Geometric energy transport and refrigeration with driven quantum dots

N.B. When citing this work, cite the original published paper.

(article starts on next page)

Geometric energy transport and refrigeration with driven quantum dots

Juliette Monsel [1,*] Jens Schulenborg [2] Thibault Baquet [1] and Janine Splettstoesser [1]

[1]*Department of Microtechnology and Nanoscience, Chalmers University of Technology, 412 96 Göteborg, Sweden*
[2]*Center for Quantum Devices, Niels Bohr Institute, University of Copenhagen, 2100 Copenhagen*

We study geometric energy transport in a slowly driven single-level quantum dot weakly coupled to electronic contacts and with strong on-site interaction, which can be either repulsive or attractive. Exploiting a recently discovered fermionic duality for the evolution operator of the master equation, we provide compact and insightful analytic expressions of energy pumping curvatures for any pair of driving parameters. This enables us to systematically identify and explain the pumping mechanisms for different driving schemes, thereby also comparing energy and charge pumping. We determine the concrete impact of many-body interactions and show how particle-hole symmetry and fermionic duality manifest, both individually and in combination, as system-parameter symmetries of the energy pumping curvatures. Building on this transport analysis, we study the driven dot acting as a heat pump or refrigerator, where we find that the sign of the on-site interaction plays a crucial role in the performance of these thermal machines.

I. INTRODUCTION

Energy transport in driven mesoscopic systems is of high interest from the perspective of two very different research fields. First, while steady-state transport spectroscopy is a well-established experimental tool to characterize quantum devices, opportunities arising from the combination of ac driving [1–17] and heat or energy transport [18–26] in spectroscopy are promising but have been less explored. Of specific interest in this context is whether these two "knobs" can be leveraged in adiabatic energy pumping [27–30], which is expected to give new insights, especially when factoring in the geometric nature of pumping due to slow driving [27,29,31–33]. Second, periodic driving to pump controlled energy flows in mesoscopic conductors is at the heart of realizing cyclic thermal machines at the nanoscale. A broad analysis of such cyclic small-scale engines has been put forward in very different types of devices; see, e.g., Refs. [34–40] and references therein. Driven quantum dots are one of the most basic setups in which a cyclic operation for, e.g., heat engines [41,42] and motors [43–50] can be implemented. Geometric charge pumping by slowly driving such dots has been analyzed in great detail in theory [3,51–60] and experiment [61–64]. However, energy pumping has only been studied addressing specific aspects [27,29,65–68], whereas a detailed,

full-fledged analytical study is still missing, even for the simplest case of a single-level quantum dot.

This paper therefore systematically analyzes geometric energy pumping through a single-level quantum dot with
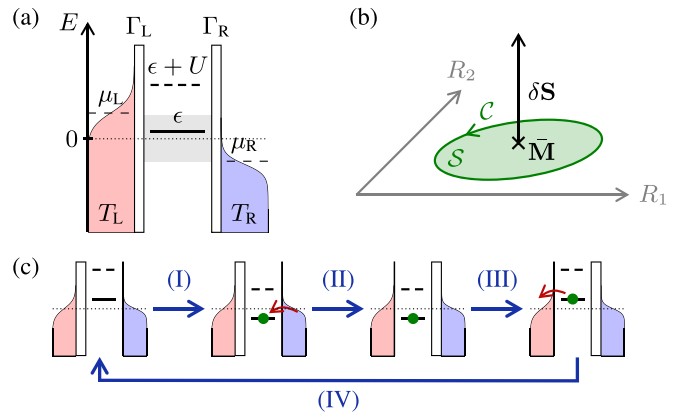

FIG. 1. (a) Energy landscape of a spin-degenerate single-level quantum dot with level position ϵ and local two-particle interaction strength U, tunnel coupled to two reservoirs $\alpha =$ L, R at temperature T_α and chemical potential μ_α, where $\mu_\text{L} - \mu_\text{R} = V_\text{b}$, with coupling strengths $\Gamma_{\text{L/R}} = \Gamma(1 \pm \Lambda)/2$, where Γ is a fixed typical tunneling frequency and Λ is the left-right asymmetry. The sketch shows the usual situation of repulsive Coulomb interaction $U > 0$, but we also consider the attractive case $U < 0$. (b) Representation of the closed driving path $\mathcal{C}$ in parameter space of a pair of generic driving parameters R_1 and R_2, encircling the surface with vector $\delta\mathbf{S}$ and area $\mathcal{S} = |\delta\mathbf{S}|$ around a working point defined by time-averaged parameters $\bar{\mathbf{M}} = (\bar\epsilon, \bar{U}, \bar{V}_\text{b}, \bar\Lambda, \bar{T}_\text{L})$. The pumping procedure is detailed in Sec. II B. (c) Example of a driving cycle as considered in Sec. V, implementing a refrigerator with $T_\text{L} > T_\text{R}$ and $\mu_\text{L} = \mu_\text{R}$ and driving parameters ϵ and Λ, the latter indicated by vertical lines of different thickness.

*monsel@chalmers.se

possibly strong on-site interaction, which can be either repulsive or attractive, and weak tunnel coupling to electronic reservoirs. We address the characteristics of energy pumping for transport spectroscopy as well as cyclically operated quantum-dot heat engines. Appealing to both the geometric character of the driving and general symmetries of open fermionic systems, we derive analytical expressions directly linking the intuitively understandable, well-known dc linear response properties of the dot [69,70] to the pumped charge and energy. This enables an in-depth pumping analysis revealing the pumped energy to be significantly more insightful into the resonant and off-resonant dot dynamics than the charge, especially for attractive interaction. Moreover, we directly relate the efficiency of the dot operated as a driven refrigerator or heat pump to the dot's steady-state thermovoltage. This makes particularly transparent how local electron pairing due to attractive on-site interaction would influence this operation.

To realize geometric charge and energy pumping, we assume the system to be slowly driven in time by the periodic modulation of an arbitrary pair of parameters (see Fig. 1). This includes any finite, and possibly driven interaction strength, bias voltage [6,31,71] and temperature differences between the leads, with the latter two being particularly relevant when operating the system as an engine, a refrigerator, or a heat pump. Namely, time-dependent driving can result in charge and energy flow against the current direction imposed by biases. Beyond thermoelectrics, geometric pumping currents which superpose bias-induced stationary currents have also been shown to be useful as a spectroscopic tool [6,31].

We also include the less usual attractive interaction in our analysis. In locally confined systems, an electron pair can experience such attractive interaction if, by bringing the pair closer together, additional electrons repelling off the pair are enabled to redistribute in a way that overcompensates the added Coulomb energy between the pair [71]. This effect was shown experimentally for quantum dots in Refs. [72–75], thus providing a simple tunable platform to test the effect of possibly strong electron pairing on various transport phenomena. In particular, the energy current through such a dot directly probes the interaction energy, in contrast to the charge current [76,77], and attractive interaction has been predicted to exhibit unusual features already in stationary thermoelectric transport [78]. It is thus not only fundamentally interesting to extend the previous work on geometric charge pumping with attractive interaction 71] to energy pumping. In fact, it is also expected and confirmed by our work that interaction-induced pairing can have a considerable effect on the operation and performance of a dot as a driven thermal machine.

To efficiently cover the many different system parameter regimes, we make use of a recently discovered dissipative symmetry of the master equation of fermionic systems [76], which is referred to as fermionic duality. This duality relation has proven useful to describe heat and energy transport not only in time-dependently driven [77,79,80] but also in stationary systems [78,81,82]. Importantly, fermionic duality is valid for arbitrary local interaction strengths, as well as for any bias voltage or temperature difference between the leads; it hence yields general yet compact and easy to interpret analytical results for the complete geometric formulation of the pumped energy. We thereby systematically identify, for both

strong repulsive or attractive on-site interactions, different pumping mechanisms [71] and pinpoint the nature of the contributions of different modes of the dissipative dot dynamics. This in particular exposes the parameter regimes in which the pumped energy differs nontrivially from the pumped charge and highlights the impact of many-body interactions. Moreover, our formalism clearly identifies symmetries between the pumped energy at different working points and with different interaction signs, due to particle-hole symmetry and due to fermionic duality itself. Equipped with these general physical insights into energy pumping, we then address the slowly driven quantum dot specifically as a refrigerator or heat pump. Our analytical approach relates the performance of this quantum-dot machine directly to the dot's steady-state Seebeck coefficient, its equilibrium charge fluctuations, and its typical *RC* time [83]. This provides intuitive yet quantitative predictions for the output power and efficiency and elucidates how the interplay between on-site interaction, its sign, and the driving frequency affects these quantities.

The paper is organized as follows. We introduce the theoretical approach in Sec. II. Section III then sets up the full analytical formulation of the pumping transport equations relying on the fermionic duality and discusses general properties of (energy) pumping based on these analytical results. Specific features of energy pumping for different driving schemes are discussed in detail in Sec. IV A for a quantum dot with repulsive on-site interaction and in Sec. IV B for a quantum dot with attractive on-site interaction. In Sec. V we analyze the driven quantum dot as a refrigerator or heat pump, where heat is pumped out of the cold and into the hot contact, and identify the performance characteristics for repulsive and attractive quantum dots. Readers more inclined towards this last part may also skip the discussion in Sec. IV, as Sec. V focuses on a different system parameter regime. Further details and derivations are presented in extensive Appendixes.

II. THEORETICAL APPROACH

We start by introducing the model for the quantum dot and the time-dependent driving leading to pumping. This also includes an overview of the master-equation approach our theoretical analysis is based on.

A. Quantum-dot model

We consider a single-level quantum dot, with a spin-degenerate energy level ϵ, tunnel coupled to an environment as represented in Fig. 1(a). The total Hamiltonian $\hat{H}_{\text{tot}} = \hat{H} + \sum_\alpha \hat{H}_\alpha + \hat{H}_{\text{tun}}$ describes the isolated quantum dot ($\hat{H}$), two macroscopic electronic contacts ($\hat{H}_{\alpha=\text{L,R}}$), and their tunnel coupling to the dots ($\hat{H}_{\text{tun}}$). The dot Hamiltonian reads

$$\hat{H} = \sum_{\sigma=\uparrow,\downarrow} \epsilon \hat{N}_\sigma + U \hat{N}_\uparrow \hat{N}_\downarrow. \tag{1}$$

Here the occupation number operator for the different spin directions is given by $\hat{N}_\sigma = \hat{d}_\sigma^\dagger \hat{d}_\sigma$, with the dot annihilation operator $\hat{d}_\sigma$ for spin σ and $\hat{N} = \sum_\sigma \hat{N}_\sigma$. We account for (possibly strong) on-site interaction between electrons, which is characterized by the interaction strength U. Importantly, in the present paper, we analyze the standard situation of repulsive

Coulomb interaction, where $U > 0$, but also the case where the on-site interaction is attractive, $U < 0$. Such quantum dots with attractive interaction have recently been studied theoretically [84–88], and have been realized in experiment [72–75]. The possible states of the dot are the empty state $|0\rangle$, the single occupied state with either spin up ($|\uparrow\rangle$) or spin down ($|\downarrow\rangle$), or the state of double occupation $|2\rangle$.

The two macroscopic electronic contacts $\alpha = $ L,R are assumed to be simple spin-degenerate metallic leads. The corresponding Hamiltonian of the lead α is given by

$$\hat{H}_\alpha = \sum_{k,\sigma} \varepsilon_{\alpha,k} \hat{c}^\dagger_{\alpha,k,\sigma} \hat{c}_{\alpha,k,\sigma}, \qquad (2)$$

with the annihilation operator $\hat{c}_{\alpha,k,\sigma}$ acting on states with orbital quantum number k. The lead occupation number operator is given by $\hat{N}_\alpha = \sum_{k,\sigma} \hat{c}^\dagger_{\alpha,k,\sigma} \hat{c}_{\alpha,k,\sigma}$. The Fermi functions $f^\pm_\alpha(E) = \{1 + \exp[\pm(E - \mu_\alpha)/k_B T_\alpha]\}^{-1}$ with the electrochemical potential μ_α and the temperature T_α quantify the corresponding average particle $(+)$/hole $(-)$ occupation per mode with energy E.

The state of the quantum dot can change in time due to tunneling to or from the leads. The corresponding tunneling Hamiltonian is assumed to be spin independent,

$$\hat{H}_{\text{tun}} = \sum_{\alpha,k,\sigma} V_{\alpha,k} \hat{c}^\dagger_{\alpha,k,\sigma} \hat{d}_\sigma + \text{H.c.} \qquad (3)$$

Given the simple metallic contacts described above, the tunneling Hamiltonian $\hat{H}_{\text{tun}}$ conserves spin and charge. On an energy scale given by the internal dot splittings, the density of states in the contacts and coupling strength $V_{\alpha,k}$ typically vary little around the chemical potential. We therefore simplify the typical tunneling rate $\Gamma_\alpha = \pi \rho_\alpha |V_\alpha|^2$ also as energy independent, i.e., with $V_{\alpha,k} \equiv V_\alpha$ (wideband limit).

The focus of our studies is on the (experimentally relevant) weak-coupling regime $\Gamma_\alpha \ll k_B T_\alpha$. Since we are particularly interested in the role of electron-electron interaction for energy pumping, we furthermore mostly study (but are not limited to) the case $|U| \gg k_B T_\alpha$, especially for the detailed analysis in Sec. IV. Also note that here we consider only devices in which the energy flow via coupling between electrons and bosonic degrees of freedom (phonons, photons, etc.) is negligible. Finally, we henceforth set $\hbar = k_B = |e| = 1$.

B. Adiabatic charge and energy pumping

This paper deals with adiabatic charge and energy pumping, i.e., charge and energy transport across the quantum dot due to the slow periodic modulation of system parameters. We hence analyze the time-resolved particle and energy currents into one contact α,

$$I_{N\alpha}(t) = \partial_t \langle \hat{N}_\alpha \rangle, \quad I_{H\alpha}(t) = \partial_t \langle \hat{H}_\alpha \rangle, \qquad (4)$$

averaged over one period $2\pi/\Omega$ of the driving, $\Delta N_\alpha = \int_0^{2\pi/\Omega} dt\, I_{N\alpha}(t)$ and $\Delta H_\alpha = \int_0^{2\pi/\Omega} dt\, I_{H\alpha}(t)$. We denote the expectation value with respect to the total-system state by $\langle \bullet \rangle$. The adiabatically pumped transport quantities[1] ΔN_α and

ΔH_α are geometric quantities [32,33,89–92] and require the modulation of at least a pair of driving parameters encircling a finite surface in parameter space, as indicated in Fig. 1(b).

A pure pumping current is obtained when modulating the dot and coupling parameters $\epsilon(t)$, $U(t)$, and $\Gamma_\alpha(t)$. This can in practice be achieved by externally driven local gate voltages. In the theoretical description, their time dependence enters directly the Hamiltonian parameters introduced in Sec. II A. With regard to the dot-contact coupling, it was previously found for our setup [71] that the variation of the combined coupling strength $\Gamma(t) = \Gamma_L(t) + \Gamma_R(t)$ does not lead to any pumping. We hence set $\Gamma(t) = \Gamma$ and consider the left-right asymmetry $\Lambda(t) = [\Gamma_L(t) - \Gamma_R(t)]/[\Gamma_L(t) + \Gamma_R(t)]$ as the only coupling-related pumping parameter.

Beyond pure pumping, we also consider a more generic situation with finite, possibly time-dependent voltage biases and temperature differences. The adiabatic pumping currents are then the first order in driving-frequency contributions in addition to the zeroth-order currents, the latter stemming from steady-state biases or rectification effects. Driven electrochemical potentials $\mu_\alpha(t)$ are routinely realized in ac transport experiments. However, the time-dependent modulation of temperatures $T_\alpha(t)$ of electronic contacts requires well-controlled heating and cooling [93,94]. The theoretical treatment of these macroscopic parameters can be performed here by replacing the parameters in the Fermi functions by time-dependent parameters. A more detailed justification of this procedure is given in Appendix A (see also Refs. [95–97]). For practical reasons, we choose to modulate the bias voltage $V_b(t) = \mu_L(t) - \mu_R(t)$ symmetrically with respect to both leads, thereby setting the average potential $\mu_0 = (\mu_L + \mu_R)/2 \equiv 0$ as reference energy. Temperature driving is instead only performed on the left reservoir $T_L(t)$; the right contact remains at a fixed temperature $T_R \equiv T$, which we typically use as energy unit.

Adiabatic pumping due to any of these driving parameters is geometric and does not depend on the detailed time dependence of the driving, but only on the area of the enclosed surface.[2] Since the precise boundary shape of this surface is not essential for our discussion, we assume an analytically convenient, sinusoidal form

$$R_i(t) = \bar{R}_i + \delta R_i \sin(\Omega t + \varphi_i), \qquad (5)$$

with frequency Ω for the periodically driven parameters $\epsilon(t)/T$, $U(t)/T$, $V_b(t)/T$, $\Lambda(t)$, and $T_L(t)/T$. The working point defined by the constant contribution $\bar{R}_i$ and the amplitude δR_i are set independently for all different modulated parameters. The phases φ_i need to differ between the different R_i to achieve a finite encircled surface in parameter space and hence a possibly finite pumped quantity. The adiabaticity condition reads [6]

$$\Omega \delta R_i \ll \Gamma. \qquad (6)$$

For better readability, we will later collect the set of any two driving parameters for a specific protocol in a three-

---

[1]This study can straightforwardly be extended to heat currents $I_{Q\alpha}(t) = I_{H\alpha}(t) - \mu_\alpha(t) I_{N\alpha}(t)$ (see also Appendix A).

[2]At higher orders in frequency, a single driven dot parameter is sufficient since the required asymmetry is provided by the slight lagging behind of the particle current compared to the driving [98].

component vector $\mathbf{R} = (R_1(t), R_2(t), 0)^{\mathsf{T}}$. We call any pair of two parameters a driving scheme.

C. Master equation and fermionic duality

To describe the dynamics of the driven quantum-dot system and to calculate the sought transported charge and energy, we resort to a master-equation approach [3,6,98]. This is valid in the regime of weak coupling relevant here $\Gamma \ll \min_\alpha\{T_\alpha\}$ and for up to moderately slow driving $0 < \Omega\delta R_i/\Gamma \lesssim 1$. Performing an expansion in Ω/Γ, the time evolution of the reduced quantum-dot density matrix $\rho(t)$ reads

$$0 = W|\rho^{(0)}(t)), \quad \partial_t|\rho^{(\ell-1)}(t)) = W|\rho^{(\ell)}(t)). \quad (7)$$

This introduces the instantaneously time-dependent kernel superoperator W, which describes transitions due to tunneling events between dot and reservoirs. The kernel acts on the reduced density operator $|\rho(t)) = \hat{\rho}(t)$. We choose a notation with rounded kets $|x)$ for operators $\hat{x}$ in Liouville space and with rounded bras for the corresponding covectors $(x|\bullet = \mathrm{Tr}\{\hat{x}^\dagger\bullet\}$ with respect to the Hilbert-Schmidt scalar product. The driving-frequency expansion is denoted by the superscript (ℓ), representing the ℓth order in Ω/Γ. The solution for the density operator $|\rho(t)) = \sum_{\ell=0}^\infty |\rho^{(\ell)}(t))$ then follows from the master equation (7), including the instantaneous stationary state $|\rho^{(0)}(t)) \equiv |z)$ with respect to the modulated system parameters at some time t, as well as the corrections $|\rho^{(\ell)}(t))$ in ℓth order in Ω/Γ.

Note that due to charge- and spin-conserving tunneling, the occupation probabilities $P_i(t) = \langle i|\rho(t)|i\rangle$, namely, the diagonal elements of the reduced density matrix in the basis of dot energy eigenstates, decouple from the coherences, namely, the off-diagonal elements $\langle i|\rho(t)|j\rangle$. Since the pumped charge and energy (as the observables relevant here) are also diagonal in the energy eigenbasis, the coherent dynamics is completely discarded and we determine only the time-dependent probabilities to obtain the relevant transport quantities. The required matrix representation of the kernel W in the remaining probability subspace consists of transition rates between the dot energy eigenstates of zero $[|0) = |0\rangle\langle 0|]$, single[3] $[|1) = \frac{1}{2}\sum_{i=\uparrow,\downarrow}|i\rangle\langle i|]$, and double $[|2) = |2\rangle\langle 2|]$ occupation. The rates can be calculated using the lead decomposition $W = \sum_\alpha W^\alpha$ and Fermi's golden rule for each lead-resolved kernel W^α separately. They are given by[4]

$$W_{10}^\alpha = 2\Gamma_\alpha f_\alpha^+(\epsilon), \quad W_{21}^\alpha = \Gamma_\alpha f_\alpha^+(\epsilon + U),$$
$$W_{01}^\alpha = \Gamma_\alpha f_\alpha^-(\epsilon), \quad W_{12}^\alpha = 2\Gamma_\alpha f_\alpha^-(\epsilon + U). \quad (8)$$

The diagonal elements of the matrices representing W^α and hence W are obtained from these rates by total probability conservation, dictating $(\mathbb{1}|W^\alpha = (\mathbb{1}|W = 0$ with identity operator $\hat{\mathbb{1}}$. The instantaneous time dependence of W comes

---

[3]The spin degree of freedom does not play any role in this work and we therefore do not separately treat the different spin state occupations in the singly occupied mixed state.

[4]The basis is trace normed, but not orthonormal, since $(1|1) = 1/2$. Therefore, $W = \sum_{ij} \frac{(i|W|j)}{(i|i)(j|j)}|i)(j|$ (see the Supplemental Material of [76]).

from the driving parameters [Eq. (5)] entering the expressions of the tunneling rates and Fermi functions in Eq. (8).

While the solution for the occupation probabilities as well as for the transport quantities can in principle be straightforwardly carried out, such a straightforward approach typically yields rather long, inaccessible expressions that offer little clues towards further parameter-regime specific simplifications and approximations. An improved understanding based on more compact and insightful analytical results, can however be obtained from a recently discovered fermionic duality relation. This has proven to be particularly useful in understanding dot systems driven out of equilibrium [76,77,79,80] and observables influenced by strong many-body effects, such as the energy being affected by a large Coulomb interaction $|U|/T \gg 1$ [78,81].

Specifically, this dissipative symmetry for the kernel W of the master equation, i.e., the fermionic duality, connects the Hermitian conjugate of W to the kernel of a dual model, in which all energies are inverted (see Appendix B). This allows us to straightforwardly write the kernel in its eigenbasis [79,81]

$$W = -\gamma_{\mathrm{p}}|p)(p'| - \gamma_{\mathrm{c}}|c)(c'|, \quad (9)$$

which can be interpreted in a meaningful way. The eigenvalues of the kernel are the negative of the relaxation rates, which one identifies as the charge relaxation rate γ_{c}, the parity rate γ_{p}, and the additional eigenvalue 0, which corresponds to the stationary state. The fermionic duality cross relates the relaxation rates to each other. In particular, the parity rate $\gamma_{\mathrm{p}} = 2\Gamma$ connects to the zero eigenvalue of the kernel through the duality-based decay rate relation between any two eigenmodes x and y,

$$\gamma_y = 2\Gamma - \gamma_x^{\mathrm{i}}. \quad (10)$$

The superscript i indicates the dual model with inverted energies

$$\epsilon^{\mathrm{i}} = -\epsilon, \quad U^{\mathrm{i}} = -U, \quad \mu_\alpha^{\mathrm{i}} = -\mu_\alpha. \quad (11)$$

The temperature and coupling rate Γ are not inverted by the dual transform. The charge relaxation rate $\gamma_{\mathrm{c}} = f_\epsilon^+ + f_U^-$, where we use the compact notation for combinations of Fermi functions $f_\epsilon^\pm = \sum_\alpha \Gamma_\alpha f_\alpha^\pm(\epsilon)$ and $f_U^\pm = \sum_\alpha \Gamma_\alpha f_\alpha^\pm(\epsilon + U)$, is self-dual following the relation of Eq. (10).

In a similar way, the right and left eigenvectors of the kernel are interconnected through the duality-based cross relation

$$(y'| = [(-\hat{\mathbb{1}})^{\hat{N}}|x^{\mathrm{i}})]^\dagger = [e^{i\pi\hat{N}}|x^{\mathrm{i}})]^\dagger. \quad (12)$$

This relation leads to the compact form of charge and parity decay as well as the stationary state $|z)$, given by

$$|z) = \frac{1}{\Gamma\gamma_{\mathrm{c}}}[f_\epsilon^- f_U^-|0) + f_\epsilon^+ f_U^-|1) + f_\epsilon^+ f_U^+|2)],$$

$$|p) = |(-\mathbb{1})^N), \quad |c) = \frac{1}{2}(-\hat{\mathbb{1}})^{\hat{N}}[|N) - N_z^{\mathrm{i}}|\mathbb{1})], \quad (13)$$

and the corresponding left eigenvectors

$$(z'| = (\mathbb{1}|, \quad (p'| = (z^{\mathrm{i}}(-\mathbb{1})^N|,$$
$$(c'| = (N| - N_z(\mathbb{1}|. \quad (14)$$

Equations (13) and (14) contain the dot occupations

$$N_z = (N|z), \quad N_z^i = (N|z^i) \quad (15)$$

with respect to the stationary state $|z)$ and with respect to the dual stationary state $|z^i)$, that is, the stationary state in the dual model with inverted energies (see Appendix B for explicit analytical expressions).

Our following analysis of energy pumping benefits from this approach using the duality-based eigendecomposition of the kernel W in Eqs. (9)–(15). The basic starting point is to write both the zeroth-order solution $|\rho^{(0)})$ and the first-order correction in frequency $|\rho^{(1)})$ in terms of the instantaneous eigenmodes and the corresponding decay rates

$$|\rho^{(0)}) = |z), \quad |\rho^{(1)}) = \frac{1}{\tilde{W}} \partial_t |z), \quad (16)$$

with the pseudoinverse of the kernel

$$\frac{1}{\tilde{W}} = -\frac{1}{\gamma_p} |p)(p'| - \frac{1}{\gamma_c} |c)(c'|. \quad (17)$$

This pseudoinverse was constructed by exploiting that it only ever acts on vectors $|x)$ orthogonal to the zero-eigenvalue subspace, i.e., with $(\mathbb{1}|x) = 0$. Finally, for energy pumping in a refrigerator scheme as discussed in Sec. V, we also require second-order corrections in frequency,

$$|\rho^{(2)}) = \frac{1}{\tilde{W}} \partial_t \left[\frac{1}{\tilde{W}} \partial_t |z) \right]. \quad (18)$$

This correction constitutes a limitation for thermodynamically efficient pumping [41].

III. TRANSPORT EQUATIONS

A. Transport of a generic observable due to time-dependent driving

Based on the theoretical approach introduced in Sec. II, we now calculate the stationary current as well as the first order in Ω/Γ correction leading to pumping, for an arbitrary observable. One can write the ℓth-order contribution to the current into contact α as

$$I_{\mathcal{O}\alpha}^{(\ell)} = (\mathcal{O}|W^\alpha|\rho^{(\ell)}), \quad (19)$$

that is, in terms of a local dot observable $\hat{\mathcal{O}}$, as long as this observable is conserved [99]. This means that the flow of the expectation value of the observable $\hat{\mathcal{O}}$ out of the local dot system equals the sum over the currents into all contacts. It is naturally fulfilled for the dot charge as the local observable and the resulting charge currents into the contacts. For the energy current, Eq. (19) is only valid if no energy is stored on the tunneling barriers, that is, when $\langle \hat{H}_{\text{tun}} \rangle(t)$ is constant. The latter is true for the weakly coupled dot considered here [100] as long as nonelectronic energy flow due to, e.g., dissipation to phonons is negligible. By contrast, in strong-coupling situations, the time-dependent storage of energy on the barriers can play an important role [46,101,102].

The ingredients of Eq. (19) are known for stationary charge and energy currents ($\ell = 0$) and have been analyzed by exploiting the fermionic duality in detail [81]. Also, time-dependent charge and energy currents through a quantum dot

have been analyzed after a rapid switch in the parameters [76,77,79]. By contrast, a detailed analysis of the pumping currents exploiting the fermionic duality has been missing.

Collecting the time-dependent parameters in the driving scheme $\mathbf{R} = (R_1(t), R_2(t), 0)^\mathsf{T}$ as prescribed at the end of Sec. II B, we can write the pumping current as [31]

$$I_{\mathcal{O}\alpha}^{(1)} = (\mathcal{O}|W^\alpha \frac{1}{\tilde{W}} \boldsymbol{\nabla}_\mathbf{R} |z) \cdot \partial_t \mathbf{R}, \quad (20)$$

with the gradient defined as $\boldsymbol{\nabla}_\mathbf{R} = (\partial_{R_1}, \partial_{R_2}, 0)^\mathsf{T}$. The resulting transported observable per driving period equals a geometric phase, as pointed out by Ning and Haken [103] and Landsberg [104] (see also Refs. [32,33,105]),

$$\Delta\mathcal{O}_\alpha^{(1)} = \int_0^{2\pi/\Omega} dt \, I_{\mathcal{O}\alpha}^{(1)}(t) = \oint_\mathcal{C} d\mathbf{R} \cdot \mathbf{A}_{\mathcal{O}\alpha}(\mathbf{R}) \quad (21a)$$

$$= \iint_\mathcal{S} d\mathbf{S} \cdot \mathbf{B}_{\mathcal{O}\alpha}(\mathbf{R}), \quad (21b)$$

with the geometric connection

$$\mathbf{A}_{\mathcal{O}\alpha}(\mathbf{R}) = (\mathcal{O}|W^\alpha \frac{1}{\tilde{W}} \boldsymbol{\nabla}_\mathbf{R} |z) \quad (22)$$

and the pseudomagnetic field, also called the pumping curvature,[5]

$$\mathbf{B}_{\mathcal{O}\alpha}(\mathbf{R}) = \boldsymbol{\nabla}_\mathbf{R} \times \mathbf{A}_{\mathcal{O}\alpha}(\mathbf{R}). \quad (23)$$

The pumping curvatures $\mathbf{B}_{H\alpha}(\mathbf{R})$ and $\mathbf{B}_{N\alpha}(\mathbf{R})$ for the energy ($\hat{\mathcal{O}} = \hat{H}$) and charge ($\hat{\mathcal{O}} = \hat{N}$) will be analyzed in detail in Sec. IV for different sets of pumping parameters, using the insights from the fermionic duality relation. However, before addressing any specific transport observable, we note that the time-dependent driving of parameters can excite the quantum system away from the stationary state in two different ways, namely,

$$\frac{1}{\tilde{W}} \boldsymbol{\nabla}_\mathbf{R} |z) = \mathbf{x}^\mathrm{C} |c) + \mathbf{x}^\mathrm{P} |p), \quad (24)$$

with a charge-type excitation and a parity-type excitation. Exploiting the duality-based kernel decomposition, the amplitudes of these excitations can be written as

$$\mathbf{x}^\mathrm{C} = -\frac{1}{\gamma_c}(N|\boldsymbol{\nabla}_\mathbf{R} |z) = -\frac{1}{\gamma_c} \boldsymbol{\nabla}_\mathbf{R} N_z, \quad (25a)$$

$$\mathbf{x}^\mathrm{P} = -\frac{1}{\gamma_p}(z^i(-\mathbb{1})^N|\boldsymbol{\nabla}_\mathbf{R} |z) \quad (25b)$$

$$= -\frac{1}{4\gamma_p} \boldsymbol{\nabla}_\mathbf{R} p_z - \frac{1}{2\gamma_p}(N_z^i - 1)\boldsymbol{\nabla}_\mathbf{R} N_z, \quad (25c)$$

---

[5]By using more general differential forms than $\boldsymbol{\nabla}_\mathbf{R} \times \bullet$, one can generalize Stokes's theorem (see, for example, Ref. [106]) to connect Eq. (21a) with Eq. (23) for any discrete dimensional vector $\mathbf{R}$, corresponding to driving arbitrarily many parameters simultaneously. Our treatment, however, focuses on the minimal and experimentally relevant situation of two-parameter driving, for which the driving cycle describes a path $\mathcal{C}$ enclosing the surface $\mathcal{S}$ of a flat two-dimensional plane in parameter space as shown in Fig. 1(b).

with the stationary quantum-dot parity $p_z = ((-\mathbb{1})^N |z)$ (see Appendix B for explicit analytical expressions). The function $\mathbf{x}^C$ for the chargelike excitation is expectedly proportional to the inverse of the charge relaxation rate γ_c and the paritylike term $\mathbf{x}^P$ is proportional to the inverse of the parity rate γ_p. However, when expressing $\mathbf{x}^P$ in terms of observables as in (25c), we find gradients of both the stationary parity p_z and occupation number N_z, with the latter also entering via the dual occupation N_z^i. This observable decomposition in (25c), as well as the vector-overlap form in Eq. (25b), will offer valuable insights for the interpretation of energy pumping in the remainder of this paper.

Further exploiting the mode decomposition (24), we can split the geometric connection of a specific observable $\hat{\mathcal{O}}$, transported into a specific contact α, $\mathbf{A}_{\mathcal{O}\alpha}(\mathbf{R})$, into contributions $\mathbf{A}_{\mathcal{O}\alpha}(\mathbf{R}) = \mathbf{A}_{\mathcal{O}\alpha}^C(\mathbf{R}) + \mathbf{A}_{\mathcal{O}\alpha}^P(\mathbf{R})$ coming, respectively, from the chargelike and paritylike system excitations due to the driving,

$$\mathbf{A}_{\mathcal{O}\alpha}^{C/P}(\mathbf{R}) = (\mathcal{O}|W^\alpha|c/p)\mathbf{x}^{C/P}. \tag{26}$$

The crucial point is now that the eigenmode decomposition given in Eqs. (9)–(15) for the full kernel W only derives from probability conservation, from the local equilibrium state in each individual lead α, and from fermionic duality [79,81]. The decomposition can hence be carried out in exactly the same way for the lead-resolved kernel W^α. This yields a lead-resolved stationary state $|z_\alpha)$, dual state $|z_\alpha^i)$, and their associated lead-resolved dot occupation numbers

$$N_{z\alpha} = (N|z_\alpha), \quad N_{z\alpha}^i = (N|z_\alpha^i). \tag{27}$$

These quantities together determine the full set of lead-resolved eigenvectors of W^α as well as the corresponding charge rate $\gamma_{c\alpha} = \Gamma_\alpha[f_\alpha^+(\epsilon) + f_\alpha^-(\epsilon + U)]$ and parity rate $\gamma_{p\alpha} = 2\Gamma_\alpha$. In particular, we again obtain the parity mode $|p_\alpha) = |p) = |(-\mathbb{1})^N)$ as a parameter-independent right eigenvector. When inserted together with Eq. (25) into Eq. (26), this eigenvector yields

$$\mathbf{A}_{\mathcal{O}\alpha}^C(\mathbf{R}) = a_{\mathcal{O}\alpha}^C \nabla_\mathbf{R} N_z, \tag{28a}$$

$$\mathbf{A}_{\mathcal{O}\alpha}^P(\mathbf{R}) = a_{\mathcal{O}\alpha}^{P,p} \nabla_\mathbf{R} p_z + a_{\mathcal{O}\alpha}^{P,N} \nabla_\mathbf{R} N_z, \tag{28b}$$

where

$$a_{\mathcal{O}\alpha}^C = \frac{\gamma_{c\alpha}}{\gamma_c}(\mathcal{O}|c_\alpha) + \frac{\gamma_{p\alpha}}{\gamma_c}(p_\alpha'|c)(\mathcal{O}|p), \tag{29a}$$

$$a_{\mathcal{O}\alpha}^{P,p} = \frac{\gamma_{p\alpha}}{4\gamma_p}(\mathcal{O}|p), \quad a_{\mathcal{O}\alpha}^{P,N} = \frac{\gamma_{p\alpha}}{2\gamma_p}(N_z^i - 1)(\mathcal{O}|p). \tag{29b}$$

This set of equations readily shows the requirements that a certain observable must fulfill in order to make the different excited modes (chargelike and paritylike) visible. The second term in Eq. (29a) and the two paritylike terms from Eq. (29b) in particular only contribute if the observable $\hat{\mathcal{O}}$ is sensitive to many-body effects. Geometric charge pumping ($\hat{\mathcal{O}} = \hat{N}$) in the quantum-dot system studied here is therefore not sensitive to the parity mode excitation, as $(N|p) = (N|(-\mathbb{1})^N) = 0$ leaves only the first term in Eq. (29a) to contribute. The consequence is that the charge pumping current is directly proportional to the inverse of the charge relaxation rate [6,107]. Moreover, since a finite bias voltage or temperature difference generally causes the lead-resolved eigenvectors of

W^α to differ from those of the full kernel, $(p_\alpha'| \neq (p'|$ and $|c_\alpha) \neq |c)$, the ratio between chargelike and paritylike contributions generally also depends on the contact in which the transported observable is detected.

To obtain compact and insightful expressions for the pumped transport variables (such as the pumped charge and energy), we split the pumping curvature in a similar way, $\mathbf{B}_{\mathcal{O}\alpha}(\mathbf{R}) = \mathbf{B}_{\mathcal{O}\alpha}^C(\mathbf{R}) + \mathbf{B}_{\mathcal{O}\alpha}^P(\mathbf{R})$, with $\mathbf{B}_{\mathcal{O}\alpha}^{C/P}(\mathbf{R}) = \nabla_\mathbf{R} \times \mathbf{A}_{\mathcal{O}\alpha}^{C/P}(\mathbf{R})$. The pumping curvature then generally reads

$$\mathbf{B}_{\mathcal{O}\alpha}^C(\mathbf{R}) = \nabla_\mathbf{R} a_{\mathcal{O}\alpha}^C \times \nabla_\mathbf{R} N_z,$$

$$\mathbf{B}_{\mathcal{O}\alpha}^P(\mathbf{R}) = \nabla_\mathbf{R} a_{\mathcal{O}\alpha}^{P,p} \times \nabla_\mathbf{R} p_z + \nabla_\mathbf{R} a_{\mathcal{O}\alpha}^{P,N} \times \nabla_\mathbf{R} N_z. \tag{30}$$

Equation (30) clarifies that a finite pumping current needs not only a finite parameter gradient of the stationary dot occupation and/or parity but in particular a gradient component orthogonal to $\nabla_\mathbf{R} a_{\mathcal{O}\alpha}$ [31,71].

The analysis of charge and energy pumping put forward in this paper mainly relies on the functional form of Eqs. (28)–(30) in order to understand the different pumping mechanisms and pumping schemes.

B. Energy pumping

To support our detailed pumping analysis for various parameter drivings and external conditions in Sec. IV, we employ the fermionic-duality-based approach to highlight general analytical features relevant for energy pumping.

1. Geometric connection

We begin with analytical results for the geometric connection of energy pumping and their general physical implications, in particular in comparison to charge pumping. Equations (28) and (29) yield

$$a_{H\alpha}^C = a_{H\alpha}^{C,TC} + a_{H\alpha}^{C,NTC}, \tag{31a}$$

$$a_{H\alpha}^{P,p} = \frac{U\Gamma_\alpha}{4\Gamma}, \tag{31b}$$

$$a_{H\alpha}^{P,N} = \frac{U\Gamma_\alpha}{2\Gamma}(N_z^i - 1), \tag{31c}$$

where we have defined

$$a_{H\alpha}^{C,TC} = \mathcal{E}^\alpha \frac{\gamma_{c\alpha}}{\gamma_c}, \tag{32a}$$

$$a_{H\alpha}^{C,NTC} = \frac{U}{2} \frac{\gamma_{p\alpha}}{\gamma_c}(N_{z\alpha}^i - N_z^i). \tag{32b}$$

The term $a_{H\alpha}^{C,TC}$ includes the characteristic energy

$$\mathcal{E}^\alpha = \epsilon + \frac{U}{2}(2 - N_{z\alpha}^i) \tag{33}$$

as a function of the lead-resolved dual occupation number $N_{z\alpha}^i$ introduced above.

To interpret Eq. (31), we first note that charge pumping only senses the chargelike excitation ($\mathbf{A}_{N\alpha} \sim \mathbf{x}^C$):

$$\mathbf{A}_{N\alpha}(\mathbf{R}) = a_{N\alpha}^C \nabla_\mathbf{R} N_z, \quad a_{N\alpha}^C = \frac{\gamma_{c\alpha}}{\gamma_c}. \tag{34}$$

Based on the expression of $a_{N\alpha}^{C}$, we identify $a_{H\alpha}^{C,TC}$ as the tight-coupling contribution to energy pumping. This term is "tightly coupled" to the charge current through multiplication by the characteristic energy $\mathcal{E}^{\alpha}$, which in fact equals the (stationary) Seebeck coefficient of the quantum dot [81]. The other term in the chargelike contribution, $a_{H\alpha}^{C,NTC}$, contributes only if $N_{z\alpha}^{i} \neq N_{z}^{i}$, i.e., when a stationary temperature difference or bias voltage is applied across the dot. This and all other contributions to energy pumping given in Eqs. (31) are uniquely due to the on-site interaction U and hence vanish in a noninteracting quantum dot.

To gain additional insight into the properties of the parity contribution $\mathbf{A}_{H\alpha}^{P}(\mathbf{R})$ to the geometric connection, let us return to its original definition in Eq. (26):

$$\mathbf{A}_{H\alpha}^{P}(\mathbf{R}) = (H|W^{\alpha}|p)\mathbf{x}^{P} = -U\gamma_{p\alpha}\mathbf{x}^{P}$$
$$= \frac{U\gamma_{p\alpha}}{\gamma_{p}}(z^{i}(-\mathbb{1})^{N}|\nabla_{\mathbf{R}}|z). \quad (35)$$

We first note that this contribution fulfills a symmetry under the dual transform, namely, under the sign inversion of all energies. Concretely, using the product rule of $\nabla_{\mathbf{R}}$ together with the eigenvector orthogonality $(z^{i}(-\mathbb{1})^{N}|z) = (z(-\mathbb{1})^{N}|z^{i}) = 0$, Hermiticity of the states $z = z^{\dagger}$ and $z^{i} = (z^{i})^{\dagger}$, and parity superselection dictating $[z, (-\mathbb{1})^{N}] = [z^{i}, (-\mathbb{1})^{N}] = 0$, we find $\mathbf{x}^{P}$ to be antisymmetric with respect to the transformation to the dual model:[6]

$$\mathbf{x}^{P,i} = -\frac{1}{\gamma_{p}}(z(-\mathbb{1})^{N}|\nabla_{\mathbf{R}}|z^{i})$$
$$= +\frac{1}{\gamma_{p}}(z^{i}(-\mathbb{1})^{N}|\nabla_{\mathbf{R}}|z) = -\mathbf{x}^{P}. \quad (36)$$

This and the sign inversion of U under the dual transform means that $\mathbf{A}_{H\alpha}^{P}(\mathbf{R}) = -U\gamma_{p\alpha}\mathbf{x}^{P}$ is self-dual, i.e., identical when transforming to the dual model. In Sec. IV B, we further translate this to a symmetry of the paritylike energy pumping curvature $\mathbf{B}_{\mathcal{O}\alpha}^{P}(\mathbf{R})$ for repulsive vs attractive on-site interaction of equal strength.

Second, we can derive from the general form of Eq. (35) and the behavior of $|z)$ and $|z^{i})$ that $\mathbf{A}_{H\alpha}^{P}(\mathbf{R})$ is nonzero only for specific parameter regions, meaning that the geometric connection for energy pumping is in many cases dominated by the charge-mode contribution $\mathbf{A}_{H\alpha}^{C}(\mathbf{R})$. Let us consider a parameter regime where both dot transition energies ϵ and $\epsilon + U$ lie outside the bias window, $|\epsilon|, |\epsilon + U| > |V_{b}|/2$. The dot state is then in either the empty or the doubly occupied state, but never in the single occupied state. The dual state $|z^{i})$ describes, by its inverted nature, a nearly opposite occupation compared to $|z)$, i.e., an empty dual state $N_{z}^{i} = 0$ for a fully occupied stationary dot state $N_{z} = 2$ and vice versa. A similar situation occurs for strong interaction: $|U| > |V_{b}|$ and $|U| \gg T_{\alpha}$. Assuming a repulsive on-site interaction $U > 0$ on the dot, the fictitious dual model with inverted energies [characterizing $|z^{i})$] has a stationary state that is characterized by an attractive interaction, $U^{i} = -U$, and is hence dominated

by electron pairing [79,81]. Therefore, the dual model exhibits a single, sharp two-particle transition at $\epsilon + U/2 = 0$. This means that the dual steady-state probability for single occupation is strongly suppressed.[7] For both of these situations, the overlap in Eq. (35) can then, independently of the sign of the interaction U, be well approximated by

$$\mathbf{A}_{H\alpha}^{P}(\mathbf{R}) \rightarrow \frac{U\gamma_{p\alpha}}{\gamma_{p}}\big[P_{0}^{i}\nabla_{\mathbf{R}}P_{0} + P_{2}^{i}\nabla_{\mathbf{R}}P_{2}\big], \quad (37)$$

where $P_{0} = (0|z)$ and $P_{2} = (2|z)$ are the probabilities for the dot to be empty (0) or doubly occupied (2) in the stationary state $|z)$ and $P_{0}^{i} = (0|z^{i})$ and $P_{2}^{i} = (2|z^{i})$ are the corresponding duals in the state $|z^{i})$. The crucial point is now that for $|V_{b}| < |U|$ and $|U| \gg T_{\alpha}$, or if both ϵ and $\epsilon + U$ are outside the bias window, P_{0}^{i} and P_{2}^{i} are only sizable for parameters in which P_{0} and P_{2} are stably suppressed, meaning $P_{0}^{i}\nabla_{\mathbf{R}}P_{0}, P_{2}^{i}\nabla_{\mathbf{R}}P_{2} \rightarrow 0$. Equation (37) thereby implies that the parity contribution $\mathbf{A}_{H\alpha}^{P}(\mathbf{R})$ to pumping of energy and in fact the parity contribution $\mathbf{A}_{\mathcal{O}\alpha}^{P}(\mathbf{R})$ to pumping of any observable become negligible in all the above-mentioned parameter regimes.

The key physical insight derived from Eq. (37) is that unless both dot resonances ϵ and $\epsilon + U$ are close to or within a bias window $|V_{b}| > |U|$, the time-dependent energy current due to the slow driving, as represented by the geometric connection $\mathbf{A}_{H\alpha}(\mathbf{R})$, is well approximated by its charge-mode contribution,

$$\mathbf{A}_{H\alpha}(\mathbf{R}) \approx a_{H\alpha}^{C}\nabla_{\mathbf{R}}N_{z} = \mathbf{A}_{H\alpha}^{C}(\mathbf{R}). \quad (38)$$

In other words, the corrections at the first order in Ω/Γ to the time-dependent energy and charge current become proportional, $I_{H\alpha}^{(1)}(t) \approx C(t)I_{N\alpha}^{(1)}(t)$. The factor $C(t) = a_{H\alpha}^{C}$ only depends on the momentary system parameter configuration, but not on the time derivative of that configuration as determined externally via the driving frequency Ω. The energy pumping curvature in this regime is accordingly governed by the charge component $\mathbf{B}_{H\alpha}(\mathbf{R}) \rightarrow \mathbf{B}_{H\alpha}^{C}(\mathbf{R})$. Since $a_{H\alpha}^{C}$ consists only of the Seebeck coefficient $\mathcal{E}^{\alpha}$ and terms proportional to dual occupation numbers N_{z}^{i} and $N_{z\alpha}^{i}$, our detailed energy pumping analysis in Sec. IV can, in many parts, simply refer to the intuitive and well-known physics governing these quantities.

Let us point out that it is rather surprising at first glance that the energy pumped through a system with comparably large interaction strength $|U|$ is due to the charge-mode excitation only, in extended parameter regions. Indeed, in contrast to the charge current, the energy current is directly sensitive to many-body effects via the Coulomb energy that can be transferred through the quantum dot even in the absence of net charge current. The suppression of paritylike terms can nevertheless be understood when distinguishing close-to-steady-state from excited-state dot dynamics. As clarified in Ref. [79], a maximally excited (or unstable) quantum-dot

---

[6]This assumes an energy inversion prior to taking the gradient $\nabla_{\mathbf{R}}$, the latter not commuting with energy inversion.

[7]An equivalent statement can be made for a quantum-dot model with attractive interaction $U < 0$. In this case, it is the stationary state of the actual dot model $|z)$ that is always given by either the empty or the doubly occupied state while the probability of single occupation is strongly suppressed.

state with respect to the environment is in fact closely approximated by the dual inverted state $|z^i\rangle$ if $|U| \gg |V_b|$, T_α or if $|\epsilon|, |\epsilon + U| \gg |V_b|/2, T_\alpha$. For example, a doubly occupied dot would be maximally unstable if the stationary dot state is close to an empty state. The overlap (35) thus expresses that (as long as the notion of a maximally unstable state is meaningful) the parity mode only enters for excitations close to maximal instability. Such maximally unstable states can be created, e.g., with fast level switches as studied in Refs. [76,77,79]. The key difference of adiabatic pumping with respect to the fast-switching case is that slow driving alone cannot induce such a strong excitation away from the steady state. The suppressed paritylike contribution to geometric energy pumping simply reflects this fact.

The analysis changes however for sufficiently large bias voltage $|V_b| > |U|$ if ϵ and $\epsilon + U$ lie either inside or at an edge of the bias window. In this case, the overlap between stationary and inverted stationary states is in general finite. However, a pumped energy current deviating from a pure charge-mode contribution for $|U| \gg T$ requires not only large biases $|V_b| \gtrsim |U|$, but also at least ϵ or $\epsilon + U$ to be close to a resonance with one lead potential μ_L or μ_R, since otherwise the gradient $\nabla_R|z\rangle$ vanishes.[8] If this resonance condition is fulfilled, any driving affecting it can then in principle also excite paritylike terms, as further illustrated in Sec. IV A. In this case, the proportionality $I_{H\alpha}^{(1)}(t) \approx C(t)I_{N\alpha}^{(1)}(t)$ between the first-order corrections of charge and energy current pointed out above breaks down. This physically means either that $I_{H\alpha}^{(1)}(t)$ can be finite while $I_{N\alpha}^{(1)}(t) = 0$ or that $C(t)$ would no longer be determined by the system properties alone, but also by the driving speed set by the frequency Ω and amplitudes δR_i in Eq. (5).

2. Pumping mechanisms

To facilitate the detailed discussion of the features of energy pumping in Sec. IV, it is helpful to label interesting areas of the parameter space. We call a pumping mechanism [71] a quantum-dot configuration[9] $\bar{M} = (\bar\epsilon, \bar{U}, \bar{V}_b, \bar\Lambda, \bar{T}_L)$ to which a driving scheme is applied such that it leads to charge or energy transport. In the following, we focus only on the impact of the three first parameters $\bar\epsilon, \bar{U}$, and $\bar{V}_b$, while $\bar\Lambda = 0$ and $\bar{T}_L = T$. We classify the different mechanisms leading to energy pumping for both a repulsive interaction ($\bar{U} > 0$) and an attractive one ($\bar{U} < 0$). We sketch the electrochemical potential configurations corresponding to these mechanisms and we indicate their locations in the ($\bar\epsilon, \bar{V}_b$) space in Fig. 2. Extending the notation used in Ref. [71] for charge pumping, we have named the mechanisms $X_s^\pm$. Here X is a letter

---

between A and H whose meaning is given in Table I. The superscript $\pm$ corresponds to the sign of the bias voltage $\bar{V}_b$. Finally, the subscript s takes the value $s = 1$ if the transition energy ϵ is resonant with the Fermi level of one of the reservoirs and $s = 2$ if the transition energy $\epsilon + U$ is resonant. The subscripts $s = 3$ and $s = 4$ indicate that a single transition energy ϵ for $s = 3$ and $\epsilon + U$ for $s = 4$ lies within the bias window.

As will be discussed in more detail in Sec. IV, mechanisms A, D, E, and G are specific to the repulsive case while C is present only in the attractive one. Mechanisms B, F, and H are common to both cases. Note that B and F are the two mechanisms involving paritylike pumping contributions.

3. Symmetry of pumping curvatures

The pumping curvatures plotted in Figs. 3 and 4 and discussed in full detail in Sec. IV exhibit several interesting symmetries under particular changes of the working-point parameters $\bar\epsilon, \bar{V}_b$, and $\bar{U}$. This section provides the key analytical results underlying these symmetries, based on a rigorous derivation in Appendix C 1.

Depending on the driving scheme, the pumping curvature in Figs. 3 and 4 is either symmetric or antisymmetric under the parameter transform $\mathcal{T} : (\epsilon, U, V_b, T_\alpha, \Lambda) \mapsto (-\epsilon - U, +U, -V_b, +T_\alpha, +\Lambda)$. This parameter transform can be shown to correspond to a particle-hole transform. Since the quantum-dot system we consider here is particle-hole symmetric, also the pumped observables ΔN_α and ΔH_α, which are obtained from a surface integral over the respective curvature, are symmetric under a particle-hole transform.

We start by addressing driving schemes with time-independent interaction U and driving of any two of the parameters $(\epsilon, V_b, T_\alpha, \Lambda)$. The transform $\mathcal{T}$ leaves the area enclosed by the cycle invariant, but may affect the cycle orientation. This goes along with sign changes of the curvature that are found to be (Appendix C 1)

$$\mathcal{T}\mathbf{B}_{H\alpha}(\mathbf{R}) = \sigma(R_1)\sigma(R_2)\mathbf{B}_{H\alpha}(\mathbf{R}), \qquad (39)$$

with the introduced signs

$$\sigma(R_i) = \begin{cases} -1 & \text{if } R_i \in \{\epsilon, V_b\} \\ +1 & \text{if } R_i \in \{T_L, \Lambda\}. \end{cases} \qquad (40)$$

By contrast, when driving $U(t)$, the particle-hole-transformed driving cycle always involves an effectively time-dependent ϵ, $\mathcal{T}\epsilon = -\epsilon - U(t)$, regardless of which second driving parameter R_2 is chosen next to U. In this case, $\mathcal{T}$ bends the driving surface out of the (U, R_2) plane at fixed ϵ, generally affecting both cycle orientation and enclosed area. Remarkably, though, we show explicitly in Appendix C 1 that the additional ϵ driving can still be straightforwardly accounted for by modifying Eq. (39) to[10]

$$\mathcal{T}\mathbf{B}_{H\alpha}(\{U, R_2\}) = \sigma(R_2)[\mathbf{B}_{H\alpha}(\{U, R_2\}) - \mathbf{B}_{H\alpha}(\{\epsilon, R_2\})]. \qquad (41)$$

---

[8]If both transition energies are well inside the bias window, the small coupling asymmetry $\Lambda \approx 0$ considered in Sec. IV implies that all possible dot states become equally stable or unstable in the stationary limit of this strongly bias driven configuration, $|z\rangle \to |\mathbb{1}\rangle/4$. Then $|z^i\rangle \to |z\rangle$, but since $|z\rangle \to |\mathbb{1}\rangle/4$ results in a vanishing gradient $\nabla_R|z\rangle \to 0$, the overlap (35) still approximately vanishes.

[9]For notational simplicity, here and in the following we will drop the units of parameters occurring in $\mathbf{R}$ and $\bar{\mathbf{M}}$, as introduced in Sec. II B.

[10]For notational simplicity, here and in the following we will drop the third component of $\mathbf{R}$, which is always zero.
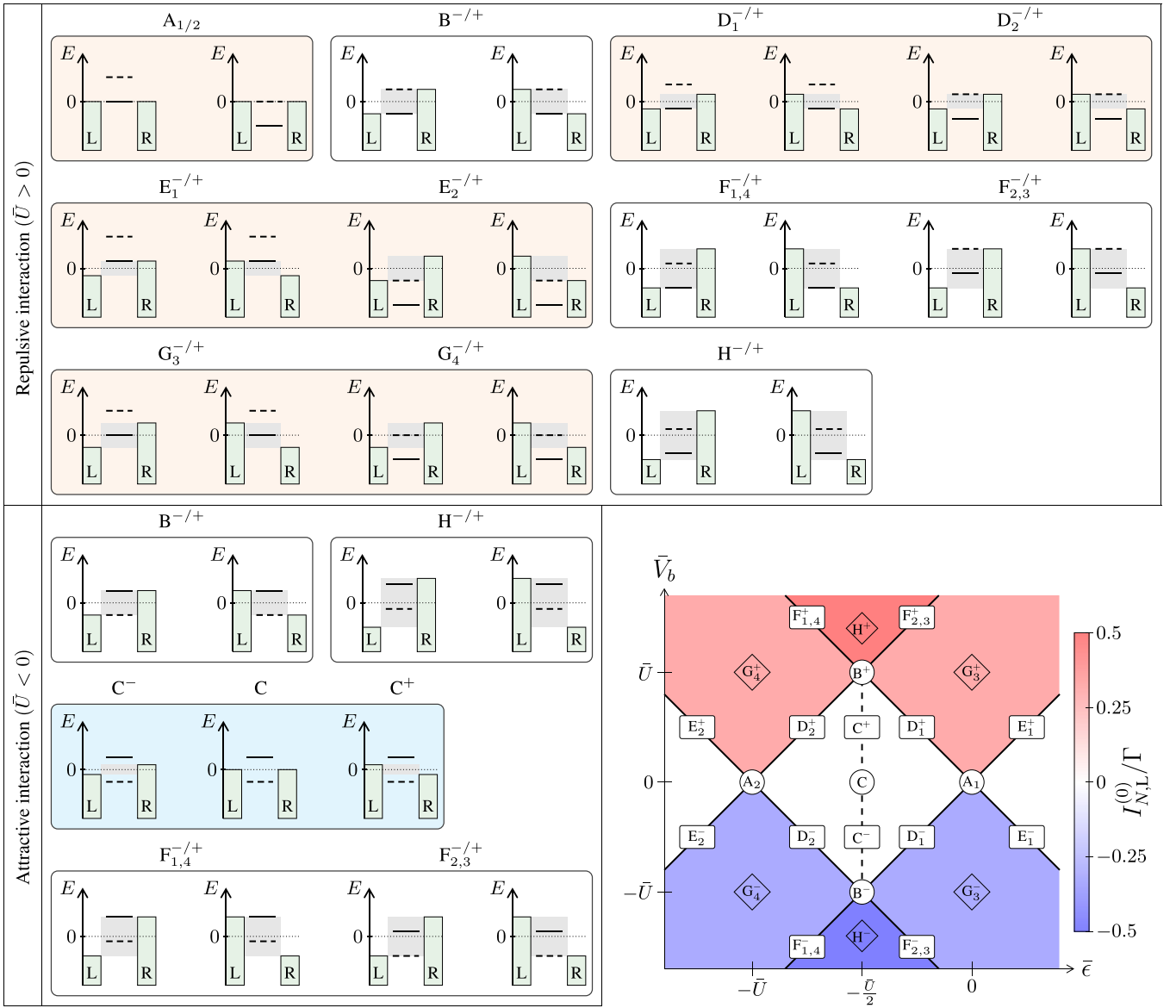
FIG. 2. Electrochemical potential configurations corresponding to the discussed pumping mechanisms (see Table I) for a repulsive interaction (top rows) and an attractive one (bottom rows). The solid black line indicates the transition energy ϵ, while the dashed one corresponds to $\epsilon + U$. The mechanisms specific to the repulsive case are highlighted in light orange, while the one specific to the attractive case is highlighted in light blue. The mechanisms are also indicated on a map of the parameter space $(\bar{\epsilon}, \bar{V}_b)$ in the bottom-right corner, with circles for points at double resonances, the rectangles for lines of single resonances, and diamonds for surfaces, namely, regions in the absence of resonance. The colormap indicates the stationary current from the left reservoir into the quantum dot, $I_{NL}^{(0)}$. For simplicity, the sketch is done for zero-temperature reservoirs.

In the special case in which we drive $R_1 = \epsilon$ and $R_2 = U$, this results in

$$\mathcal{T}\mathbf{B}_{H\alpha}(\{\epsilon, U\}) = -\mathbf{B}_{H\alpha}(\{\epsilon, U\}). \tag{42}$$

The above argument also straightforwardly extends to charge pumping. The only difference is that unlike for the energy observable $\hat{H}$, the transform $\mathcal{T}$ has no effect on the dot occupation operator $\hat{N}$ itself. As a result, the charge pumping curvature relations analogous to Eqs. (39), (42), and (41) all have an additional minus sign on their respective right-hand sides (see Appendix C 1).

Finally, it is interesting to note that while we have physically determined Eqs. (39), (42), and (41) for the full curvatures, we also find these relations to hold separately for the charge and parity components $\mathbf{B}_{H\alpha}^{\text{P/C}}(\mathbf{R})$. This is because, up to an overall sign, $\mathcal{T}$ also acts as a particle-hole transform on each left and right eigenvector of the kernels W and W^{α} individually.

IV. CHARACTERISTICS OF ENERGY PUMPING

We now proceed with a detailed analysis of energy pumping based on the analytical results obtained using fermionic duality in the previous sections. We show plots of the

TABLE I. Description of the different pumping mechanisms.

Mechanism	Description
A	Double resonance at zero bias voltage
B	Double resonance at $|\bar{V}_b| = |\bar{U}|$
C	Particle-hole symmetric point, namely, $\bar{\epsilon} = -\bar{U}/2$
D	Single resonance on the side of the Coulomb diamond (bias window in between the two transition energies)
E	Single resonance while the bias window is not in between the transition energies
F	Single resonance while the other transition energy lies within the bias window
G	Single transition energy in the bias window
H	Both transition energies in the bias window

energy pumping curvature $\mathbf{B}_{HR}(\mathbf{R})$ of the right contact for all different driving schemes in Figs. 3 and 4. Figures 7 and 8 in Appendix D also display the corresponding charge pumping curvatures $\mathbf{B}_{NR}(\mathbf{R})$ for relevant comparisons between charge and energy pumping. These pumping curvatures are calculated by setting $\alpha = \mathrm{R}$ and $\hat{\mathcal{O}} = \hat{N}, \hat{H}$ in Eq. (30), namely,

$$\mathbf{B}_{NR}(\mathbf{R}) = \mathbf{B}_{NR}^{\mathrm{C}}(\mathbf{R}) = \boldsymbol{\nabla}_{\mathbf{R}} \frac{\gamma_{\mathrm{cR}}}{\gamma_{\mathrm{c}}} \times \boldsymbol{\nabla}_{\mathbf{R}} N_z \qquad (43)$$

and

$$\mathbf{B}_{HR}^{\mathrm{C}}(\mathbf{R}) = \boldsymbol{\nabla}_{\mathbf{R}} a_{HR}^{\mathrm{C}} \times \boldsymbol{\nabla}_{\mathbf{R}} N_z,$$
$$\mathbf{B}_{HR}^{\mathrm{P}}(\mathbf{R}) = \boldsymbol{\nabla}_{\mathbf{R}} a_{HR}^{\mathrm{P},p} \times \boldsymbol{\nabla}_{\mathbf{R}} p_z + \boldsymbol{\nabla}_{\mathbf{R}} a_{HR}^{\mathrm{P},N} \times \boldsymbol{\nabla}_{\mathbf{R}} N_z, \qquad (44)$$

where the coefficients a are given by Eqs. (31).

Furthermore, for sufficiently small driving amplitudes, the geometric phase can be approximated by the bilinear response $\Delta \mathcal{O}_\alpha^{(1)} \approx \mathbf{B}_{\mathcal{O}_\alpha}(\mathbf{R}) \cdot \delta \mathbf{S}$, where the vector $\delta \mathbf{S}$ is orthogonal to the surface $\mathcal{S}$ and has the encircled area of $\mathcal{S}$ as its norm [Fig. 1(b)]. Therefore, in this limit, the amount of pumped energy or charge per driving cycle is directly proportional to the pumping curvature plotted in the figures.

A. Quantum dot with repulsive on-site interaction

The energy pumped through the quantum dot per driving cycle shows a very rich behavior as a function of the driving parameters as well as of the constant working-point parameters. In Fig. 3 we show the pumping curvature for the energy pumped through the quantum dot with repulsive on-site interaction for all possible choices of pairs of driving parameters (indicated by $\mathbf{R}$ on top of each panel). All curvatures are plotted as functions of the working-point dot level position $\bar{\epsilon}$ and bias voltage $\bar{V}_b$. This choice of representation is motivated by the fact that it allows all features to be compared to the well-known Coulomb diamonds characterizing the steady-state transport through interacting quantum dots. We set the average temperature to be equal in both contacts $\bar{T}_\mathrm{L} = \bar{T}_\mathrm{R} \equiv T$ and much smaller than the average Coulomb interaction $\bar{U} = 30T$, a regime where Coulomb interaction effects are dominant and clearly visible. For simplicity, the working-point coupling asymmetry is furthermore chosen to be zero, $\bar{\Lambda} = 0$.

1. Specific features of energy pumping and comparison to charge pumping

As discussed on a formal level in Sec. III B 3, we observe that the energy pumping curvature presented in all panels of Fig. 3 is particle-hole symmetric or antisymmetric depending on the driving scheme, except if U is one of the driving parameters. Furthermore, in comparison with charge pumping (see Appendix D), we identify a number of different pumping mechanisms (see also Sec. III B 2) with features specific to energy pumping. Generally, we find features at double resonances, in particular at those crossing points of the Coulomb diamonds, which we classify as mechanism B, at single resonances, namely, the lines confining the Coulomb diamonds, which are due to mechanisms D, E, and F, as well as nonresonant features, appearing in the surfaces outside the Coulomb diamonds, classified as mechanisms G and H.

We start by discussing the features that occur when the coupling asymmetry is kept constant $\Lambda = \bar{\Lambda}$, beginning specifically at zero bias voltage, which is with mechanism A. This mechanism, at a double resonance with an equilibrium environment, is one of the mechanisms in charge pumping with the largest magnitude (see Refs. [6,31] and Appendix D). By contrast, the pumped energy precisely at these points is vanishingly small. One rather finds that any feature occurring in the vicinity of $\bar{V}_b/T = 0$ is not due to a unique double-resonance mechanism, but rather occurs as part of the lines associated with mechanisms D and E, which require a single resonance only, as further discussed below. The reason for this is the mostly tightly coupled energy flow [see Sec. III B 1 and in particular Eq. (31a)]

$$\mathbf{A}_{H\alpha}(\mathbf{R}) \approx \left(\frac{\mathcal{E}^\alpha \gamma_{\mathrm{c}\alpha}}{\gamma_{\mathrm{c}}} \right) \boldsymbol{\nabla}_{\mathbf{R}} N_z, \qquad (45)$$

which yields the characteristic energy $\mathcal{E}^\alpha$ related to the Seebeck coefficient [Eq. (33)] as the dominant contribution to the energy current in a near-equilibrium environment. Since this energy coefficient is suppressed close to the resonances, so is the energy effectively carried by the pumped charge.

The situation is reversed for mechanism B, corresponding to a double resonance with a large bias $|V_b| \approx |U|$, where not only the charge mode but also the parity mode starts to contribute to energy transport (see Sec. III B 1). At this double resonance, driving any parameter other than Λ leads to pumping mostly by changing the balance between transport at one resonance with energy ϵ vs the other one with energy $\epsilon + U$. This has a negligible effect on the net charge transport as long as the coupling is symmetric, but it does affect the transported energy stemming from two resonances, with equally important chargelike and paritylike contributions (see also Sec. IV A 2).

As a next step, we analyze the most common single-resonance features in the pumped energy, namely, the lines occurring due to mechanisms D–F. While strongly suppressed in charge pumping for any driving scheme apart from those involving Λ, energy pumping always exhibits at least some of those features except when only driving macroscopic variables T_L and V_b. To understand this, we note that for all these mechanisms with constant Λ, the rate of particle transport between the dot and the nonresonant lead α' is fixed in strength
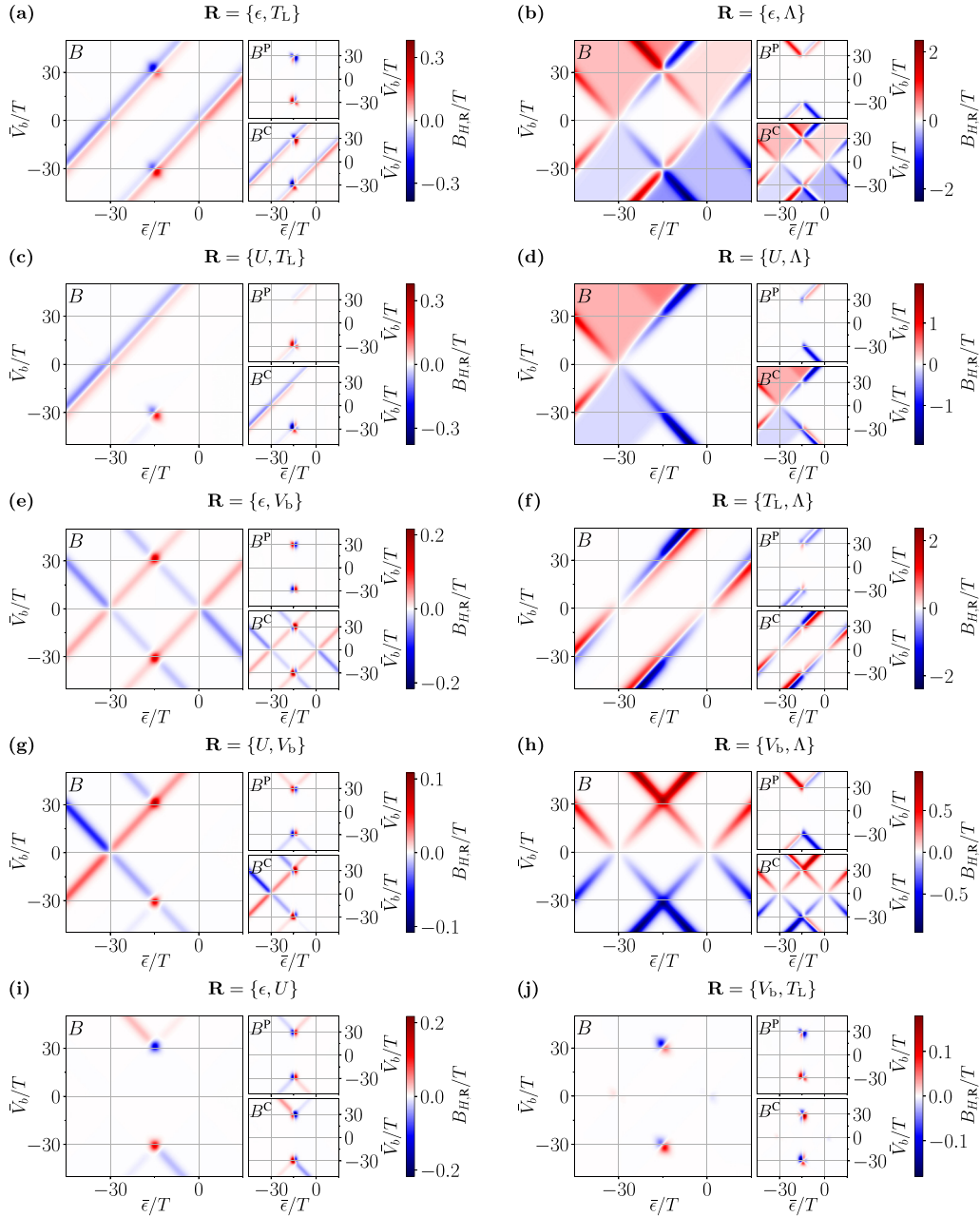
FIG. 3. Pumping curvatures $\mathbf{B}_{H\mathbf{R}}$ of the repulsive system ($\bar{U} > 0$) in the ($\bar{\epsilon}, \bar{V}_\mathrm{b}$) space for all possible two-parameter driving schemes $\mathbf{R} = \{R_1, R_2\}$. We have plotted the relevant component of $\mathbf{B}_{H\mathbf{R}}$, which is the one perpendicular to the driving plane defined by (R_1, R_2), in units of T. In each subfigure, the largest panel corresponds to the total pumping curvature, the top right one to the parity contribution $\mathbf{B}_{H\mathbf{R}}^{\mathrm{P}}$, and the bottom right one to the charge contribution $\mathbf{B}_{H\mathbf{R}}^{\mathrm{C}}$. The driving is done around the working point $\bar{\mathbf{M}} = (\bar{\epsilon}, \bar{U}, \bar{V}_\mathrm{b}, \bar{T}_\mathrm{L}, \bar{\Lambda})$ with $\bar{\Lambda} = 0$, $\bar{T}_\mathrm{L} = \bar{T}_\mathrm{R} = T$, and $\bar{U} = 30T$. We have taken $\mu_{\mathrm{L/R}} = \pm V_\mathrm{b}/2$, with the reference chemical potential μ_0 set to zero.

and direction, i.e., $\partial_{R_i} W^{\alpha'} \approx 0$, since the transport resonance lies either significantly below or above the respective chemical potential $\mu_{\alpha'}$ on the scale of the temperature. This results in the driving of only one effective parameter associated with the near-resonant lead α around a steady-state value at the working point [6]. The charge current therefore averages out over one cycle (see Appendix G for an explicit derivation).

Conversely, the net pumped energy for the single-resonance mechanisms D–F can still be finite when work done on the particles, via driven local dot energies ϵ and/or

U, affects the transported energy time dependently (see also Appendix E). This formally corresponds to the direct (ϵ, U) dependence of the prefactors a in the geometric connection for energy pumping [Eqs. (31)], i.e., not the one entering implicitly via the occupation numbers, which depend on time only at resonance. A nonzero cycle-averaged pumped energy moreover requires the energy during a particle transfer from the resonant lead to differ from the energy for the corresponding reversed process *to* the lead at the same rate. This asymmetry is established by the second driving parameter next to ϵ or U.
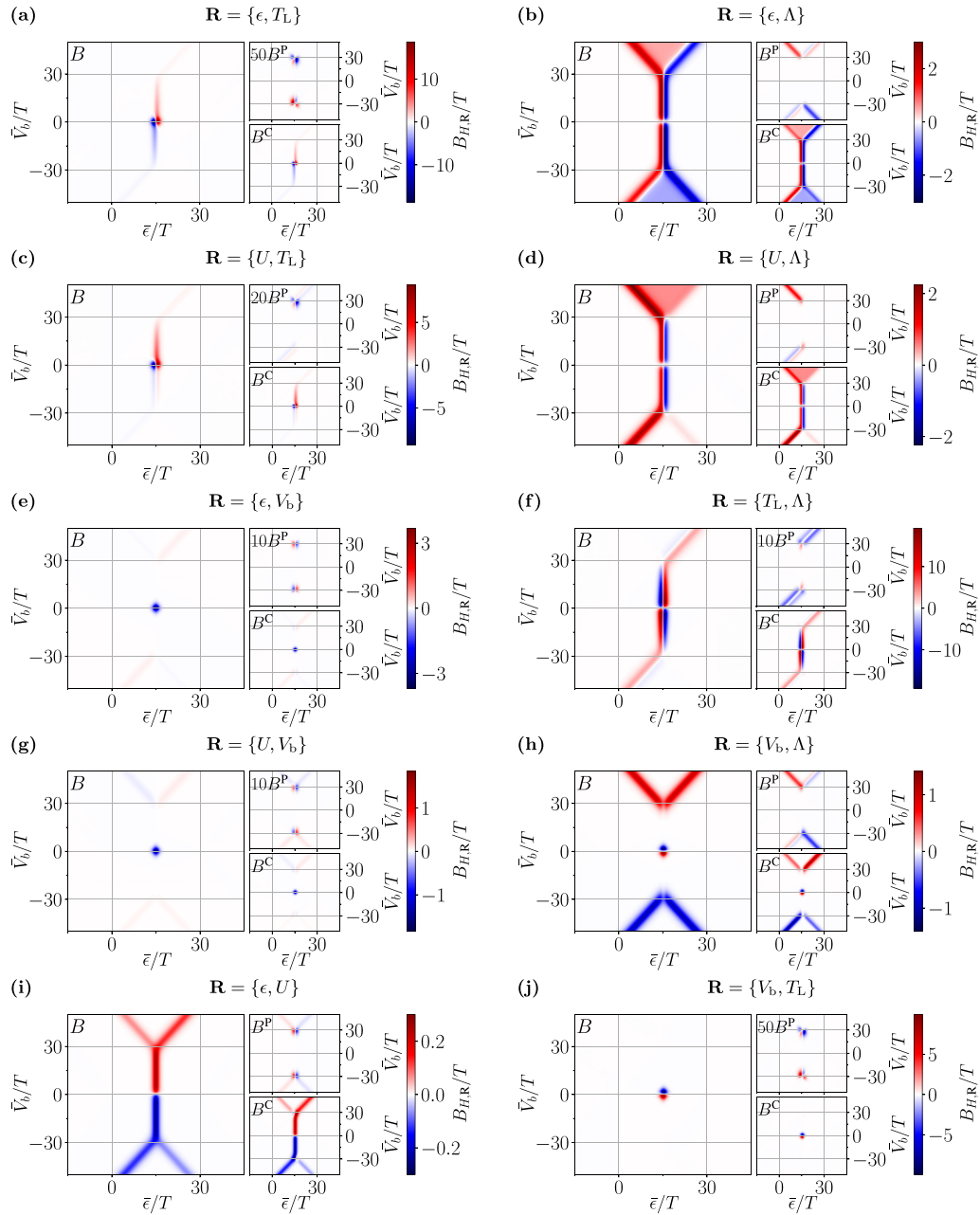
FIG. 4. Pumping curvature $\mathbf{B}_{H\mathrm{R}}$ of the attractive system ($\bar{U} < 0$) in the ($\bar{\epsilon}, \bar{V}_\mathrm{b}$) space for all possible two-parameter driving schemes $\mathbf{R} = \{R_1, R_2\}$. We have plotted the component of $\mathbf{B}_{H\mathrm{R}}$ perpendicular to the driving plane defined by (R_1, R_2), in units of T. In each subfigure, the largest panel corresponds to the total pumping curvature, the top right one to the parity contribution $\mathbf{B}_{H\mathrm{R}}^\mathrm{P}$, and the bottom right one to the charge contribution $\mathbf{B}_{H\mathrm{R}}^\mathrm{C}$. Here $\mathbf{B}_{H\mathrm{R}}^\mathrm{P}$ has been multiplied by a factor indicated in each panel to make its features visible using the same color scale as in the other panels. The parameters are the same as in Fig. 3, except that $\bar{U} = -30T$.

We also show pumping curvatures for a noninteracting dot in Appendix F, providing even simpler examples of how work done on the electron in the dot in resonance with a single lead results in finite energy pumping in the absence of charge pumping. By contrast, since driving the lead parameters alone does not do any work on the transferred particles, we accordingly find that $\mathbf{B}_{H\alpha}(\{V_\mathrm{b}, T_\mathrm{L}\})$ vanishes for the single-resonance mechanisms. This is evident from Fig. 3(j) and formally derived in Appendix G.

A particularly striking case in which work done on the dot electrons causes nonzero energy pumping curvatures

$\mathbf{B}_{H\alpha}(\mathbf{R}) \neq 0$ in the absence of cycle-averaged charge pumping is the driving scheme involving only dot parameters, $\mathbf{R} = \{\epsilon, U\}$ [Fig. 3(i)]. Here mechanisms B and F yield finite energy pumping without charge pumping for the reasons explained above. Charge pumping, on the other hand, can in any case only occur for mechanisms A and B, at double resonances. With mechanism B already ruled out, we find that mechanism A also cannot contribute to the curvature $\mathbf{B}_{N\alpha}(\{\epsilon, U\})$ because the dot is coupled to a constant equilibrium environment $V_\mathrm{b} = T_\mathrm{L} - T = 0$ during the entire driving cycle. The two leads $\alpha = \mathrm{L,R}$ individually act equivalently to

the sum of leads and the transport situation is fully symmetric. Hence, the cycle-averaged particle current vanishes (see Appendix E).

The comparison between charge and energy pumping changes when the couplings Γ_α are driven via their relative asymmetry Λ, as apparent in the explicit formulas given in Appendix G, in particular Eqs. (G9) and (G11). First, the pumped charge for mechanisms D–F at a single resonance is generally finite (see Fig. 7 in Appendix D). The nonvanishing cycle average stems from the fact that the tunneling asymmetry $\Lambda(t)$ enters the time-dependent charge current nonlinearly, regardless of the resonance with the lead α. This is because $\Lambda(t)$ influences the tunneling current both directly, via the tunneling rates themselves, and indirectly, by affecting the relative influence of each lead on the dot state.

A second characteristic of Λ driving which clearly distinguishes energy pumping from charge pumping is the surface features due to mechanisms G and H, appearing for ϵ or U as second driving parameter [Figs. 3(b) and 3(d)]. These plateaus correspond to a completely nonresonant situation outside the Coulomb diamond, in which the kernels of both leads $\alpha =$ L,R and their derived quantities (apart from $N_{z\alpha}^i$) are independent of any parameter except the couplings, i.e., $\partial_{R_i} W^\alpha / \Gamma \approx \partial_{R_i} W / \Gamma \approx \partial_{R_i} \gamma_{c\alpha} / \Gamma \approx \partial_{R_i} N_{z\alpha} \approx 0$ for $R_i \neq \Lambda$. Since the charge pumping curvature [Eq. (43)] depends on the parameters exclusively through these quantities, driving Λ and any other parameter $R_i \neq \Lambda$ effectively equals single-parameter geometric driving with Λ only, which vanishes by definition. By contrast, a nonzero pumped energy is still possible because it directly depends on ϵ and U via the tight-coupling energy $\mathcal{E}^\alpha$ given in Eq. (33). The physical explanation again lies in the work done on the dot electrons. Namely, while a modulation of Λ does not affect how much charge is transported across the dot in one cycle, a simultaneous modulation of Λ and ϵ or U still means that the energy taken out of one lead by a particle hopping to the dot is not the same as the energy which the same particle carries when hopping to the other lead.

Finally, let us end this section with a remarkable similarity between charge and energy pumping which occurs for temperature driving: Compared to the case of constant temperature, all single- and double-resonance features exhibit additional sign changes within the feature itself [Figs. 7(a), 7(c), 7(f), and 7(j) and Figs. 3(a), 3(c), 3(f), and 3(j)], that is, when the transition energy $\bar\epsilon$ or $\bar\epsilon + \bar U$ crosses the resonance with the left lead ($\bar\mu_L = \bar V_b/2$). Indeed, a temperature change always affects the lead-electron occupation asymmetrically around the chemical potential: Driving the temperature to, e.g., a slightly higher value, the chance of finding electrons at some energy $E - \mu_L > 0$ above the chemical potential rises, whereas the probability for electrons at $-(E - \mu_L) > 0$ below this potential lowers by the same amount. Consequently, the temperature-driving effect on electron transport to or from the lead is inverted when crossing the resonance and as such it affects both the pumped charge and energy.

2. Paritylike contributions to energy pumping

Our general analysis in Sec. III B 1 has already revealed, on a formal level, that for the case of strong repulsive interactions $U \gg T_\alpha$ relevant here, paritylike excitations only enter at large bias $|V_b| \gtrsim U$ and with at least one of the two dot transition energies ϵ and $\epsilon + U$ being nearly resonant with one of the lead potentials. The two smaller side panels of every subfigure of Fig. 3, which show the chargelike $\mathbf{B}_{HR}^C(\mathbf{R})$ and paritylike $\mathbf{B}_{HR}^P(\mathbf{R})$ contributions to the pumping curvature separately, explicitly confirm this behavior. Namely, we observe paritylike contributions at pointlike features around double resonances at $\bar V_b = |\bar U|$ (mechanism B) with U and Λ constant or at linelike features when U or Λ are among the driving parameters (mechanism F). In the following, we further elucidate these features.

As explained above, a constant Λ with only a single resonant lead implies that any finite cycle-averaged energy transport due to the time-dependent driving must involve work done on the dot electrons. For constant U, this means that ϵ must be a driving parameter and as such this driving modifies both transition energies ϵ and $\epsilon + U$ equally. The energy transferred in addition to the steady-state energy current is hence tightly coupled to the charge transported back and forth between the dot and resonant lead, i.e., each particle on average carries the same amount of pumped energy. Consequently, the parity component to the pumping curvature disappears for mechanism F with constant U and Λ [Figs. 3(a), 3(e), and 3(j)].

For mechanism B with the dot in resonance with both leads, any two driving parameters generally affect the balance between electron transfer at energy ϵ and energy $\epsilon + U$. The paritylike contribution to this energy pumping is then determined by how much pumped energy is transferred near a state of maximal instability (this is a well-defined concept in the vicinity of the special points $|\bar V_b| = |\bar U|$); the dot state in fact rapidly switches between empty and doubly occupied when crossing the double resonance. In other words, the large bias voltage provides a finite probability even for slow driving to excite transport near maximal instability.

A driven U differs from the other parameters in that it selectively affects only transport with transition energy $\epsilon + U$. Even in the single-resonance case for mechanism F, the driving-induced time-dependent deviation from the steady-state energy current thereby generates non-tightly-coupled contributions, i.e., not every transported charge carries the same energy, allowing the parity mode to contribute [see Eqs. (31b) and (31c)]. A driven coupling asymmetry Λ instead always equally affects the rates of transition via both energies ϵ and $\epsilon + U$, but as such still gives rise to paritylike time-dependent corrections to the energy current. Indeed, as stated before, a cycle-averaged contribution from these paritylike corrections only arises if they are accompanied by a resonant effect that modulates the balance between transport at the two transition energies ϵ and $\epsilon + U$. When driving only U and Λ, this demands a lead potential resonant with the transition energy $\epsilon + U$, explaining why the parity contribution due to mechanism F in Fig. 3(d) disappears for $\bar\epsilon < -\bar U/2$. Driving the temperature T_L of the left lead and U or Λ analogously requires a resonance with the left lead to give finite paritylike pumped energy per cycle so that $\mathbf{B}_{H\alpha}^P(\mathbf{R})$ vanishes for $\bar V_b > \bar U \gg T_L$ and $\bar\epsilon < -U/2$ as well as for $\bar V_b < -\bar U$ and $\bar\epsilon > -U/2$ [see Figs. 3(c) and 3(f)].

B. Quantum dot with attractive on-site interaction

We now analyze the same driving schemes as above for a quantum dot with an attractive on-site interaction $U < 0$ and we identify the major differences and similarities with the more standard case of a repulsive on-site interaction. Results for the energy pumped through a quantum dot with $U < 0$ are shown in Fig. 4 for the different driving schemes. We consider similar working points as previously, namely, $\bar{T}_L = T$, $\bar{\Lambda} = 0$, and $\bar{U} = -30T$, and plot the curvatures in the $(\bar{\epsilon}, \bar{V}_b)$ space.

1. Specific feature of attractive on-site interaction: Two-particle resonance

A unique feature of attractive on-site interaction is the pairing-induced two-particle resonance at the particle-hole symmetric point $\epsilon = -U/2$ [78]. At this point, when $\Lambda = 0$ and $T_L = T$, the dot switches from a stable empty state (for $\epsilon/T \gg -U/2T$) to a stable double occupation (for $\epsilon/T \ll -U/2T$), regardless of bias voltage (up to $V_b \approx |U|$). Interestingly, this transition in the dot occupation N_z still occurs around $\epsilon/T \approx -U/2T$ and depends little on V_b, even for small but finite coupling asymmetries and temperature differences.

As justified in Sec. III B 1, only the charge mode contributes to the energy pumping for $|V_b| < |U|$, namely, $\mathbf{B}_{H\alpha}(\mathbf{R}) \approx \nabla_{\mathbf{R}} a^C_{H\alpha} \times \nabla_{\mathbf{R}} N_z$. Therefore, as visible in Fig. 4, the energy pumping curvatures exhibits features only along this two-particle resonance line for these biases, corresponding to the mechanism C defined in Sec. III B 2. However, the charge pumping, which has already been addressed in detail in Ref. [71] for $U < 0$, only happens for $|V_b|/T \approx 0$ and $\epsilon/T \approx -U/2T$ (see Fig. 8 in Appendix D).

In this section we compare charge and energy pumping close to the two-particle resonance $\epsilon/T \approx -U/2T$ and we start by analyzing the pumping curvatures close to zero bias voltage $V_b/T \ll 1$. First and foremost, energy pumping cannot be understood by simply relating it to charge pumping. As a matter of fact, unlike for a repulsive on-site interaction, the contribution $\nabla_{\mathbf{R}} a^{C,TC}_{H\alpha} \times \nabla_{\mathbf{R}} N_z$, tightly coupled to charge pumping [Eq. (32a)], does not dominate the energy pumping curvature. On the contrary, the features of the energy pumping curvature mostly arise from the non-tightly-coupled contribution $\nabla_{\mathbf{R}} a^{C,NTC}_{H\alpha} \times \nabla_{\mathbf{R}} N_z$ [Eq. (32b)], even at $|V_b|/T \approx 0$. This contribution is however less straightforward to interpret for $U < 0$ than for $U > 0$ since it contains the ratio of $N^i_{z\alpha} - N^i_z$ and γ_c, which is finite while both quantities individually are suppressed for mechanism C. To understand better energy pumping, we therefore conduct an in-depth analysis of $\mathbf{B}_{H\alpha}(\mathbf{R})$ for every driving scheme based on expressions derived from the explicit formulas in Appendix H 2. In particular, we give analytical justifications of the features observed in Fig. 4, found to be as follows.

Focusing on mechanism C$^\pm$, at finite bias voltage $|U| > |V_b| > T$, we note that charge pumping is always suppressed, even though the system may be in a two-particle resonance with the combined two-lead system at $\bar{\epsilon} = -\bar{U}/2$. This is because even close to this resonance, the dot is nevertheless off resonance with both lead potentials individually, namely, $(\epsilon + U/2)/T \ll |\mu_\alpha|/T$. The time-dependent charge flow is then at most affected by a single driving parameter related to

the left-right balance of charge transfer, and single-parameter driving results in a vanishing cycle average (see Appendix H 1 for an analytical derivation).

Finite energy pumping for mechanism C$^\pm$ can, by contrast, still be achieved by doing work on the dot or by modulating the left-right lead coupling balance in a voltage-biased environment (see Appendix H 2). A crucial difference from the $|\bar{V}_b|/T \approx 0$ case occurs for a driven bias voltage V_b [Figs. 4(e), 4(g), 4(h), and 4(j)], which always features suppressed energy pumping. This originates from the fact that for $|V_b| > T$ any further modulation of an already symmetrically applied bias $|U| > |V_b(t)| > T$ has no bearing on either charge or energy transport via the two-particle resonance, i.e., for $\epsilon/T \approx -U/2T$. Driving V_b and any second parameter is hence equivalent to single-parameter driving even for the energy current, thereby prohibiting adiabatic pumping altogether.

2. Comparison to repulsive on-site interaction

We now look more generally at the features of energy pumping for a quantum dot with an attractive on-site interaction and compare it to the repulsive on-site interaction from Sec. IV A. First, the energy pumping curvature exhibits the same particle-hole symmetry or antisymmetry as in the repulsive case in each panel of Fig. 4, except if U is one of the driving parameters (Sec. III B 3). Furthermore, the parity-like component $\mathbf{B}^P_{H\alpha}(\mathbf{R})$ of the energy pumping curvature is very similar for both interaction signs, as revealed by comparing the top right panels in Fig. 3 to the corresponding panels in Fig. 4. In particular, $\mathbf{B}^P_{H\alpha}(\mathbf{R})$ for constant attractive interaction $\bar{U} < 0$ equals $\mathbf{B}^P_{H\alpha}(\mathbf{R})$ evaluated for repulsive interaction $-\bar{U} > 0$ and a working point $\bar{\epsilon}$ shifted by $\bar{U} = -|\bar{U}|$. This stems from a combination of the self-duality of $\mathbf{A}^P_{H\alpha}$ (Sec. III B 1) and the particle-hole symmetry relations (Sec. III B 3), as derived in details in Appendix C 2. The paritylike pumping contributions can thus be understood in the same way as discussed for the repulsive dot in Sec. IV A 2 and are not further discussed here.

We continue our comparison by noting that many mechanisms leading to charge or energy pumping for $U > 0$ are absent for $U < 0$. Indeed, due to the pairing induced by attractive interaction, any particle flow to and from the dot is almost always exponentially suppressed if at least one of the two dot transition energies ϵ and $\epsilon + U$ lies significantly outside the bias window on the scale of T. Accordingly, sizable contributions due to mechanisms A, D, E, and G are absent in both energy and charge pumping (see Figs. 4 and 8, respectively). On the contrary, mechanism C at the two-particle resonance $\bar{\epsilon} = -U/2$ is specific to attractive on-site interaction and the most relevant mechanism for both charge and energy pumping (Sec. IV B 1).

Mechanism B also does not contribute with distinct features as for $U > 0$, but rather appears as a continuation of mechanism C$^\pm$, with vanishing charge pumping but generally finite energy pumping. This is consistent with the fact that at $\bar{\epsilon} = -\bar{U}/2$ and strong attraction $-U \gg T$, an effective double-resonance situation with both leads combined is fulfilled not only for $|V_b| = |U|$ specifically, but for any bias voltage $|V_b| \leqslant |U|$.

We furthermore observe that mechanisms F and H contribute to energy pumping at large bias $|V_b| \gtrsim |U|$ in both cases. Since mechanism H corresponds to both dot transition energies ϵ and $\epsilon + U$ being inside the bias window, the sign of the interaction strength U loses its significance and we accordingly observe the same plateaus in the pumped energy as for repulsive interaction [see Figs. 4(b) and 4(d) and Figs. 3(b) and 3(d)]. The charge pumping curvature is likewise suppressed for both $U > 0$ and $U < 0$. The situation for mechanism F at constant U and Λ is again qualitatively very similar to the case of repulsive interaction for both charge and energy pumping. The difference is that for a working point $\bar{\epsilon}$ below/above the particle-hole symmetric point, it is not the energetically higher/lower dot transition energy as for $U > 0$, but instead the energetically lower/higher energy that is in resonance with one of the leads. While irrelevant for constant U, a time-dependent $U(t) < 0$ does yield a different pumped energy than for $U(t) > 0$ because of this distinction. This can be seen by, e.g., comparing (ϵ, U) driving in Fig. 4(i) to Fig. 3(i). Repulsive interaction here features a larger magnitude of pumped energy for $\bar{V}_b > 0$ and $\bar{\epsilon} + \bar{U}/2 < 0$ as well as $\bar{V}_b < 0$ and $\bar{\epsilon} + \bar{U}/2 > 0$, whereas attractive interaction yields a larger pumping current with the sign of $\bar{\epsilon} + \bar{U}/2$ reversed.

The driving scheme $\mathbf{R} = \{\epsilon, U\}$ gives similar results for both signs of the interaction: Charge pumping is suppressed [Fig. 8(i)] due to the constant equilibrium environment of the dot while energy can still be pumped [Fig. 4(i)]. The reason is that the (ϵ, U) driving does work on the particles while temporarily occupying the dot. However, unlike for $U > 0$, energy pumping also happens at biases $|V_b| < |U|$ due to mechanism C (see Sec. IV B 1).

Addressing the effect of driven coupling asymmetry, the obvious difference between repulsive and attractive interactions is that while the pumped energy is qualitatively the same for both interaction signs [Figs. 4(b), 4(d), 4(f), and 4(h) and Figs. 3(b), 3(d), 3(f), and 3(h)], net cycle-averaged charge pumping [Figs. 8(b), 8(d), 8(f), and 8(h) and Figs. 7(b), 7(d), 7(f), and 7(h)] is finite only for $U > 0$ but suppressed for $U < 0$. The reason for this is the same as for mechanism C$^{\pm}$: With both lead potentials away from the two-particle resonance, the driving has no additional effect on top of the bias-induced stationary charge flow when averaged over a cycle, but it can still affect the net energy of electrons passing through.

Finally, when driving the temperature, like for $U > 0$, there is a sign change in the feature at the single resonance with the left lead, but only for mechanism F since D and E are suppressed [Figs. 4(a), 4(c), and 4(f)]. However, the effect is less visible due to the high values of the pumping curvature for mechanism C. As discussed previously, the intensity of the branches, above and below the resonance with the left lead, is reversed since the transition energies are also inverted.

V. REFRIGERATOR AND HEAT PUMP

The regime of slow driving studied here is especially interesting for periodically driven thermal machines [48,108]. Therefore, in this section we analyze the device as a cyclic thermal machine, intended to further cool a bath colder than its environment (refrigerator) or to further heat a bath warmer than its surrounding (heat pump). The working substance is the quantum dot itself and the contacts represent the hot and cold baths, assuming equal chemical potential $V_b = 0$. We use the results from Secs. III and IV specific to these parameters to identify interesting driving operation points and to gain insights into the mechanisms at play.

A. Driving scheme and thermodynamic quantities

As a paradigmatic (but not the only possible) way to achieve refrigeration or heat pumping, we consider the driving scheme (ϵ, Λ),

$$\epsilon(t) = \bar{\epsilon} + \delta\epsilon \sin(\Omega t), \quad \Lambda(t) = \delta\Lambda \sin(\Omega t + \phi), \quad (46)$$

which moves the dot potential $\epsilon(t)$ while modulating the left-right tunnel coupling asymmetry $\Lambda(t)$ with a driving phase ϕ relative to $\epsilon(t)$. As an illustrative example, let us for a moment assume an amplitude $\delta\Lambda = 1$, tuning the dot all the way from only coupled to the cold bath and decoupled from the hot bath to the opposite configuration, only coupled to the hot bath. For an appropriately chosen ϕ, this enables us to pump electrons against a temperature difference, making the device operate as a refrigerator or heat pump as sketched in Fig. 1(c). Namely, in step (I), the dot is only coupled to the cold bath while its transition energy is lowered below the Fermi level to let an electron tunnel in. The dot is then decoupled from the cold bath and coupled to the hot bath in step (II). Step (III) increases the dot transition energy above the Fermi level so that the electron tunnels into the hot bath. The final step (IV) completes the cycle, reverting to a dot only coupled to the cold bath.

To be in the adiabatic-response regime, the driving frequency Ω as well as the amplitudes $\delta\epsilon$ and $\delta\Lambda$ are chosen such that $\Omega\delta\epsilon/T, \Omega\delta\Lambda \ll \Gamma$. The targeted heat pump and refrigerator driving cycles operate at zero bias voltage $V_b = 0$, but are meaningful if a small but finite temperature difference $\bar{T}_L = T + \delta T$ and $\bar{T}_R = T$ with $0 < |\delta T| \ll T$ exists, unlike $|\delta T| = 0$ considered in Sec. IV. The device performance is quantified via the heat $\mathcal{Q}_R$ emitted or absorbed to/from the right reservoir and via the work $\mathcal{W}$ provided to the device by the external driving, both in one driving cycle. In this setting, the refrigerator (heat pump) operation mode corresponds to $\delta T > 0$ and $\mathcal{Q}_R > 0$ ($\delta T < 0$ and $\mathcal{Q}_R < 0$). The average cooling power is given by $\mathcal{Q}_R \Omega / 2\pi$ and the coefficient of performance is defined as

$$\eta = \left| \frac{\mathcal{Q}_R}{\mathcal{W}} \right|, \quad (47)$$

whenever $\mathcal{Q}_R$ has the desired sign, while we set $\eta = 0$ otherwise. The corresponding Carnot efficiency reads

$$\eta_{\text{Carnot}} = \frac{T}{|\delta T|}. \quad (48)$$

Since $\mu_R = 0$, the heat current coincides with the energy current I_{HR} (Appendix A), so the heat $\mathcal{Q}_R$ can be expressed, up to the first-order correction, as $\mathcal{Q}_R = \mathcal{Q}_R^{(0)} + \mathcal{Q}_R^{(1)}$ with

$$\mathcal{Q}_R^{(\ell)} = \Delta H_R^{(\ell)} = \int_0^{2\pi/\Omega} dt\, I_{HR}^{(\ell)}(t), \quad (49)$$

where $I_{HR}^{(\ell)}(t)$ is defined in Eq. (19) with $\hat{O} = \hat{H}$. The zeroth-order $\mathcal{Q}_R^{(0)}$ stems from the instantaneous stationary heat flow $I_{HR}^{(0)}(t)$ induced by the temperature difference between the contacts; it is hence proportional to Γ/Ω and always detrimental to the device operation, since heat always flows from the hot to the cold bath in the steady state. The first-order correction $\mathcal{Q}_R^{(1)}$, on the other hand, describes the geometric pumping contribution. It is independent of both total coupling strength Γ and driving frequency Ω, and an appropriate driving phase ϕ between $\epsilon(t)$ and $\Lambda(t)$ results in a finite cycle-averaged heat pumped from the cold to the hot contact.

The work can be split into two contributions[11] $\mathcal{W} = \mathcal{W}_\epsilon + \mathcal{W}_\Lambda$ coming from the driving of each parameter. With $\mathcal{W}_\Lambda \to 0$ in the weak-coupling regime,[12] the work is done exclusively by the ϵ driving,

$$\mathcal{W}_\epsilon = \int_0^{2\pi/\Omega} dt (\partial_t H | \rho(t)) = \sum_{\ell > 0} \mathcal{W}_\epsilon^{(\ell)}, \qquad (50)$$

where the factor $\partial_t \hat{H} = \dot{\epsilon}(t) \hat{N}$ suppresses the $\ell = 0$ term $\sim \Gamma/\Omega$ in the driving-frequency expansion in orders

$$\mathcal{W}_\epsilon^{(\ell)} = \int_0^{2\pi/\Omega} dt\, \dot{\epsilon}(t) (N | \rho^{(\ell-1)}(t)). \qquad (51)$$

Unlike for $\mathcal{Q}_R$, we cannot truncate the series (50) already at the first-order correction ($\ell = 1$), despite the slow driving. Appendix I specifically shows that $\mathcal{W}_\epsilon^{(1)}$ is of first order in δT, whereas $\mathcal{W}_\epsilon^{(2)}$ contains a zeroth-order term in δT, making $\mathcal{W}_\epsilon^{(2)}$ the dominant contribution to the coefficient of performance (47) for $0 < |\delta T|/T \ll 1$. In fact, it was recently shown on more general grounds [110] that a first-order expansion in both temperature difference δT and driving frequency Ω is typically not sufficient to adequately estimate the performance of a thermal machine.

B. Limit of small driving amplitudes

With a full analysis of work $\mathcal{W}_\epsilon$, heat $\mathcal{Q}_R$, and performance η of the quantum-dot device following in Sec. V C, we first gain further analytical insight by considering only small driving amplitudes such that $\delta\epsilon/T, \delta\Lambda \ll 1$ allows us to Taylor expand all quantities up to leading order in these amplitudes. The vanishing bias voltage $V_b = 0$, the assumption of strong interaction $|U|/T \gg 1$, and the small temperature difference $|\delta T| \ll T$ furthermore enable us to use the linear-response results from Ref. [81] and the general steady-state linearization approach from Ref. [79] to expand all quantities up to linear order in δT.

Based on our findings from Sec. III A, we derive in Appendix I that the heat contributions for $|U| \gg T$ are, up to

leading order in δT, given by

$$\mathcal{Q}_R^{(0)} \approx \frac{2\pi}{\Omega} \left[\left(\mathcal{E}^{eq} I_{NR}^{(0)} - \kappa \delta T \right) \left(1 - \frac{(\delta\Lambda)^2}{2} \right) \right. $$
$$\left. + \frac{\delta\epsilon^2}{4} \left[\mathcal{E}^{eq} \partial_\epsilon^2 I_{NR}^{(0)} + \partial_\epsilon I_{NR}^{(0)} - (\partial_\epsilon^2 \kappa) \delta T \right] \right] + O(\delta T^2),$$

$$\mathcal{Q}_R^{(1)} = \mathbf{B}_{HR}(\mathbf{R}) \cdot \delta \mathbf{S} \approx -\frac{\delta N_{eq}^2 \mathcal{E}^{eq}}{2} \delta S + O(\delta T). \qquad (52)$$

The heat thereby depends on the Seebeck energy $\mathcal{E}^{eq}$, on the Fourier heat [81]

$$\kappa|_{\Lambda=0} = \frac{1}{4} \gamma_p \delta N_{eq}^2 \left(\delta N_{eq}^i \right)^2 \frac{U^2}{4T^2}, \qquad (53)$$

on the oriented driving surface $\delta S = \iint_\mathcal{S} d\Lambda(d\epsilon/T) = -\pi \sin(\phi)(\delta\epsilon/T)\delta\Lambda$, and on the stationary charge current, defined by the $\ell = 0$ component of Eq. (19):

$$I_{NR}^{(0)} \approx -\frac{1}{4} \gamma_{c,eq} \delta N_{eq}^2 \mathcal{E}^{eq} \frac{\delta T}{T^2} + O(\delta T^2). \qquad (54)$$

All of the above quantities depend on the equilibrium charge rate $\gamma_{c,eq}$, which determines the inverse RC time of the dot [83], and on the Seebeck energy $\mathcal{E}^{eq}$,

$$\gamma_{c,eq} = \gamma_c|_{\delta T, V_b = 0} = \left. \frac{\Gamma}{\Gamma_\alpha} \gamma_{c\alpha} \right|_{\delta T, V_b = 0},$$

$$\mathcal{E}^{eq} = \mathcal{E}^\alpha|_{\delta T, V_b = 0} = \epsilon + \frac{U}{2} \left(2 - N_{eq}^i \right), \qquad (55)$$

$$N_{eq}^i = N_z^i|_{\delta T, V_b = 0} = N_{z\alpha}^i|_{\delta T, V_b = 0},$$

as well as on the equilibrium charge fluctuations δN_{eq}^2,

$$\delta N_{eq}^2 = ((N - N_z)^2 | z)|_{\delta T, V_b = 0}. \qquad (56)$$

These are well known from the dc linear-response behavior of the dot [81] and here directly enter properties of the driven system. This includes the work $\mathcal{W}$ corresponding to the driving cycle, which reads (Appendix I)

$$\mathcal{W}_\epsilon^{(1)} = -\partial_\Lambda N_z T \delta S \approx -2T \frac{I_{NR}^{(0)}}{\gamma_{c,eq}} \delta S + O(\delta T^2),$$

$$\mathcal{W}_\epsilon^{(2)} \approx \pi \frac{\Omega}{\gamma_{c,eq}} \frac{\delta\epsilon^2}{T} \delta N_{eq}^2 + O(\delta T). \qquad (57)$$

In the limit $\delta T \to 0$, both reservoirs become identical and the stationary current vanishes $I_{N/HR}^{(0)} \to 0$. Therefore, $\mathcal{Q}_R^{(0)} \to 0$, $\mathcal{W}_\epsilon^{(1)} \to 0$, and

$$\mathcal{Q}_R^{(1)} \to \sin(\phi) \frac{\pi \delta N_{eq}^2 \mathcal{E}^{eq} \delta\epsilon}{2T} \delta\Lambda, \quad \mathcal{W}_\epsilon^{(2)} \to \frac{\pi\Omega}{\gamma_{c,eq}} \frac{\delta N_{eq}^2 \delta\epsilon^2}{T}. \qquad (58)$$

As a consequence, unlike for a Carnot cycle, the cooling power is nonzero and the coefficient of performance η is finite when the temperature difference vanishes

$$\eta \approx \left| \frac{\mathcal{Q}_R^{(0)} + \mathcal{Q}_R^{(1)}}{\mathcal{W}_\epsilon^{(1)} + \mathcal{W}_\epsilon^{(2)}} \right| \xrightarrow{\delta T \to 0} |\sin(\phi)| \frac{\gamma_{c,eq} |\mathcal{E}^{eq}| \delta\Lambda}{2\Omega\delta\epsilon} \qquad (59)$$

---

[11]If the bias voltage were finite, there would be an additional chemical work contribution.

[12]Beyond the weak-coupling regime, higher orders in the tunnel coupling induce a renormalization of the dot's population [3], which can then be related to a finite work cost. See also Ref. [109] for an expression of the work in the strong-coupling regime for a noninteracting fermionic system.

for the desired sign of $\mathcal{Q}_R$ ($\mathcal{Q}_R > 0$ for refrigeration and $\mathcal{Q}_R < 0$ for the heat pump) and $\eta = 0$ otherwise. However, in the limit of infinitely slow driving $\Omega \rightarrow 0$, namely, a perfectly quasistatic cycle, η becomes infinite like the Carnot efficiency. Equations (58) and (59) are crucial analytical results in the following more detailed discussion of the dot acting as a refrigerator or heat pump: Depending only on the driving amplitudes and well-known equilibrium quantities, i.e., charge fluctuations δN_{eq}^2, Seebeck energy $\mathcal{E}^{eq}$, and the *RC* time scaled by the driving frequency $\gamma_{c,eq}/\Omega$, Eqs. (58) and (59) provide simple estimates of the device performance as a function of the system parameters.

C. Refrigerator and heat pump performance

To analyze the refrigeration and heat pump performance, we focus mostly on the interesting operating points for the thermal machine at $V_b = 0$ identified in Sec. IV: mechanism A (resonance points) for a repulsive on-site interaction and mechanism C (particle-hole symmetric point) for an attractive on-site interaction. The thermodynamic quantities relevant to the device performance for these parameters are plotted in Fig. 5 as a function of $\bar{\epsilon}$ and δT, allowing us to compare the two cases $U > 0$ and $U < 0$. All displayed curves were obtained by numerically solving the master equation $\partial_t |\rho) = W |\rho)$ (see Sec. II C) and therefore take into account all the orders in Ω/Γ (see Appendix J for a comparison with the adiabatic-response limit). Note that we have always set the interaction strength to $|U|/T = 10$. The latter is slightly smaller than in Sec. IV, in order to avoid that corrections at higher orders in Ω/Γ become dominant (discussed below).

Let us start by discussing the influence of the driving protocol itself, through the phase ϕ, the amplitudes $\delta\epsilon$ and $\delta\Lambda$, and the frequency Ω. Equations (58) and (59) clearly state that ϕ has no influence on the $\mathcal{W}_\epsilon^{(2)}$ but maximizes the heat, and hence the performance η for $\phi = \pi/2$. We therefore set $\phi = \pi/2$ for the entirety of this analysis, including Figs. 5 and 6. The key point for the amplitude dependence is that up to the leading order in Ω, the coupling asymmetry $\delta\Lambda$ only affects the heat $\mathcal{Q}_R^{(1)} \sim \delta\epsilon\delta\Lambda$, but not the work $\mathcal{W}_\epsilon^{(2)} \sim \delta\epsilon^2$, since it is irrelevant to which contact the energy corresponding to this work flows. As a result, the performance $\eta \sim \delta\Lambda/\delta\epsilon$ improves with larger asymmetry $\delta\Lambda$ increasing the directionality of the heat flow, but still degrades with larger $\delta\epsilon$ increasing the work done on the system to induce this heat flow. Finally, the driving frequency Ω only enters $\mathcal{W}_\epsilon^{(2)}$ in leading order; it provides a typical timescale for the delayed system response and the resulting work due to the driving, as further detailed below.

The dependence of $\mathcal{Q}_R$, $\mathcal{W}_\epsilon^{(2)}$, and η on the working-point dot level $\bar{\epsilon}$ is shown in Figs. 5(a)–5(d). For repulsive interaction $U > 0$, the proportionality $\mathcal{Q}_R, \eta \sim \mathcal{E}^{eq}$ predicted by Eq. (58) and (59) implies the same well-known [69,70,111] sawtooth behavior as a function of $\bar{\epsilon}$ as for the Seebeck coefficient $\mathcal{E}^{eq}$. Indeed, the numerical results in Figs. 5(a) and 5(c) confirm that apart from small $|\delta T|$ corrections, the sign changes of $\mathcal{E}^{eq}$ near the resonances $\bar{\epsilon} = 0, -U$ and near the particle-hole symmetry point $\bar{\epsilon} = -U/2$ result in suppressed $\mathcal{Q}_R$ and η, concomitant with switches from refrigeration (blue curve) to heat pumping (red curve) behavior. The slope of $\mathcal{Q}_R$

as a function of $\bar{\epsilon}$ is however attenuated around $\bar{\epsilon} = -U/2$ compared to the slopes around $\bar{\epsilon} = 0, -U$. This is because $\mathcal{Q}_R$ is, unlike η, also proportional to the charge fluctuations δN_{eq}^2, which are generally stronger near the single-particle resonances $\bar{\epsilon} = 0, -U$. These fluctuations cancel out in η because the work $\mathcal{W}_\epsilon^{(2)}$ as given in Eq. (58) is likewise proportional to δN_{eq}^2. The latter is due to the fact that net work can only be done per ϵ-driving cycle if a crossing of a single-particle resonance allows at least for temporary dot occupation changes.

For attractive interaction $U < 0$ [Figs. 5(b) and 5(d)], the Seebeck energy $\mathcal{E}^{eq}$ and hence $\mathcal{Q}_R$ only change sign once close to $\bar{\epsilon} = -U/2 = +|U|/2$, which is the pairing-related two-particle resonance [78]. This means that in contrast to the case $U > 0$, the system only switches once from a heat pump to a refrigerator at small $\delta T/T \ll 1$ when sweeping through $\bar{\epsilon} = -U/2$, with $\mathcal{Q}_R < 0 \rightarrow \mathcal{Q}_R > 0$ [Fig. 5(b)]. The second key difference from the repulsive interaction visible in Fig. 5(d) is that η is generally suppressed for dot levels $0 < \bar{\epsilon} < -U$. This stems from the proportionality to the charge rate $\eta \sim \gamma_c$, as predicted by Eq. (59). This rate enters the coefficient of performance via the work (58), for which the dominant second-order correction is in fact inversely proportional to the equilibrium charge rate $\mathcal{W}_\epsilon^{(2)} \sim \Omega/\gamma_{c,eq}$ due to the delayed system response. According to Eq. (51), $\mathcal{W}_\epsilon^{(2)}$ depends on the first-order correction to the dot state $\rho^{(1)}$, representing the delay of the state evolution due to the external driving. The slower the system response, the larger the delay, as generally stated by Eq. (16) and as quantified by γ_c/Ω specifically for the charge-mode response. For attractive interaction and $0 < \bar{\epsilon} < -U$, the rate γ_c is exponentially suppressed. The resulting suppression of changes in the dot occupation during the ϵ drive thus increases the required work significantly and hence suppresses the performance η. Figure 5 indeed shows $\mathcal{W}_\epsilon^{(2)}$ for $U < 0$ to be approximately two orders of magnitude larger compared to the repulsive dot with $U > 0$ when comparing the points of operation indicated by the red and blue stars. Moreover, the smaller rate γ_c for $U < 0$ also requires a lower driving frequency compared to the repulsive dot in order to remain in the adiabatic-response regime (see Appendix J). The issue can be mitigated by operating at higher base temperature T, thus motivating our choice of $|U| = 10T$ instead of $30T$ as in Sec. IV.

Irrespective of the interaction sign, Figs. 5(a)–5(d) reveal an approximate symmetry between the refrigerator and heat pump case under a temperature inversion $\delta T \rightarrow -\delta T$ together with a particle-hole parameter transform $\mathcal{T}$ (see Sec. III B 3). This is because the work $\mathcal{W}_\epsilon^{(2)}$ is symmetric under both $\mathcal{T}$ and $\delta T \rightarrow -\delta T$ [Eq. (57)], the pumped heat $\mathcal{Q}_R^{(1)} \sim \mathbf{B}_{HR}(\mathbf{R})$ is antisymmetric under $\mathcal{T}$ but symmetric under δT inversion [Eq. (52)], and the steady-state heat $\mathcal{Q}_R^{(0)} \sim \delta T$ is instead symmetric under $\mathcal{T}$ but antisymmetric under $\delta T \rightarrow -\delta T$ (see also Appendix I). For an identical driving frequency $\Omega = 10^{-2}\Gamma$, this symmetry between the refrigerator and heat pump is less accurate for $U < 0$ than for $U > 0$, which comes from higher-order contributions and confirms that the dot with an attractive on-site interaction is less in the adiabatic-response regime. This can be seen by looking at $\mathcal{Q}_R$ (solid lines) in Figs. 5(a) and 5(b): For $U > 0$, rotating the blue curve (refrigerator) by $180°$ around $(-U/2, 0)$ perfectly gives the red curve (heat
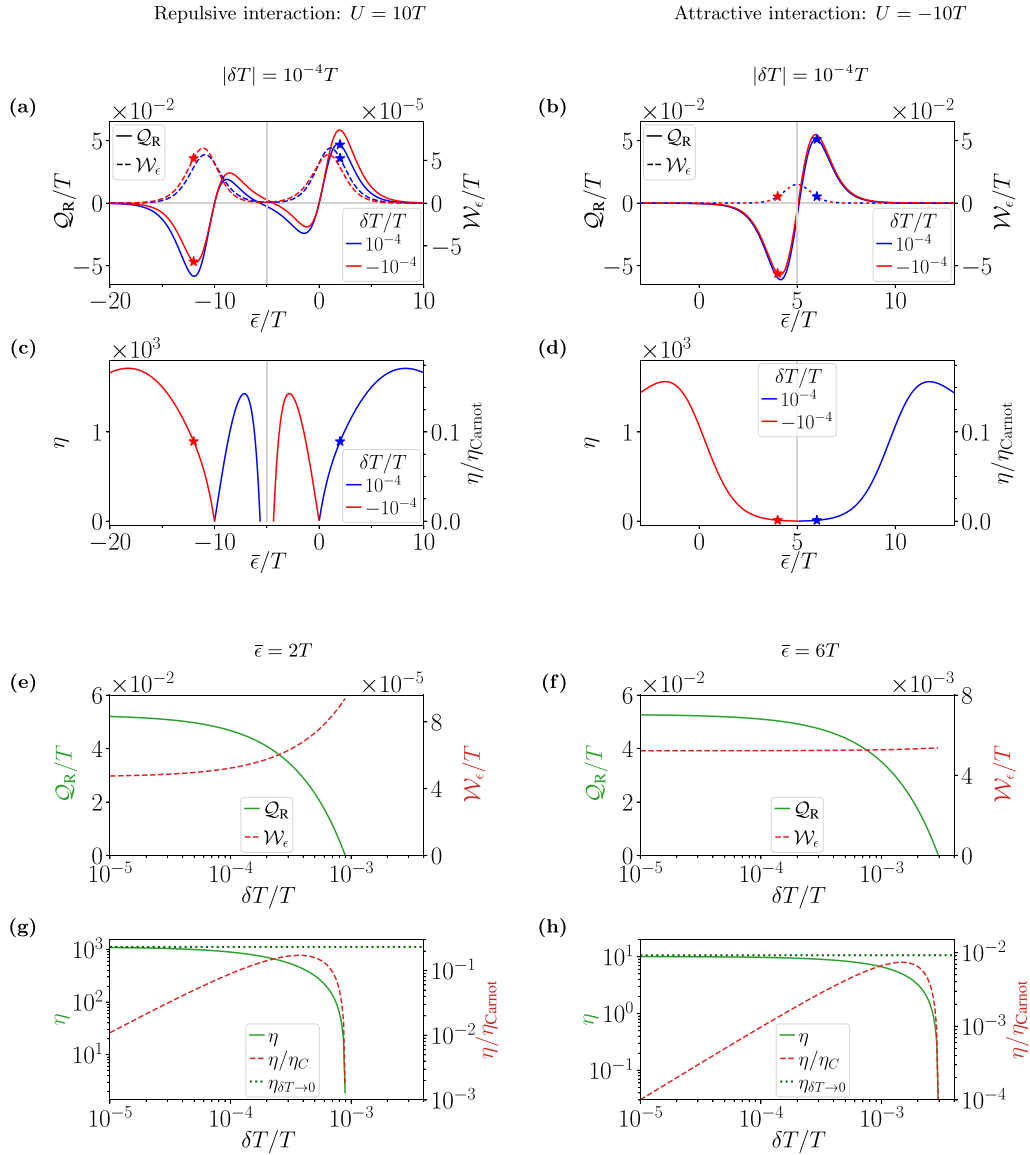
FIG. 5. Thermodynamic quantities as functions of the (a)–(d) energy $\bar{\epsilon}$ and (e) and (f) temperature difference $\delta T = T_{\mathrm{L}} - T$ for a repulsive on-site interaction (left column) and an attractive one (right column), obtained by numerically integrating the full master equation. In (a)–(d) we compare the refrigerator ($\delta T > 0$, blue curves) and heat pump ($\delta T < 0$, red curves) operating modes: (a) and (b) heat $\mathcal{Q}_{\mathrm{R}}$ (solid lines, left axis) and work $\mathcal{W}_\epsilon$ (dashed lines, right axis) and (c) and (d) coefficient of performance η, with the right axis indicating the ratio between η and the Carnot efficiency. In (e) and (f) we only consider the refrigerator ($\delta T > 0$), with the blue stars in (a)–(d) indicating the chosen $\bar{\epsilon}$ values and the red stars in (a)–(d) showing the corresponding values if one used the heat pump operating mode instead. The coefficient η is plotted only for the values of $\bar{\epsilon}$ for which $\mathcal{Q}_{\mathrm{R}}$ has the desired sign. In (g) and (h) the green dotted line indicates the efficiency $\eta_{\delta T \to 0}$ in the limit of small driving amplitudes for a vanishing temperature difference [Eq. (59)]. The parameters are $\Gamma = 10^{-2}T$, $\Omega = 10^{-2}\Gamma$, $\delta\epsilon = 10^{-1}T$, $\delta\Lambda = 1$, $\phi = \pi/2$, $|U| = 10T$, $\bar{V}_{\mathrm{b}} = 0$, and $\bar{\Lambda} = 0$.

pump), while this is not the case for $U < 0$; in particular, the blue star is exactly on the peak whereas the red one is slightly on the side of the dip.

Nevertheless, the mapping between refrigeration and heat pumping holds well enough so that we can, from now on, focus exclusively on refrigeration to assess which temperature differences δT allow for a dot operation with reasonable performance η. First, we compare the δT dependences of heat, work, and performance coefficient for repulsive interaction [Figs. 5(e) and 5(g)] to the ones for attractive interaction [Figs. 5(f) and 5(h)]. This mainly reveals that at the individ-

ually chosen working points $\bar{\epsilon}$ [blue stars in Figs. 5(a)–5(d)], the attractive system has a considerably larger operation range for $\delta T/T$. This is because the above-mentioned suppression of the charge rate γ_{c} for $U < 0$ also suppresses the stationary particle current $I_{N\mathrm{R}}^{(0)} \sim \gamma_{\mathrm{c,eq}}$ [Eq. (54)]. The detrimental zeroth-order steady-state heat contribution $\mathcal{Q}_{\mathrm{R}}^{(0)} \sim I_{N\mathrm{R}}^{(0)} \sim \gamma_{\mathrm{c,eq}}$ [Eq. (52)] is therefore significantly smaller than the geometrically pumped heat $\mathcal{Q}_{\mathrm{R}}^{(1)}$, even for sizable temperature differences δT. Finite interaction $|U| > 0$, however, always has a detrimental effect on the cooling power due to the leakage heat current, that is, the $-\kappa\delta T$ term in Eq. (52), since
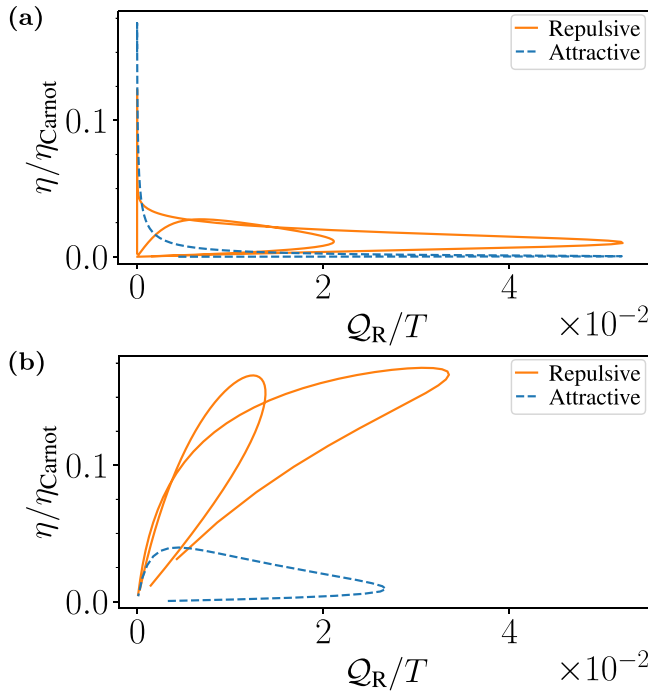
(a)

(b)

FIG. 6. Coefficient of performance η and heat $\mathcal{Q}_R$ parametrically plotted as a function of a varied working point $\bar{\epsilon}$, for both $U > 0$ (orange solid lines) and $U < 0$ (blue dashed lines). The curves were obtained by numerically integrating the full master equation. In (a) we set $\delta T = 10^{-5}T$ in the repulsive case and $\delta T = 4 \times 10^{-5}T$ for the attractive dot. In (b) we choose δT such that $\eta/\eta_{\text{Carnot}}$ is maximized in Figs. 5(g) and 5(h), meaning $\delta T = 3.75 \times 10^{-4}T$ and $1.5 \times 10^{-3}T$ for $U > 0$ and $U < 0$, respectively. The factor 4 between δT for the attractive vs the repulsive case accounts for the increased operation range of $\delta T/T$ observed in Figs. 5(f) and 5(h) compared to Figs. 5(e) and 5(g). The parameters not indicated are set as in Fig. 5.

the Fourier heat κ is proportional to U^2 [Eq. (53)].[13] We also note that the compact analytical expression (59) [dotted green lines in Figs. 5(g) and 5(h)] accurately gives the efficiency in the limit of vanishing δT, even for $U < 0$, though it was derived in the adiabatic-response regime and in the limit of small driving amplitudes. This therefore confirms that the device performance can be easily assessed from the system parameters.

Next we find a δT-dependent trade-off between performance η and cooling power $\sim \mathcal{Q}_R \Omega$. This is highlighted in Fig. 6, where both η and $\mathcal{Q}_R$ are plotted parametrically as a function of the working point $\bar{\epsilon}$. For very small $\delta T/T$, the maximum performance η is achieved at zero power, whereas maximum power is reached at very small $\eta/\eta_{\text{Carnot}}$ [Fig. 6(a)]. Conversely, for $\delta T/T$ maximizing $\eta/\eta_{\text{Carnot}}$ at the operating point $\bar{\epsilon}$ indicated by the blue stars in Figs. 5(a)–5(d), this trade-off is much less pronounced for $U < 0$ and almost vanishes for $U > 0$. Maximum power in this case almost coin-

cides with the maximal coefficient of performance [Fig. 6(b)]. Also note that sweeping $\bar{\epsilon}$ for $U > 0$ always yields two separate $(\mathcal{Q}_R, \eta)$ curves, corresponding to the two disconnected $\bar{\epsilon}$ ranges allowing for refrigeration as shown in Figs. 5(a) and 5(c); for $U < 0$, the single requirement $\bar{\epsilon} < -U/2$ [Figs. 5(b) and 5(d)] analogously yields only one connected $(\mathcal{Q}_R, \eta)$ curve.

We finally emphasize that, despite the finite driving speed, we find the system to operate at finite power with more than 15% of the Carnot efficiency. Furthermore, for $U > 0$ and temperature differences $\delta T/T \sim 10^{-3}$, the device can even be operated at maximum power while keeping an η close to the achievable maximum. This is particularly unexpected as single quantum dots are typically disregarded in favor of double-dot devices that allow for a better decoupling from the baths [41]. Quantum dots with a repulsive interaction $U \approx 5$ meV, like in Ref. [94], or an attractive interaction $U \approx -0.2$ meV, like in Ref. [75], would make it possible to pump heat against a tiny but finite temperature difference δT of the order of millikelvin. Devices with larger on-site interaction strengths would allow operating at higher δT.

VI. CONCLUSION

We have analyzed geometric energy transport through strongly interacting, weakly coupled quantum dots due to the slow driving of a pair of system parameters. Based on a master-equation analysis combined with a fermionic duality relation, we have provided compact and intuitive analytical results linking the pumped energy to the well-known steady-state thermoelectric properties of the dot.

We have explicitly worked out that energy pumping, in contrast to charge pumping, is the result of two different decay modes of the dot being excited due to the time-dependent driving: the charge mode, typically contributing via a tight-coupling term proportional to the charge current via the well-known stationary Seebeck coefficient, and the parity mode, uniquely due to the on-site Coulomb interaction. Even though the energy current is more directly susceptible to the Coulomb energy, slow adiabatic energy pumping is typically still governed by the charge mode, even for strong local interaction. The parity mode, however, does become important if the external bias exceeds the Coulomb energy and then, as a result of fermionic duality, yields a contribution symmetric in the interaction sign, i.e., with respect to repulsive and attractive interactions.

Using the obtained analytical results, we have identified the symmetries of the pumped energy with respect to the different (time-averaged) system parameters and we have analyzed in detail all possible pumping schemes and pumping mechanisms. In particular, we have found a number of pumping mechanisms unique to either attractive or repulsive interaction and pumping mechanisms that are not possible for charge pumping, but only for energy pumping. The latter emerge whenever only one or even none of the quantum-dot energy levels are in resonance with the contact chemical potentials.

We have furthermore demonstrated the time-dependently-driven quantum dot to be operable as a heat pump or refrigerator between biased contacts. We have derived a simple yet insightful analytical expression for the efficiency in the

---

[13]Otherwise, the performances of the noninteracting case $U = 0$ are in between the repulsive and attractive cases, e.g., for the efficiency or the maximum δT at which the refrigerator can be operated.

limit of vanishing temperature, linking the driving characteristics to the well-known linear-response Seebeck coefficient, the equilibrium charge fluctuations, and the dot's RC time. This reveals in particular how the performance is decisively affected by the sign of the on-site interaction, in terms of limiting driving speed, output power, and efficiency.

A perspective of high interest for the field of stochastic and quantum (thermo)dynamics would be to extend this study to the statistics of energy pumping [66,68]. This would yield generalized fluctuation relations for this type of interacting, fermionic, cyclic machines.

ACKNOWLEDGMENTS

APPENDIX A: TIME-DEPENDENT ELECTROCHEMICAL POTENTIALS AND TEMPERATURES

Adiabatic pumping due to the driving of the reservoir potentials μ_α and temperatures T_α was previously studied in Refs. [50,59,60]. These quantities are however macroscopic observables characterizing the (local and time-local) equilibrium density operators of the leads $\rho_\alpha = \rho_{\rm eq}(\mu_\alpha, T_\alpha)$ and do not directly enter their Hamiltonian H_α. Hence, including the effect of lead potential and temperature driving on the state of a tunnel-coupled quantum dot requires extra care.

More specifically, the master-equation approach employed here, as detailed in Sec. II C, is based on the Born-Markov approximation. This implies that the only dynamics induced in the leads are due to the weakly coupled dot, causing only a negligible deviation from local equilibrium. The resulting dot dynamics after tracing out the leads then only depends on the lead potentials $\mu_\alpha(t_0)$ and temperatures $T_\alpha(t_0)$ at some initial time t_0 at which the dot and lead state can be assumed fully uncorrelated, $\hat{\rho}_{\rm tot}(t_0) = \hat{\rho}(t_0) \prod_\alpha \hat{\rho}_\alpha(t_0)$. However, time-dependent lead potentials and temperatures in practice typically mean that lead state is also manipulated by a combination of external fields and, crucially, coupling to thermal superbaths exchanging particles and heat. A rigorous treatment would therefore consider the combined dot-lead system as an open subsystem and trace out the external superbaths which are kept at constant temperatures and potentials. Since this seems neither analytically nor numerically feasible, we capture here the lead-superbath interaction in a simplified fashion.

On timescales much larger than the thermalization time in the leads, time-dependent $\mu_\alpha(t)$ and $T_\alpha(t)$ can often be mimicked by instead shifting and scaling the single-particle

lead spectra [95–97]

$$\hat{H}_\alpha \to H_\alpha(t) = c_\alpha(t)\hat{H}_\alpha^0 + v_\alpha(t)\hat{N}_\alpha, \tag{A1}$$

with $c_\alpha(t_0) = 1$ as well as $v_\alpha(t_0) = 0$ and where $\hat{H}_\alpha^0$ denotes the lead Hamiltonian from Eq. (2). The corresponding Born-Markov master equation of the weakly coupled dot in the slow-driving regime then becomes equal to the master equation for constant lead parameters, except for the parameter replacement

$$T_\alpha \to T_\alpha(t) = c_\alpha(t)\bar{T}_\alpha, \tag{A2a}$$

$$\mu_\alpha \to \mu_\alpha(t) = c_\alpha(t)\bar{\mu}_\alpha + v_\alpha(t). \tag{A2b}$$

This paper employs this replacement scheme, since it can in fact be physically determined for the weakly coupled Markovian leads subject to slow driving relevant here. The key point for this is the large timescale separation between the lead thermalization time $t_{\rm therm}$ and both driving period as well as typical tunneling time: $t_{\rm therm}\Omega \ll t_{\rm therm}\Gamma \ll 1$. Namely, we may assume that instances of superbath-lead interactions take place at separate times t_i. With this, we "slice" the full driving period into time intervals $[t_i, t_{i+1}]$ for which we assume $\Gamma t_{\rm therm} \ll 1 \ll \Gamma\Delta t = \Gamma(t_{i+1} - t_i) \ll \Gamma/\Omega$. During each interval, we can approximate temperatures and potentials as constant, $T_\alpha(t) = T_\alpha(t_i)$ and $\mu_\alpha(t) = \mu_\alpha(t_i)$, while the external superbaths effectively decouple from the leads. Due to the very fast lead rethermalization, the superbath-lead interaction should result in small yet quick changes of temperatures $T_\alpha(t_i) \to T_\alpha(t_{i+1}) = T_\alpha(t_i) + \delta T_{\alpha,i}$ and potentials $\mu_\alpha(t_i) \to \mu_\alpha(t_{i+1}) = \mu_\alpha(t_i) + \delta\mu_{\alpha,i}$ and should furthermore suppress any residual dot-lead correlation that may have built up during the interval $[t_i, t_{i+1}]$. Since $\Gamma\Delta t \gg 1$ while $\Omega/\Gamma \ll 1$, this means that each time interval can be treated separately using the Born-Markov master equation as in Sec. II C: Dot and leads are uncorrelated at time t_i, the initial dot state is given either by the prepared initial state $\rho(t_i = 0) = \rho_0$ or by the solution to the master equation in the previous interval $\rho(t_i) = \rho(t_{i-1} + \Delta t)$, and the lead states at time t_i are characterized by local equilibrium states with respect to $\mu_\alpha(t_i)$ and $T_\alpha(t_i)$. Stitching all time intervals together and using $\Omega\Delta t \ll 1$, we find that on the timescale of the long driving period, the dot dynamics $\rho(t)$ obeys the single Born-Markov master equation (7) with the continuous parametric time dependence (A2).

Interestingly, while this paper studies the driving effect on particle current $I_{N\alpha}$ and electronic energy current $I_{H\alpha}$, as defined in Eq. (19), the above time-sliced picture also suggests a generalization to heat currents: For a weakly-tunnel-coupled dot and Markovian leads remaining approximately in local equilibrium at potential μ_α, the stationary heat current $I_{Q\alpha}$ is well approximated by the excess energy current with respect to the chemical potential: $I_{Q\alpha} = I_{H\alpha} - \mu_\alpha I_{N\alpha}$. The lead states within each time slice $[t_i, t_{i+1}]$ can also be approximated by such local equilibrium states when setting the proper time-dependent lead parameters $\mu_\alpha = \mu_\alpha(t_i)$ and $T_\alpha = T_\alpha(t_i)$. Hence, on the timescale of the driving, the heat current generalizes to $I_{Q\alpha}(t) = I_{H\alpha}(t) - \mu_\alpha(t)I_{N\alpha}(t)$. This is the reasoning behind our claim from Sec. V that for a time-independent $\mu_\alpha = 0$, the heat current is equal to the energy current.

APPENDIX B: ANALYTICAL EXPRESSIONS FOR DUALITY QUANTITIES

We first provide the fermionic duality relation for the kernel W of the dissipative evolution due to Markovian, weakly-tunnel-coupled baths in the wideband limit. For the spin-degenerate dot, this duality reads [76,79]

$$W + \mathcal{P}[W^{\mathrm{i}}]^{\dagger}\mathcal{P} = -2\Gamma\mathcal{I}, \tag{B1}$$

where W^{i} is the kernel corresponding to the dual model, $\Gamma = \Gamma_{\mathrm{L}} + \Gamma_{\mathrm{R}}$ is the above-defined lead-summed coupling strength per spin, the bold $\dagger$ indicates Hermitian conjugation in Liouville space with respect to the Hilbert Schmidt scalar product, $\mathcal{P}\bullet = (-\mathbb{1})^N \bullet = \mathcal{P}^{\dagger}\bullet$ is the Liouville-Hermitian superoperator of applying the fermion-parity operator $(-\mathbb{1})^N$ from the left to some operator $\bullet$, and $\mathcal{I}$ is the Liouville space identity. We furthermore introduce the duality parameter transform

$$\mathcal{D} : (\epsilon, U, V_{\mathrm{b}}, T_{\alpha}, \Lambda) \to (-\epsilon, -U, -V_{\mathrm{b}}, T_{\alpha}, \Lambda) \tag{B2}$$

to write $W^{\mathrm{i}}\bullet = \mathcal{D}W\mathcal{D}\bullet$. The Liouville-space trace relation $\mathrm{Tr}W = -\Gamma\mathrm{Tr}\mathcal{I}$ then enables us, in analogy to how, e.g., Ref. [112] treats open-system symmetries, to formulate Eq. (B1) as an anti-Hermiticity relation

$$[\mathcal{P}\mathcal{D}\tilde{W}]^{\dagger} = -\mathcal{P}\mathcal{D}\tilde{W} \tag{B3}$$

for the traceless part of the kernel $\tilde{W} = W + \Gamma\mathcal{I}$ with respect to a Hilbert-Schmidt product with modified left (dual) vectors $(x| \to (x|\mathcal{P}\mathcal{D}$. This links right/left eigenvectors of the inverted kernel W^{i} to left/right eigenvectors of the original W. Namely, starting from the expressions in Sec. II C, the right eigenvectors of W^{i} are

$$|z^{\mathrm{i}}) = \frac{1}{\Gamma\gamma_{\mathrm{c}}^{\mathrm{i}}}[f_{\epsilon}^{+} f_{U}^{+}|0) + f_{\epsilon}^{-} f_{U}^{+}|1) + f_{\epsilon}^{-} f_{U}^{-}|2)],$$

$$|p^{\mathrm{i}}) = |p), \quad |c^{\mathrm{i}}) = \frac{1}{2}(-\hat{\mathbb{1}})^{\hat{N}}[|N) - N_z|\mathbb{1})] \tag{B4}$$

and the left ones read

$$((z^{\mathrm{i}})'| = (\mathbb{1}|, \quad ((p^{\mathrm{i}})'| = ((-\mathbb{1})^N z|,$$

$$((c^{\mathrm{i}})'| = (N| - N_z(\mathbb{1}|, \tag{B5}$$

with the charge relaxation rate $\gamma_{\mathrm{c}}^{\mathrm{i}} = f_{\epsilon}^{-} + f_{U}^{+}$. The expectation value of the quantum-dot occupation and parity in the stationary state are given by

$$N_z = (N|z) = \frac{2f_{\epsilon}^{+}}{f_{\epsilon}^{+} + f_{U}^{-}},$$

$$p_z = ((-\mathbb{1})^N|z) = \frac{f_{\epsilon}^{-} f_{U}^{-} + f_{\epsilon}^{+} f_{U}^{+} - 2f_{\epsilon}^{+} f_{U}^{-}}{\Gamma(f_{\epsilon}^{+} + f_{U}^{-})} \tag{B6}$$

for the original model and

$$N_z^{\mathrm{i}} = (N|z^{\mathrm{i}}) = \frac{2f_{\epsilon}^{-}}{f_{\epsilon}^{-} + f_{U}^{+}},$$

$$p_z^{\mathrm{i}} = ((-\mathbb{1})^N|z^{\mathrm{i}}) = \frac{f_{\epsilon}^{-} f_{U}^{-} + f_{\epsilon}^{+} f_{U}^{+} - 2f_{\epsilon}^{-} f_{U}^{+}}{\Gamma(f_{\epsilon}^{-} + f_{U}^{+})} \tag{B7}$$

for the dual one.

APPENDIX C: PROOF OF THE SYMMETRIES

This Appendix proves the particle-hole-transform-related symmetries of the pumping curvatures $\mathbf{B}_{H\alpha}^{\mathrm{P/C}}(\mathbf{R})$ discussed in Sec. III B 3 and the duality-related symmetry of the parity component $\mathbf{B}_{H\alpha}^{\mathrm{P}}(\mathbf{R})$ under inversion of the interaction $U \to -U$ identified in Sec. IV B.

1. Particle-hole transform

To prove the symmetries under the particle-hole parameter transform

$$\mathcal{T} : (\epsilon, U, V_{\mathrm{b}}, T_{\alpha}, \Lambda) \to (-\epsilon - U, U, -V_{\mathrm{b}}, T_{\alpha}, \Lambda), \tag{C1}$$

we first need expressions for its action on the rates and eigenvectors of the master-equation kernel W given in Sec. II C.[14] The explicit expressions of the stationary state $|z)$ in Eq. (13) and of its dual $|z^{\mathrm{i}})$ in Eq. (B4) make it straightforward to verify

$$\mathcal{T}|z) = \mathcal{P}_{\mathcal{H}}|z), \quad \mathcal{T}|z^{\mathrm{i}}) = \mathcal{P}_{\mathcal{H}}|z^{\mathrm{i}}) \tag{C2}$$

with the super-Hermitian and unitary particle-hole-transform superoperator $\mathcal{P}_{\mathcal{H}} = \mathcal{P}_{\mathcal{H}}^{\dagger} = \mathcal{P}_{\mathcal{H}}^{-1}$ acting on the three spin-symmetric dot basis states $|0) = |0\rangle\langle 0|$, $|1) = \frac{1}{2}\sum_{i=\uparrow,\downarrow}|i\rangle\langle i|$, and $|2) = |2\rangle\langle 2|$ as

$$\mathcal{P}_{\mathcal{H}}|0) = |2), \quad \mathcal{P}_{\mathcal{H}}|2) = |0), \quad \mathcal{P}_{\mathcal{H}}|1) = |1). \tag{C3}$$

Relations analogous to Eq. (C2) also hold for the (α) lead-resolved states

$$\mathcal{T}|z_{\alpha}) = \mathcal{P}_{\mathcal{H}}|z_{\alpha}), \quad \mathcal{T}|z_{\alpha}^{\mathrm{i}}) = \mathcal{P}_{\mathcal{H}}|z_{\alpha}^{\mathrm{i}}). \tag{C4}$$

Furthermore, the explicit expressions for the charge and parity rate γ_{c} and γ_{p} given in Sec. II C, as well as their lead-resolved counterparts $\gamma_{\mathrm{c}\alpha}$ and $\gamma_{\mathrm{p}\alpha}$, can be used to show that these rates are $\mathcal{T}$ symmetric,

$$\mathcal{T}\gamma_{\mathrm{c/p}} = \gamma_{\mathrm{c/p}}, \quad \mathcal{T}\gamma_{\mathrm{c/p}\alpha} = \gamma_{\mathrm{c/p}\alpha}. \tag{C5}$$

Equation (C2) and $(N|\mathcal{P}_{\mathcal{H}} = 2(\mathbb{1}| - (N|$ imply that $\mathcal{T}$ acts also as particle-hole transform of the dot occupation number $\mathcal{T}N_z = (N|\mathcal{T}|z) = (N|\mathcal{P}_{\mathcal{H}}|z) = 2 - N_z$. Summarized with analogous relations for the lead-resolved charges and all duals, we find

$$\mathcal{T}N_z = 2 - N_z, \quad \mathcal{T}N_{z\alpha} = 2 - N_{z\alpha},$$

$$\mathcal{T}N_z^{\mathrm{i}} = 2 - N_z^{\mathrm{i}}, \quad \mathcal{T}N_{z\alpha}^{\mathrm{i}} = 2 - N_{z\alpha}^{\mathrm{i}}. \tag{C6}$$

Equations (C2) and (C6) together with the eigenvector expressions from Sec. II C and the $\mathcal{T}$ invariance of parameter-independent operators yield the $\mathcal{T}$ action on all left and right eigenvectors of the kernels W and W^{α},

$$\mathcal{T}|z) = \mathcal{P}_{\mathcal{H}}|z), \quad \mathcal{T}(\mathbb{1}| = (\mathbb{1}| = (\mathbb{1}|\mathcal{P}_{\mathcal{H}},$$

$$\mathcal{T}|c) = -\mathcal{P}_{\mathcal{H}}|c), \quad \mathcal{T}(c'| = -(c'|\mathcal{P}_{\mathcal{H}},$$

$$\mathcal{T}|p) = |p) = \mathcal{P}_{\mathcal{H}}|p), \quad \mathcal{T}(p'| = (p'|\mathcal{P}_{\mathcal{H}}, \tag{C7}$$

---

[14] A complete transform would also act on the initially prepared dot state. Since $\mathcal{T}$ has no effect on this initial dot state, our analysis is only valid once all transient dynamics have decayed, which we however assume throughout the paper.

and equivalently for the (α) lead-resolved versions, where we have used that the unit operator $\mathbb{1}$ and the fermion parity $(-\mathbb{1})^N$ are invariant under the particle-hole transform $\mathcal{P}_{\mathcal{H}}$. The rate symmetries (C5) and the eigenvector relations (C7) combine with the key symmetry relations

$$\mathcal{T}W = \mathcal{P}_{\mathcal{H}} W \mathcal{P}_{\mathcal{H}}, \quad \mathcal{T}W^{\alpha} = \mathcal{P}_{\mathcal{H}} W^{\alpha} \mathcal{P}_{\mathcal{H}},$$

$$\mathcal{T}\frac{1}{\tilde{W}} = \mathcal{P}_{\mathcal{H}} \frac{1}{\tilde{W}} \mathcal{P}_{\mathcal{H}}, \quad \mathcal{T}\frac{1}{\tilde{W}^{\alpha}} = \mathcal{P}_{\mathcal{H}} \frac{1}{\tilde{W}^{\alpha}} \mathcal{P}_{\mathcal{H}}. \quad \text{(C8)}$$

Together with Eq. (C2), this rigorously proves our statement from Sec. III B 3 that $\mathcal{T}$ effectively implements a particle-hole transform of the entire system evolution and its steady state. Apart from these kernel relations (C8), the only remaining ingredient required for our proof is the commutation relation of $\mathcal{T}$ and the parameter gradient $\nabla_{\mathbf{R}} = (\partial_{\epsilon}, \partial_{U}, \partial_{V_b}, \partial_{T_{\alpha}}, \partial_{\Lambda})^{\mathsf{T}}$. By the very definition of $\mathcal{T}$ in Eq. (C1), we have

$$\mathcal{T}\nabla_{\mathbf{R}} = \tilde{\sigma}\nabla_{\mathbf{R}}\mathcal{T}, \quad \tilde{\sigma} = \begin{pmatrix} -1 & 0 & 0 & 0_{1\times 2} \\ -1 & 1 & 0 & 0_{1\times 2} \\ 0 & 0 & -1 & 0_{1\times 2} \\ 0_{2\times 1} & 0_{2\times 1} & 0_{2\times 1} & 1_{2\times 2} \end{pmatrix}. \quad \text{(C9)}$$

The diagonal elements of $\tilde{\sigma}$ correspond to the signs introduced by $\mathcal{T}$, whereas the single off-diagonal element in the second row stems from the additional U shift of ϵ. Note that with respect to the main text, we introduced here a five-dimensional gradient $\nabla_{\mathbf{R}}$. Whenever considering a concrete driving scheme or calculating curvatures from cross products, the relevant subspace needs to be considered for both $\nabla_{\mathbf{R}}$ and $\tilde{\sigma}$.

The most general form of the particle-hole symmetry relations discussed in Sec. III B 3 now follows straightforwardly from the definition of the lead-resolved geometric connections in Eq. (22) and the corresponding pumping curvatures (23), namely,

$$\mathcal{T}\mathbf{A}_{\mathcal{O}\alpha}(\mathbf{R}) = \tilde{\sigma}(\mathcal{T}\mathcal{O}|[\mathcal{T}W^{\alpha}]\left[\mathcal{T}\frac{1}{\tilde{W}}\right]\nabla_{\mathbf{R}}\mathcal{T}|z)$$

$$= \tilde{\sigma}(\mathcal{T}\mathcal{O}|\mathcal{P}_{\mathcal{H}}W^{\alpha}\mathcal{P}_{\mathcal{H}}\mathcal{P}_{\mathcal{H}}\frac{1}{\tilde{W}}\mathcal{P}_{\mathcal{H}}\mathcal{P}_{\mathcal{H}}\nabla_{\mathbf{R}}|z)$$

$$= \tilde{\sigma}\mathbf{A}_{[\mathcal{P}_{\mathcal{H}}\mathcal{T}\mathcal{O}],\alpha}(\mathbf{R}). \quad \text{(C10)}$$

For the two observables $\hat{\mathcal{O}}$ discussed in this paper, energy $\hat{H}$ and charge $\hat{N}$, we have

$$\mathcal{P}_{\mathcal{H}}\mathcal{T}\hat{H} = \hat{H} - (2\epsilon + U)\mathbb{1}, \quad \mathcal{P}_{\mathcal{H}}\mathcal{T}\hat{N} = 2\times\mathbb{1} - \hat{N}, \quad \text{(C11)}$$

which, when using $(\mathbb{1}|W^{\alpha} = 0$ in Eq. (22), gives

$$\mathcal{T}\mathbf{A}_{H\alpha}(\mathbf{R}) = +\tilde{\sigma}\mathbf{A}_{H\alpha}(\mathbf{R}),$$

$$\mathcal{T}\mathbf{A}_{N\alpha}(\mathbf{R}) = -\tilde{\sigma}\mathbf{A}_{N\alpha}(\mathbf{R}). \quad \text{(C12)}$$

The only difference between energy and charge under action of $\mathcal{T}$ is the relative minus sign. This formally explains why all particle-hole symmetry relations for the energy pumping curvatures are the same as for charge pumping except for an overall sign.

Finally, the concrete form of the symmetry relations for the pumping curvatures readily follows from the definition (23):

$$\mathcal{T}\mathbf{B}_{\mathcal{O}\alpha}(\mathbf{R}) = [\tilde{\sigma}\nabla_{\mathbf{R}}] \times \mathcal{T}\mathbf{A}_{\mathcal{O}\alpha}(\mathbf{R})$$

$$= [\tilde{\sigma}\nabla_{\mathbf{R}}] \times [\tilde{\sigma}\mathbf{A}_{[\mathcal{P}_{\mathcal{H}}\mathcal{T}\mathcal{O}],\alpha}(\mathbf{R})]. \quad \text{(C13)}$$

The (anti)symmetries for $\hat{\mathcal{O}} = \hat{H}$ stated in Sec. III B 3 are simply the respective nonzero components of Eq. (C13) for the individual two-parameter driving schemes. The diagonal elements of $\tilde{\sigma}$ provide the parameter-dependent symmetry signs $\sigma(R_i)$; the special form (41) for U driving arises from the off-diagonal element of $\tilde{\sigma}$ and from the properties of the cross product. To see that Eqs. (C10) and (C13) also hold individually for the charge and parity component, we can simply repeat the steps in Eq. (C10) with the respective projectors $|c)(c'|$ and $|p)(p'|$ inserted precisely to the left of the gradient $\nabla_{\mathbf{R}}$. Since Eq. (C7) separately ensures $\mathcal{T}[|c)(c'|] = \mathcal{P}_{\mathcal{H}}|c)(c'|\mathcal{P}_{\mathcal{H}}$ and $\mathcal{T}[|p)(p'|] = \mathcal{P}_{\mathcal{H}}|p)(p'|\mathcal{P}_{\mathcal{H}}$, the computation proceeds analogously:

$$\mathcal{T}\mathbf{A}_{\mathcal{O}\alpha}^{\mathrm{C/P}}(\mathbf{R}) = \tilde{\sigma}\mathbf{A}_{[\mathcal{P}_{\mathcal{H}}\mathcal{T}\mathcal{O}],\alpha}^{\mathrm{C/P}}(\mathbf{R}),$$

$$\mathcal{T}\mathbf{A}_{H\alpha}^{\mathrm{C/P}}(\mathbf{R}) = +\tilde{\sigma}\mathbf{A}_{H\alpha}^{\mathrm{C/P}}(\mathbf{R}),$$

$$\mathcal{T}\mathbf{A}_{N\alpha}^{\mathrm{C/P}}(\mathbf{R}) = -\tilde{\sigma}\mathbf{A}_{N\alpha}^{\mathrm{C/P}}(\mathbf{R}),$$

$$\mathcal{T}\mathbf{B}_{\mathcal{O}\alpha}^{\mathrm{C/P}}(\mathbf{R}) = [\tilde{\sigma}\nabla_{\mathbf{R}}] \times \left[\tilde{\sigma}\mathbf{A}_{[\mathcal{P}_{\mathcal{H}}\mathcal{T}\mathcal{O}],\alpha}^{\mathrm{C/P}}(\mathbf{R})\right]. \quad \text{(C14)}$$

This completes our proof of the symmetries related to the particle-hole parameter transform $\mathcal{T}$.

2. Interaction-sign symmetric parity component

We can prove the U-symmetric behavior of the paritylike energy pumping curvature $\mathbf{B}_{H\alpha}^{\mathrm{P}}(\mathbf{R})$ highlighted in Sec. IV B by studying the action of the duality parameter transform (B2) on the ingredients of $\mathbf{B}_{H\alpha}^{\mathrm{P}}(\mathbf{R})$. First, it is clear by definition that

$$\mathcal{D}|z) = |z^{\mathrm{i}}), \quad \mathcal{D}|z^{\mathrm{i}}) = |z). \quad \text{(C15)}$$

It is furthermore evident from Eq. (B2) that

$$\mathcal{D}\gamma_{\mathrm{p}} = \gamma_{\mathrm{p}}, \quad \mathcal{D}(-\mathbb{1})^N = (-\mathbb{1})^N, \quad \mathcal{D}U = -U \quad \text{(C16)}$$

and that the commutation relation between $\mathcal{D}$ and the gradient $\nabla_{\mathbf{R}}$ reads

$$\mathcal{D}\nabla_{\mathbf{R}} = \tilde{\sigma}_{\mathcal{D}}\nabla_{\mathbf{R}}\mathcal{D}, \quad \tilde{\sigma}_{\mathcal{D}} = \mathrm{diag}(-1, -1, -1, 1, 1). \quad \text{(C17)}$$

Equations (C15)–(C17) together show that the action of $\mathcal{D}$ on the paritylike excitation $\mathbf{x}^{\mathrm{P}}$ as introduced in the first line of Eq. (25c) is given by

$$\mathcal{D}\mathbf{x}^{\mathrm{P}} = -\frac{1}{\mathcal{D}\gamma_{\mathrm{p}}}(\mathcal{D}z^{\mathrm{i}}(-\mathbb{1})^N|\mathcal{D}\nabla_{\mathbf{R}}|z)$$

$$= -\tilde{\sigma}_{\mathcal{D}}\frac{1}{\gamma_{\mathrm{p}}}(z(-\mathbb{1})^N|\nabla_{\mathbf{R}}|z^{\mathrm{i}}) = -\tilde{\sigma}_{\mathcal{D}}\mathbf{x}^{\mathrm{P}}. \quad \text{(C18)}$$

The last line in Eq. (C18) follows from Eq. (36), with the key difference being the matrix prefactor $\tilde{\sigma}_{\mathcal{D}}$. This factor signifies that when applying the dual transform after taking the gradient $\nabla_{\mathbf{R}}$, $\mathbf{x}^{\mathrm{P}}$ is no longer antisymmetric in all components, but attains an additional sign according to Eq. (C17). This likewise
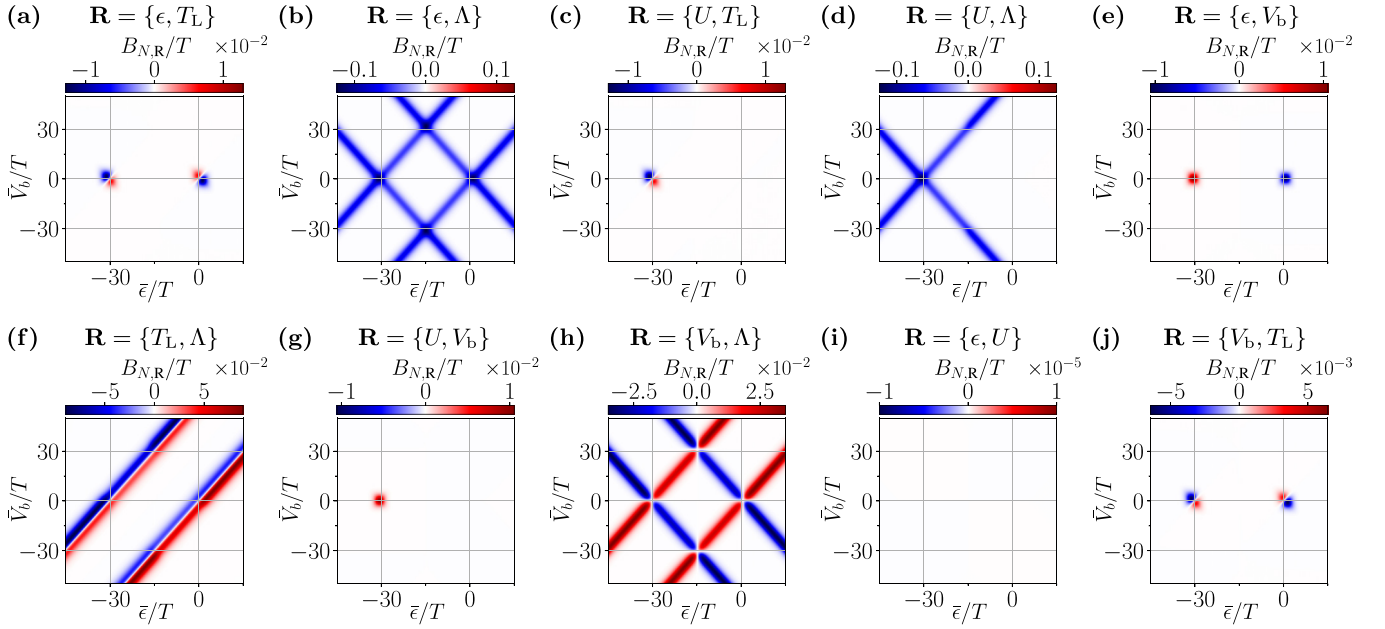
FIG. 7. Pumping curvatures $\mathbf{B}_{NR}$ for a quantum dot with repulsive on-site interaction, $U > 0$, in the $(\bar{\epsilon}, \bar{V}_b)$ space for all possible two-parameter driving schemes $\mathbf{R} = \{R_1, R_2\}$. We have plotted the component of $\mathbf{B}_{NR}$ perpendicular to the driving plane defined by (R_1, R_2). The way the driving is done and the choice of all other parameters are the same as in Fig. 3.

translates to the parity component $\mathbf{A}_{H\alpha}^{P}(\mathbf{R})$ of the geometric connection given in Eq. (35),

$$\mathcal{D}\mathbf{A}_{H\alpha}^{P}(\mathbf{R}) = U\gamma_{p\alpha}\mathcal{D}\mathbf{x}^{P} = +\tilde{\sigma}_{\mathcal{D}}\mathbf{A}_{H\alpha}^{P}(\mathbf{R}), \qquad \text{(C19)}$$

and to the corresponding pumping curvature

$$\begin{aligned}\mathcal{D}\mathbf{B}_{H\alpha}^{P}(\mathbf{R}) &= \tilde{\sigma}_{\mathcal{D}}\nabla_{\mathbf{R}} \times \mathcal{D}\mathbf{A}_{H\alpha}^{P}(\mathbf{R}) \\ &= [\tilde{\sigma}_{\mathcal{D}}\nabla_{\mathbf{R}}] \times [\tilde{\sigma}_{\mathcal{D}}\mathbf{A}_{H\alpha}^{P}(\mathbf{R})]. \qquad \text{(C20)}\end{aligned}$$

To show the symmetry of $\mathbf{B}_{H\alpha}^{P}(\mathbf{R})$ with respect to the sign of a time-independent interaction U, we now apply the particle-hole parameter transform $\mathcal{T}$ defined in Eqs. (C1)–(C20) from the left and shift it through to the right. Using Eqs. (C9) and (C14), this gives

$$\begin{aligned}\mathbf{B}_{H\alpha}^{P}&(\mathbf{R})|_{\bar{\epsilon}\to\bar{\epsilon}-\bar{U}}|_{\bar{U}\to-\bar{U}} \\ &= \mathcal{T}\mathcal{D}\mathbf{B}_{H\alpha}^{P}(\mathbf{R}) \\ &= [\tilde{\sigma}_{\mathcal{D}}\tilde{\sigma}\nabla_{\mathbf{R}}] \times [\tilde{\sigma}_{\mathcal{D}}\tilde{\sigma}\mathbf{A}_{H\alpha}^{P}(\mathbf{R})], \qquad \text{(C21)}\end{aligned}$$

with

$$\tilde{\sigma}_{\mathcal{D}}\tilde{\sigma} = \tilde{\sigma}\tilde{\sigma}_{\mathcal{D}} = \begin{pmatrix} 1 & 0 & 0 & 0_{1\times2} \\ 1 & -1 & 0 & 0_{1\times2} \\ 0 & 0 & 1 & 0_{1\times2} \\ 0_{2\times1} & 0_{2\times1} & 0_{2\times1} & 1_{2\times2} \end{pmatrix}. \qquad \text{(C22)}$$

As long as U is not driven, the second row and column of $\tilde{\sigma}_{\mathcal{D}}\tilde{\sigma}$ are excluded, the matrix $\tilde{\sigma}_{\mathcal{D}}\tilde{\sigma}$ becomes a 4×4 identity, and the interaction-inversion symmetry

$$\mathbf{B}_{H\alpha}^{P}(\mathbf{R}) = \mathbf{B}_{H\alpha}^{P}(\mathbf{R})|_{\bar{\epsilon}\to\bar{\epsilon}-\bar{U}}|_{\bar{U}\to-\bar{U}} \quad \text{if } \partial_t U = 0 \qquad \text{(C23)}$$

follows. In other words, the paritylike curvature $\mathbf{B}_{H\alpha}^{P}$ for constant attractive interaction $\bar{U} < 0$ is equal to $\mathbf{B}_{H\alpha}^{P}$ evaluated for repulsive interaction $-\bar{U} > 0$ and a working point $\bar{\epsilon}$ shifted by $\bar{U} = -|\bar{U}|$. A comparison of the small panels in Fig. 3 to the corresponding panels in Fig. 4 indeed confirms this. Beyond

this, Eq. (C21) also reveals the behavior with U as one driving parameter:

$$\begin{aligned}\mathbf{B}_{H\alpha}^{P}(\{U, R_2\}) &= -\mathbf{B}_{H\alpha}^{P}(\{U, R_2\})|_{\bar{\epsilon}\to\bar{\epsilon}-\bar{U}}|_{\bar{U}\to-\bar{U}} \\ &\quad + \mathbf{B}_{H\alpha}^{P}(\{\epsilon, R_2\}). \qquad \text{(C24)}\end{aligned}$$

For the special case of $R_1 = \epsilon$ and $R_2 = U$, we find

$$\mathbf{B}_{H\alpha}^{P}(\{\epsilon, U\}) = -\mathbf{B}_{H\alpha}^{P}(\{\epsilon, U\})|_{\bar{\epsilon}\to\bar{\epsilon}-\bar{U}}|_{\bar{U}\to-\bar{U}}, \qquad \text{(C25)}$$

as can be seen by comparing Fig. 3(i) to Fig. 4(i). Altogether, Eqs. (C23) and (C25) are explicit analytical manifestations of the strong similarities between energy pumping for attractive and repulsive interactions observed at large bias $|V_b| \geqslant |U|$.

APPENDIX D: CHARGE PUMPING

Geometrical charge pumping for both a repulsive and an attractive interaction has already been studied in Refs. [6,31,71]. Nevertheless, to make the comparison with our results for energy pumping in Sec. IV easier, we also plot the pumping curvatures $\mathbf{B}_{NR}(\mathbf{R})$ in Fig. 7 for $U > 0$ and in Fig. 8 for $U < 0$. There are no surfaces of finite pumping curvature due to off-resonant pumping (absence of mechanisms G and H). For $U > 0$, the most present mechanism is A, namely, at a double resonance at zero bias voltage, while lines at single resonances can be obtained when Λ is a driving parameter (see Sec. IV A 1). For $U < 0$, the only mechanism is C (see Sec. IV B 1 and Appendix H 1).

APPENDIX E: QUASISTATIONARY EXCHANGE WITH ENVIRONMENT

We argue at several points in Sec. IV A 1 that the charge pumping curvature $\mathbf{B}_N = \sum_\alpha \mathbf{B}_{N\alpha}$ for the total lead-summed
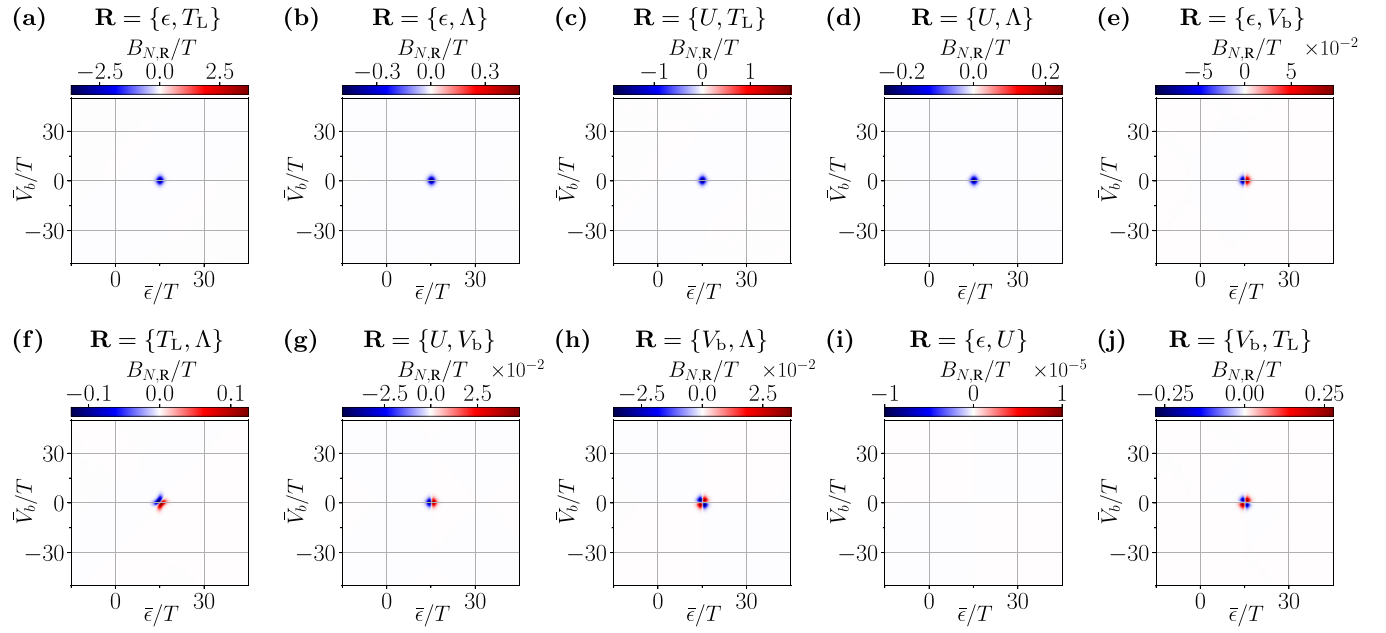
FIG. 8. Pumping curvatures $\mathbf{B}_{N\mathbf{R}}$ for a quantum dot with attractive on-site interaction, $U < 0$, in the $(\bar{\epsilon}, \bar{V}_{\mathrm{b}})$ space for all possible two-parameter driving schemes $\mathbf{R} = \{R_1, R_2\}$. We have plotted the component of $\mathbf{B}_{N\mathbf{R}}$ perpendicular to the driving plane defined by (R_1, R_2). The way the driving is done and the choice of all other parameters are the same as in Fig. 3.

system must vanish due to total charge conservation.[15] Furthermore, we argue that this exact vanishing is not generally true for the energy pumping curvature $\mathbf{B}_H$, as dot parameter driving does work on particles occupying the dot. This Appendix derives both statements.

First of all, for any observable $\hat{\mathcal{O}}$, the total stationary current entering the dot is zero by definition: $I_{\mathcal{O}}^{(0)} = I_{\mathcal{O}L}^{(0)} + I_{\mathcal{O}R}^{(0)} = (\mathcal{O}|W|z) = 0$. However, for the total lead-summed first nonadiabatic correction $I_{\mathcal{O}}^{(1)} = \mathbf{A}_{\mathcal{O}} \cdot \partial_t \mathbf{R}$, Eq. (22) and $\sum_\alpha W^\alpha / \tilde{W} = 1 - |z)(\mathbb{1}|$ dictate

$$\mathbf{A}_{\mathcal{O}} = (\mathcal{O}|\boldsymbol{\nabla}_{\mathbf{R}}|z). \tag{E1}$$

This means that

$$\mathbf{B}_{\mathcal{O}} = [\boldsymbol{\nabla}_{\mathbf{R}}(\mathcal{O}|] \times [\boldsymbol{\nabla}_{\mathbf{R}}|z)]. \tag{E2}$$

Since the occupation number $\hat{\mathcal{O}} = \hat{N}$ is parameter independent, $\boldsymbol{\nabla}_{\mathbf{R}}\hat{N} = 0$, the curvature vanishes, $\mathbf{B}_N = 0$, expressing that in the stationary limit, total charge conservation prohibits any net charge buildup in the dot averaged over a driving cycle. However, for $\hat{\mathcal{O}} = \hat{H}$, any derivative with respect to ϵ or U is generally finite. More explicitly, inserting a unit formed by the spin-degenerate basis operators $|\mathbb{1})/2$, $|N - \mathbb{1})/\sqrt{2}$, and $|(-\mathbb{1})^N)/2$ into Eqs. (E1) and (E2) and using that $(H|N - \mathbb{1})/2 = \epsilon + U/2$ as well as $(H|(-\mathbb{1})^N)/4 = U/4$, we find

$$\mathbf{A}_H = \left[\epsilon + \frac{U}{2}\right]\boldsymbol{\nabla}_{\mathbf{R}}N_z + \frac{U}{4}\boldsymbol{\nabla}_{\mathbf{R}}p_z,$$

$$\mathbf{B}_H = \boldsymbol{\nabla}_{\mathbf{R}}\left[\epsilon + \frac{U}{2}\right] \times \boldsymbol{\nabla}_{\mathbf{R}}N_z + \frac{1}{4}\boldsymbol{\nabla}_{\mathbf{R}}U \times \boldsymbol{\nabla}_{\mathbf{R}}p_z. \tag{E3}$$

---

[15]In the fully left-right symmetric case, the lead-resolved curvature $\mathbf{B}_{N\alpha}$ is proportional to $\mathbf{B}_N$ and hence also vanishes.

Hence, if ϵ or U is among the driving parameters, there is generally a finite net work done on the dot that results in a net cycle-averaged energy flow into the leads, $\Delta H^{(1)} \neq 0$. This is however not the case for a completely unbiased environment, with fixed $\delta T = V_{\mathrm{b}} = 0$: Here $|z_\alpha) = |z)$ means that a driven coupling asymmetry Λ has no effect on $|z)$ and that $f_\epsilon^\pm \to f_\alpha^\pm(\epsilon)$ and $f_U^\pm \to f_\alpha^\pm(\epsilon + U)$ in Eq. (13) imply for Eq. (E3) that

$$\mathbf{B}_H \overset{\delta T, V_{\mathrm{b}} \to 0}{\to} 0. \tag{E4}$$

This is confirmed by Figs. 4(b), 4(d), and 4(i) and shown approximately in Appendix H 2 for $U < 0$, but it holds exactly and for any interaction sign. It is also consistent with the usual understanding that equilibrium heating is an effect of at least second order in the driving frequency [41].

APPENDIX F: CHARGE AND ENERGY PUMPING THROUGH A NONINTERACTING DOT

The charge and energy pumping curvatures $\mathbf{B}_{N\mathbf{R}}$ and $\mathbf{B}_{H\mathbf{R}}$ for a noninteracting quantum dot, namely, with $U = 0$, are plotted in Fig. 9 for a few driving schemes. This figure evidences the existence of interaction-induced pumping terms. For instance, the contribution of mechanism A to charge pumping for $\mathbf{R} = \{\epsilon, T_{\mathrm{L}}\}$ and $U > 0$ [Fig. 7(a)] is absent in Fig. 9(a). For energy pumping, mechanism B, which requires a double resonance (Fig. 2), also vanishes in the absence of interaction (Fig. 3 compared to the bottom row of Fig. 9). Similarly, mechanism C for $U < 0$ (Figs. 8 and 4) is absent from Fig. 9. However, when Λ is one of the driving parameters, both charge and energy pumping are always possible, with and without interaction, like, for instance, in Fig. 9(b). Additionally, Figs. 9(a) and 9(c) are simple examples of energy pumping in the absence of charge pumping.
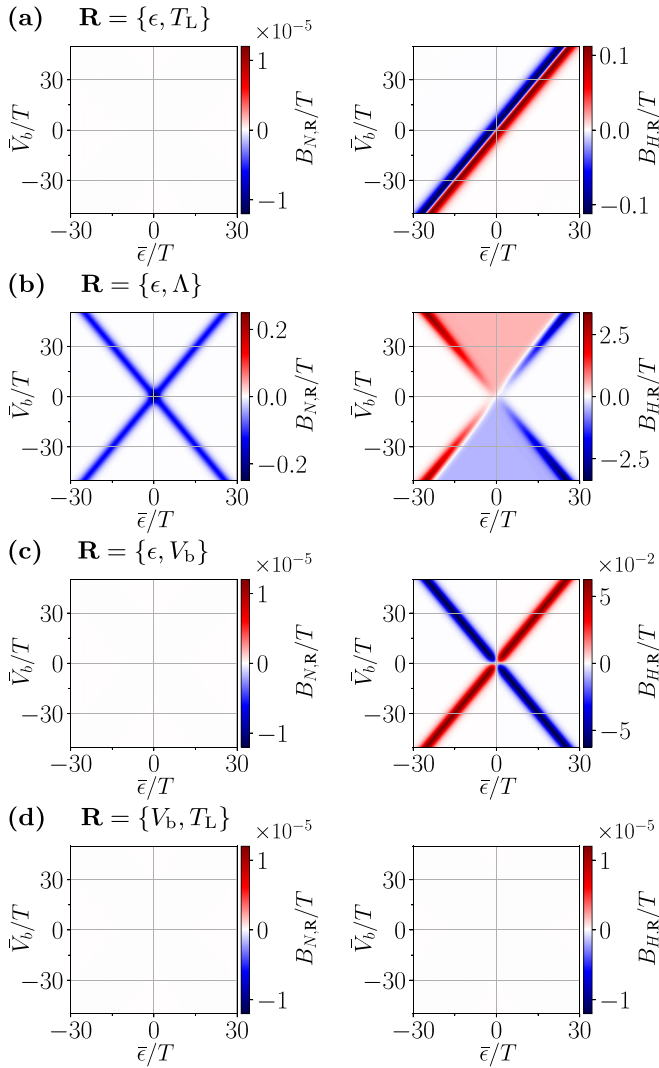
(a) $\mathbf{R} = \{\epsilon, T_\mathrm{L}\}$

(b) $\mathbf{R} = \{\epsilon, \Lambda\}$

(c) $\mathbf{R} = \{\epsilon, V_\mathrm{b}\}$

(d) $\mathbf{R} = \{V_\mathrm{b}, T_\mathrm{L}\}$

FIG. 9. Pumping curvatures $\mathbf{B}_{N\mathbf{R}}$ (left column) and $\mathbf{B}_{H\mathbf{R}}$ (right column) for a noninteracting quantum dot, namely, $U = 0$, in the $(\bar{\epsilon}, \bar{V}_\mathrm{b})$ space. The way the driving is done and the choice of all other parameters are the same as in Fig. 3.

APPENDIX G: ANALYTICAL RESULTS FOR SINGLE-RESONANCE PUMPING

In this Appendix we derive analytical pumping curvature expressions for repulsive interaction $U > 0$ and constant coupling asymmetry Λ in the single-resonance case, that is, with one lead α' being far off resonance. We start by noting that the kernel $W^{\alpha'}$ for this nonresonant lead and all its derived quantities become independent of any driving parameter $R_i \neq \Lambda$, namely,

$$\frac{\partial_{R_i} W^{\alpha'}}{\Gamma} \sim \frac{\partial_{R_i} \gamma_{c\alpha'}}{\Gamma} \sim \partial_{R_i} N_{z\alpha'} \approx 0. \qquad \text{(G1)}$$

Note that we cannot generally approximate the dual occupation $\partial_{R_i} N_{z\alpha'}^{\mathrm{i}} \approx 0$, since the latter changes at the resonances of the dual attractive system, different from the resonances in the repulsive system of interest. Using these results, we aim at expressing the pumping curvature in terms of lead-resolved quantities to make them easier to interpret and in particular

show that $\mathbf{B}_{N\mathbf{R}}(\mathbf{R})$ vanishes. Using that the total occupation number can be decomposed into [81]

$$N_z = \sum_{\alpha''} \frac{\gamma_{c\alpha''}}{\gamma_c} N_{z\alpha''} \qquad \text{(G2)}$$

and that $\sum_{\alpha''} \gamma_{c\alpha''} = \gamma_c$ means $\gamma_{c\alpha}/\gamma_c = 1 - \gamma_{c\alpha'}/\gamma_c$ for two leads, we can use Eq. (G1) to rewrite

$$\partial_{R_i} N_z \to \partial_{R_i}\left(\frac{\gamma_{c\alpha}}{\gamma_c}\right)(N_{z\alpha} - N_{z\alpha'}) + \frac{\gamma_{c\alpha}}{\gamma_c}\partial_{R_i} N_{z\alpha}. \qquad \text{(G3)}$$

Near a resonance of the repulsive dot, i.e., for parameters deviating from the particle-hole symmetric point, the lead-resolved charge rate $\gamma_{c\alpha}$ can be expressed [79] in terms of the lead-resolved coupling Γ_α, stationary occupation $N_{z\alpha}$, and dual occupation $N_{z\alpha}^{\mathrm{i}}$:

$$\gamma_{c\alpha} = \gamma_{p\alpha} \frac{N_{z\alpha}^{\mathrm{i}} - 1}{N_{z\alpha}^{\mathrm{i}} - N_{z\alpha}}. \qquad \text{(G4)}$$

For $\partial_{R_i} \gamma_{c\alpha'} \to 0$, the derivative of the charge rate ratio in Eq. (G3) thereby can be decomposed into

$$\partial_{R_i}\left(\frac{\gamma_{c\alpha}}{\gamma_c}\right) \to -\frac{\gamma_{c\alpha'}}{\gamma_c^2}\partial_{R_i}\gamma_{c\alpha}$$

$$= -\frac{\gamma_{c\alpha'}\gamma_{c\alpha}\gamma_{c\alpha}^{\mathrm{i}}}{\gamma_{p\alpha}\gamma_c^2}\frac{1}{N_{z\alpha}^{\mathrm{i}} - 1}\partial_{R_i}N_{z\alpha}^{\mathrm{i}}$$

$$- \frac{\gamma_{c\alpha'}\gamma_{c\alpha}}{\gamma_c^2}\frac{1}{N_{z\alpha}^{\mathrm{i}} - N_{z\alpha}}\partial_{R_i}N_{z\alpha}, \qquad \text{(G5)}$$

with $\gamma_{c\alpha}^{\mathrm{i}} = \gamma_{p\alpha} - \gamma_{c\alpha}$. For the charge pumping curvature of the resonant lead α, using Eqs. (G3) and (G5) gives

$$\mathbf{B}_{N\alpha}(\mathbf{R}) \to \nabla_{\mathbf{R}}\left(\frac{\gamma_{c\alpha}}{\gamma_c}\right) \times \left[(N_{z\alpha} - N_{z\alpha'})\left(\nabla_{\mathbf{R}}\frac{\gamma_{c\alpha}}{\gamma_c}\right)\right.$$

$$\left. + \frac{\gamma_{c\alpha}}{\gamma_c}\nabla_{\mathbf{R}}N_{z\alpha}\right]$$

$$= \nabla_{\mathbf{R}}\left(\frac{\gamma_{c\alpha}}{\gamma_c}\right) \times \frac{\gamma_{c\alpha}}{\gamma_c}\nabla_{\mathbf{R}}N_{z\alpha}$$

$$= -\frac{\gamma_{c\alpha'}\gamma_{c\alpha}^2\gamma_{c\alpha}^{\mathrm{i}}}{\gamma_{p\alpha}\gamma_c^3}\frac{1}{N_{z\alpha}^{\mathrm{i}} - 1}\nabla_{\mathbf{R}}N_{z\alpha}^{\mathrm{i}} \times \nabla_{\mathbf{R}}N_{z\alpha}. \qquad \text{(G6)}$$

This quantity vanishes in the single-resonance case because the finite gradient $\nabla_{\mathbf{R}}N_{z\alpha}$ near resonance is overcompensated by the nearly vanishing gradient of the inverted dual charge, $\nabla_{\mathbf{R}}N_{z\alpha}^{\mathrm{i}} \approx 0$, whose inverted interaction causes its transition energies to be far away from resonance with μ_α for $U \gg T_\alpha > 0$.

When driving temperature and bias voltage for constant U and Γ_α, the above derivation of the vanishing curvature from the properties of the dual charges $N_{z\alpha}^{\mathrm{i}}$ and N_z^{i} can also be extended to the energy current. To do so, we are going to collect all terms in $\nabla_{\mathbf{R}}N_z$ separately from terms in $\nabla_{\mathbf{R}}p_z$ in the geometric connection $\mathbf{A}_{H\mathbf{R}}(\mathbf{R})$, unlike in Eq. (28). The key ingredient for this is that according to Ref. [79], Eq. (G4) generalizes in a remarkably simple fashion to the full charge rate

$$\gamma_c = \sum_\alpha \gamma_{c\alpha} = \gamma_p \frac{N_z^{\mathrm{i}} - 1}{N_z^{\mathrm{i}} - N_z}. \qquad \text{(G7)}$$

This, together with $\gamma_{p\alpha}/\gamma_p = \Gamma_\alpha/\Gamma$, enables us to rewrite the finite-bias correction to the coefficient $a_{H\alpha}^C$ given in Eq. (32b) as

$$
\begin{aligned}
a_{H\alpha}^{C,NTC} &= \frac{U}{2}\frac{\gamma_{p\alpha}}{\gamma_c}\left[\left(N_{z\alpha}^i - 1\right) - \left(N_z^i - 1\right)\right] \\
&= \frac{U}{2}\frac{\gamma_{p\alpha}}{\gamma_c}\left[\frac{\gamma_{c\alpha}}{\gamma_{p\alpha}}\left(N_{z\alpha}^i - N_{z\alpha}\right) - \frac{\gamma_c}{\gamma_p}\left(N_z^i - N_z\right)\right] \\
&= \frac{\gamma_{c\alpha}}{\gamma_c}\frac{U}{2}\left(N_{z\alpha}^i - N_{z\alpha}\right) + \frac{U\Gamma_\alpha}{2\Gamma}\left(N_z - N_z^i\right). \quad \text{(G8)}
\end{aligned}
$$

We can now straightforwardly sum Eq. (G8) with $a_{H\alpha}^{P,N}$ given in Eq. (31c), yielding

$$
\begin{aligned}
\tilde{a}_{H\alpha}^C &= a_{H\alpha}^C + a_{H\alpha}^{P,N} \\
&= \left[\epsilon + \frac{U}{2}(2 - N_{z\alpha})\right]\frac{\gamma_{c\alpha}}{\gamma_c} + \frac{U}{2}\frac{\gamma_{p\alpha}}{\gamma_p}(N_z - 1). \quad \text{(G9)}
\end{aligned}
$$

We can thus rewrite the geometric connection

$$
\mathbf{A}_{H\alpha}(\mathbf{R}) = \tilde{a}_{H\alpha}^C\boldsymbol{\nabla}_{\mathbf{R}}N_z + a_{H\alpha}^{P,p}\boldsymbol{\nabla}_{\mathbf{R}}p_z. \quad \text{(G10)}
$$

The key difference between $\tilde{a}_{H\alpha}^C$ and $a_{H\alpha}^C$ [Eq. (31a)] is that, unlike for the tight-coupling energy (33), the prefactor in front of the charge rate ratio $\gamma_{c\alpha}/\gamma_c$ in Eq. (G9) depends on the actual lead-resolved occupation $N_{z\alpha}$, and not on the dual $N_{z\alpha}^i$, and the finite-bias correction $\sim\gamma_{p\alpha}/\gamma_p$ likewise depends on N_z instead of N_z^i. This difference simplifies the analytical expression for the energy pumping curvature $\mathbf{B}_{H\alpha}(\mathbf{R})$ whenever U and the couplings Γ_α are constant during the driving cycle. Namely, with $\boldsymbol{\nabla}_{\mathbf{R}}a_{H\alpha}^{P,p} = \boldsymbol{\nabla}_{\mathbf{R}}\frac{U}{4}\frac{\gamma_{p\alpha}}{\gamma_p} \to 0$ and $\boldsymbol{\nabla}_{\mathbf{R}}N_z \times \boldsymbol{\nabla}_{\mathbf{R}}N_z = 0$, the only terms $\sim\boldsymbol{\nabla}_{\mathbf{R}}N_z$ which survive when inserting Eq. (G10) into Eq. (30) are

$$
\begin{aligned}
\mathbf{B}_{H\alpha}(\mathbf{R}) &\overset{U,\Gamma_\alpha \text{ const}}{\to} \boldsymbol{\nabla}_{\mathbf{R}}\tilde{a}_{H\alpha}^C \times \boldsymbol{\nabla}_{\mathbf{R}}N_z \\
&\overset{U,\Gamma_\alpha \text{ const}}{\to} \left[\epsilon + \frac{U}{2}(2 - N_{z\alpha})\right]\mathbf{B}_{N\alpha}(\mathbf{R}) \\
&\quad + \left[\boldsymbol{\nabla}_{\mathbf{R}}\epsilon - \frac{U}{2}\boldsymbol{\nabla}_{\mathbf{R}}N_{z\alpha}\right]\frac{\gamma_{c\alpha}}{\gamma_c} \times \boldsymbol{\nabla}_{\mathbf{R}}N_z. \quad \text{(G11)}
\end{aligned}
$$

The form (G11) provides useful estimates of the pumped energy for constant tunnel couplings Γ_α in the single-resonance case.[16] Most importantly, if we set V_b as well as any temperature $T_{\alpha''}$ of the two leads as driving parameters and assume the nonresonant lead α' to fulfill the condition (G1), we can use Eq. (G6) in Eq. (G11) to simplify $\mathbf{B}_{H\alpha}(\{V_b, T_{\alpha''}\})$ to

$$
\begin{aligned}
\mathbf{B}_{H\alpha}(\{V_b, T_{\alpha''}\}) &\to \left[\epsilon + \frac{U}{2}(2 - N_{z\alpha})\right]\mathbf{B}_{N\alpha}(\{V_b, T_{\alpha''}\}) \\
&\quad - \frac{U}{2}\frac{\gamma_{c\alpha}}{\gamma_c}\boldsymbol{\nabla}_{\mathbf{R}}N_{z\alpha} \times \boldsymbol{\nabla}_{\mathbf{R}}N_z
\end{aligned}
$$

---

[16]However, at first glance, Eq. (G11) suggests $\epsilon + (U/2)(2 - N_{z\alpha})$ to be the energy effectively transported with the pumped charge current, which is misleading. For example, for $U > 0$, this energy would approach $\epsilon + U$, close to a resonance at which $N_{z\alpha} \approx 0$ and at which we would instead expect a pumped energy $\sim\epsilon$, as correctly predicted by the tight-coupling term (33). Moreover, the second line of Eq. (G11) typically contributes significantly whenever $\mathbf{B}_{N\alpha}(\mathbf{R}) \neq 0$.

$$
\begin{aligned}
&= \left[\epsilon + \frac{U}{2}(2 - N_{z\alpha})\right]\mathbf{B}_{N\alpha}(\{V_b, T_{\alpha''}\}) \\
&\quad + \frac{U}{2}(N_{z\alpha} - N_{z\alpha'})\left(\boldsymbol{\nabla}_{\mathbf{R}}\frac{\gamma_{c\alpha}}{\gamma_c}\right) \\
&\quad \times \frac{\gamma_{c\alpha}}{\gamma_c}\boldsymbol{\nabla}_{\mathbf{R}}N_{z\alpha} \\
&\to \left[\epsilon + \frac{U}{2}(2 - N_{z\alpha'})\right]\mathbf{B}_{N\alpha}(\{V_b, T_\alpha\}). \\
&\quad\quad\quad\quad\quad\quad\quad\quad\quad\quad\quad\quad\quad\quad \text{(G12)}
\end{aligned}
$$

A vanishing charge pumping curvature thereby dictates a vanishing energy pumping curvature.

APPENDIX H: ANALYTICAL RESULTS FOR THE TWO-PARTICLE RESONANCE

This Appendix analyzes more in detail charge and energy pumping for an attractive interaction $U < 0$ close to the two-particle resonance $\epsilon/T \approx -U/2T$, by studying the analytical expressions of the pumping curvatures for $|V_b| \leqslant |U|$ (mechanism C).

1. Charge pumping

The identities $N_z = \sum_\alpha(\gamma_{c\alpha}/\gamma_c)N_{z\alpha}$ [Eq. (G2)] and $\sum_\alpha(\gamma_{c\alpha}/\gamma_c) = 1$ for arbitrary interaction energy U show that charge pumping is suppressed at finite bias voltage (mechanisms $C^\pm$). Indeed, at $|U| > |V_b| \geqslant T$ and $\epsilon/T \approx -U/2T$, the dot is actually off-resonance with each individual lead due to the bias. This off-resonance condition and the strong pairing effect exponentially suppress any parameter dependence of the individual $N_{z\alpha}$. The total charge gradient $\boldsymbol{\nabla}_{\mathbf{R}}N_z$ is therefore proportional to the gradient of the charge rate ratio $\gamma_{c\alpha}/\gamma_c$,

$$
\boldsymbol{\nabla}_{\mathbf{R}}N_z \approx (N_{z\alpha} - N_{z\alpha'})\boldsymbol{\nabla}_{\mathbf{R}}\left(\frac{\gamma_{c\alpha}}{\gamma_c}\right). \quad \text{(H1)}
$$

This, together with the expression (34) for $a_{N\alpha}^C$, dictates $\boldsymbol{\nabla}_{\mathbf{R}}a_{N\alpha}^C$ and $\boldsymbol{\nabla}_{\mathbf{R}}N_z$ to be parallel and hence a vanishing charge pumping curvature (43).

Around $V_b = 0$, all driving schemes yield a sizable pumped charge, except for $\mathbf{R} = \{\epsilon, U\}$, as shown by Fig. 8. The latter exception is, just as for $U > 0$, due to both leads being effectively identical when $|V_b| = T_L - T = 0$: The contacts thereby combine to a single equilibrium environment with vanishing cycle-averaged particle transfer to the dot due to total charge conservation (Appendix E).

However, if only one of the dot energies ϵ or U is driven together with T_L or Λ, the latter two parameters affect the left-right lead-dot coupling balance. The ϵ or U driving at mechanism C with $|V_b|/T \approx 0$ then makes the dot more likely to accept particles when coupled more strongly to one lead compared to when coupled more strongly to the other. This yields a net pumped charge current [Figs. 8(a)–8(d)] whose sign is only determined by the driving sequence, but not by the precise working-point level $\bar{\epsilon}$ and bias voltage $\bar{V}_b$ around $\bar{\epsilon} = -\bar{U}/2$ and $\bar{V}_b = 0$.

The finite pumped charge for the driving schemes $\mathbf{R} = \{R_1, V_b\}$, with $R_1 = \epsilon, U$, arises because the dot energy driving changes the transmission strength for times with positive bias

relative to the transmission strength for times with negative bias. Depending on the driving phase ϕ in Eq. (5), a working point $\bar{\epsilon} < -\bar{U}/2$ could then mean that the dot approaches the two-particle resonance while $V_b(t) < 0$, but moves further away from this resonance while $V_b(t) > 0$, which would favor charge transport from right to left. The situation is reversed for $\bar{\epsilon} > -\bar{U}/2$ and the same driving phase ϕ, thereby introducing an $\bar{\epsilon}$-dependent sign change of $\mathbf{B}_{N\alpha}(\mathbf{R})$ [Figs. 8(e) and 8(g)].

If the dot energies remain constant and V_b is instead driven together with T_L or Λ affecting the left-right coupling balance, the sign of $\mathbf{B}_{N\alpha}(\mathbf{R})$ changes as a function of both $\bar{\epsilon}$ and $\bar{V}_b$ around $\bar{\epsilon} = -\bar{U}/2$ and $\bar{V}_b = 0$ [Figs. 8(h) and 8(j)]. The positive sign for $\bar{\epsilon} > -\bar{U}/2$ and $\bar{V}_b > 0$ and for $\bar{\epsilon} < -\bar{U}/2$ and $\bar{V}_b < 0$ means that the left/right lead potential $\bar{\mu}_\alpha$ is on average closer to a two-particle resonance with the dot during cycle times in which the left/right lead is also more strongly coupled; the complementary working-point regimes with negative charge pumping curvature sign correspond to the reversed relation between resonance and coupling.

Finally, for $\mathbf{R} = \{T_L, \Lambda\}$, the pumped charge switches signs when crossing the line $\bar{\mu}_L = \bar{\epsilon} + \bar{U}/2$ [Fig. 8(f)]. Indeed, in this case, using Eq. (G2), we get

$$\partial_\Lambda N_z = (N_{z\alpha} - N_{z\alpha'})\partial_\Lambda\left(\frac{\gamma_{c\alpha}}{\gamma_c}\right),$$

$$\partial_{T_L} N_z = (N_{z\alpha} - N_{z\alpha'})\partial_{T_L}\left(\frac{\gamma_{c\alpha}}{\gamma_c}\right) + \frac{\gamma_{cL}}{\gamma_c}\partial_{T_L}N_{zL}, \quad \text{(H2)}$$

and therefore

$$B_{N\alpha}(\{T_L, \Lambda\}) = -T\,\partial_\Lambda\left(\frac{\gamma_{c\alpha}}{\gamma_c}\right)\frac{\gamma_{cL}}{\gamma_c}\partial_{T_L}N_{zL}. \quad \text{(H3)}$$

The derivative $\partial_\Lambda(\gamma_{c\alpha}/\gamma_c)$ has a constant sign, while the sign of $\partial_{T_L} N_{zL}$ depends on the working-point level position $\bar{\epsilon}$ relative to the two-particle resonance with the left lead: N_{zL} increases with T_L for $\bar{\epsilon} + \bar{U}/2 < \bar{\mu}_L$ due to the increase in the number of available electrons in the lead at energy $\bar{\epsilon}$ and, on the contrary, N_{zL} decreases with T_L for $\bar{\epsilon} + \bar{U}/2 > \bar{\mu}_L$ due to the increased number of available holes in the lead at energy $\bar{\epsilon} + \bar{U}$.

2. Energy pumping

The energy pumping curvature $|V_b| < |U|$ is purely charge-like, $\mathbf{B}_{H\alpha}(\mathbf{R}) \approx \mathbf{B}^C_{H\alpha}(\mathbf{R})$, just as for repulsive interaction. However, close to zero bias, $|V_b|/T \approx 0$, $\mathbf{B}^C_{H\alpha}(\mathbf{R})$ is not dominated by the tightly coupled contribution

$$\mathbf{B}^{C,TC}_{H\alpha}(\mathbf{R}) = \mathcal{E}^\alpha \mathbf{B}_{N\alpha}(\mathbf{R}) + \frac{\gamma_{c\alpha}}{\gamma_c}\nabla_\mathbf{R}\mathcal{E}^\alpha \times \nabla_\mathbf{R}N_z \quad \text{(H4)}$$

coming from Eq. (32a). On the contrary, the main contribution comes from the second term in (32a), $\mathbf{B}^{C,NTC}_{H\alpha}(\mathbf{R}) = \nabla_\mathbf{R}a^{C,NTC}_{H\alpha} \times \nabla_\mathbf{R}N_z$, where $a^{C,NTC}_{H\alpha}$ is defined by Eq. (32b). To see this, we first note that, like for $U > 0$, the tightly coupled contribution $\mathbf{B}^{C,TC}_{H\alpha}(\mathbf{R})$ is small around $\epsilon/T \approx -U/2T$ and $|V_b|/T \approx 0$, since the Seebeck energy $\mathcal{E}^\alpha$ vanishes at this point, and its derivative $\partial_R\mathcal{E}^\alpha$ is nonvanishing only for $R_i = \epsilon, U$ since $N^i_{z\alpha}$ is approximately constant there. Knowing the parameter dependence of N_z for $U < 0$ from the one of N^i_z for $U > 0$, it is clear from Eq. (H4) that only driving ϵ or

U in combination with T_L or Λ gives sizable tight-coupling contributions. However, for $U > 0$ the non-tightly-coupled term $\mathbf{B}^{C,NTC}_{H\alpha}(\mathbf{R})$ vanishes at $|V_b| < U/2$, while it is typically the main contribution to the energy pumping curvature for $U < 0$.

Quantifying the non-tightly-coupled contribution with the expression (32b) for $a^{C,NTC}_{H\alpha}$ is difficult for $U < 0$: Both $N^i_{z\alpha} - N^i_z$ and γ_c are individually suppressed for mechanism C, but their ratio is actually finite. Indeed, $N^i_z \approx N^i_{z\alpha} \approx 1$ at the point of interest $\epsilon/T \approx -U/2T$, which lies in the Coulomb blockade regime for the inverted *repulsive* model. We therefore use the rewriting from Eq. (G8) as a starting point. Then, using Eq. (G2) and labeling the other lead by $\alpha' \neq \alpha$, we obtain

$$a^{C,NTC}_{H\alpha} \approx \frac{U}{2}\left(\frac{\Gamma_{\alpha'}\gamma_{c\alpha}}{\Gamma\gamma_c}(1 - N_{z\alpha}) - \frac{\Gamma_\alpha\gamma_{c\alpha'}}{\Gamma\gamma_c}(1 - N_{z\alpha'})\right). \quad \text{(H5)}$$

For $\Lambda = 0$, $T_L = T$, and $|U| \gg T$, we use the explicit expressions of the Fermi functions and neglect the exponential terms in $U/2T$, since we are interested in the parameters such that $|U|/2T \gg |2\epsilon + U|/2T$ and $|U|/T \gg |V_b|/T$, to obtain

$$a^{C,NTC}_{H\alpha} \approx \frac{U}{4}\tanh\left(\frac{V_b}{2T}\right). \quad \text{(H6)}$$

For $|Vb| < |U|$, N_z depends only on the sign of $\epsilon + U/2$, that is, whether the dot is above or below the particle-hole symmetric point and, as a consequence, $\partial_{V_b}N_z/T \approx 0$. Therefore, when driving the bias voltage, using Eq. (H6), we get

$$B^{C,NTC}_{H\alpha}(\{R_1, V_b\}) = -\frac{\bar{U}}{8}\left[1 - \tanh[2]\left(\frac{\bar{V}_b}{2T}\right)\right]\partial_{R_1}N_z. \quad \text{(H7)}$$

This pumping curvature has the sign of $\partial_{R_1}N_z$ since U is negative. If $R_1 = \epsilon, U$, then $\partial_{R_1}N_z$ is negative for mechanism C since the dot goes from double occupation to empty when crossing the particle-hole symmetric point at $\epsilon = -U/2$ (and $\partial_\epsilon N_z \approx 2\partial_U N_z$). The curvature $B^{C,NTC}_{H\alpha}(\{R_1, V_b\})$ is thus always negative, and suppressed for $|\bar{V}_b| \gg T$, as visible in Figs. 4(e) and 4(g). On the other hand, if $R_1 = \Lambda, T_L$, $\partial_{R_1}N_z$ changes sign with $\bar{V}_b$ and so does the energy pumping curvature [see Figs. 4(h) and 4(j)].

For (ϵ, U) driving, Eq. (H6) gives

$$B^{C,NTC}_{H\alpha}(\{\epsilon, U\}) = -\frac{T^2}{4}\tanh\left(\frac{\bar{V}_b}{2T}\right)\partial_\epsilon N_z. \quad \text{(H8)}$$

The energy pumping curvature thereby has the sign of the bias, vanishes at $\bar{V}_b = 0$, and takes finite values for $T \lesssim |\bar{V}_b| < |U|$ around the particle-hole symmetric point [see Fig. 4(i)]. In other words, as soon as the system deviates from the perfectly balanced case $\bar{V}_b/T = \bar{T}_L/T - 1 = 0$ shown in Appendix E, the energy pumped by (ϵ, U) driving is finite, with the sign of $\bar{V}_b$ determining the sign of the cycle-averaged energy flow.

We now look at (T_L, Λ) driving and compute the derivatives of $a^{C,NTC}_{H\alpha}$ from Eq. (H5). At $\bar{\Lambda} = 0$ and $\bar{T}_L = T$, for $|U| \gg T$ $|U|/2T \gg |2\epsilon + U|/2T$ and $|U|/T \gg |V_b|/T$,

$$\partial_\Lambda a^{C,NTC}_{H\alpha} = \frac{U}{4\gamma_c^2}(\gamma_{c\alpha} - \gamma_{c\alpha'})[\gamma_{c\alpha}(1 - N_{z\alpha}) - \gamma_{c\alpha'}(1 - N_{z\alpha'})]$$

$$\approx \frac{U}{4}\tanh[2]\left(\frac{Vb}{2T}\right)\tanh\left(\frac{2\epsilon + U}{2T}\right) \quad \text{(H9)}$$

and

$$\partial_{T_L} a_{H\alpha}^{C,NTC} \approx U \frac{2\bar{\epsilon} + U - V_b + U \tanh\left(\frac{2\epsilon + U}{2T}\right)}{16T \cosh[2]\left(\frac{V_b}{2T}\right)}. \quad \text{(H10)}$$

The derivative $\partial_{\Lambda} a_{H\alpha}^{C,NTC}$ [Eq. (H9)] expectedly vanishes at $\bar{V}_b = 0$, since both leads are identical at the working point $\bar{T}_L = T$ and thus together behave as one unique equilibrium environment. The derivative precisely at $\epsilon = -U/2$ also goes to zero for $V_b \neq 0$, as $f_{\alpha/\alpha'}^+(\epsilon) \overset{\epsilon=-U/2}{=} f_{\alpha'/\alpha}^-(\epsilon + U)$ for $\bar{T}_L = \bar{T}_R = T$ means $\gamma_{c\alpha} \overset{\epsilon=-U/2}{=} \gamma_{c\alpha'}$. Flipping the sign of V_b amounts to exchanging the leads, again because $\bar{T}_L = T$, and it is clear from Eq. (H9) that $\partial_{\Lambda} a_{H\alpha}^{C,NTC}$ is unchanged under $\alpha \leftrightarrow \alpha'$. Consequently, the sign of the Λ derivative is independent of V_b, but changes with $\epsilon + U/2$. Turning to $\partial_{T_L} a_{H\alpha}^{C,NTC}$, Eq. (H10) indicates a strong suppression for $|V_b| \gg T$. At low bias $|V_b|/T \ll 1$, the derivative $\partial_{T_L} a_{H\alpha}^{C,NTC}$ changes sign as a function of ϵ close to the particle-hole symmetric point, since $|2\epsilon + U - V_b| \rightarrow |V_b| \ll |U|$, while the sign of V_b has no influence. As discussed above, both $\partial_{T_L} N_z$ and $\partial_{\Lambda} N_z$ have the same sign as $\bar{V}_b$ but do not change sign with $\bar{\epsilon} + \bar{U}/2$. Since $\partial_{\Lambda} a_{H\alpha}^{C,NTC}$ and $\partial_{T_L} a_{H\alpha}^{C,NTC}$ have opposite signs as a function of $\bar{\epsilon} + \bar{U}/2$, this results in a pumping curvature with four quadrants with alternating signs around the particle-hole symmetric point [see Fig. 4(f)].

The energy pumping curvature for (ϵ, Λ) driving is given by $B_{H\alpha}^{C,NTC}(\{\epsilon, \Lambda\}) = -\partial_{\Lambda} a_{H\alpha}^{C,NTC} \partial_{\epsilon} N_z$. Since $\partial_{\epsilon} N_z$ has a constant negative value for $\epsilon/T \approx -U/2T$, $B_{H\alpha}^{C,NTC}(\{\epsilon, \Lambda\})$ is mainly determined by $\partial_{\Lambda} a_{H\alpha}^{C,NTC}$ [Eq. (H9)]. This derivative has been shown above to vanish both at $V_b = 0$ and for $\epsilon = -U/2$, but to only change sign with $\epsilon + U/2$, and this is confirmed by Fig. 4(b). For (U, Λ) driving, Eqs. (H5) and (H9) give, for $|U| \gg T$ $|U|/2T \gg |2\epsilon + U|/2T$ and $|U|/T \gg |V_b|/T$,

$$B_{H\alpha}^{C,NTC}(\{U, \Lambda\}) \approx \frac{\tanh[2]\left(\frac{\bar{V}_b}{2T}\right)\left[T + \bar{U} \tanh\left(\frac{2\bar{\epsilon} + \bar{U}}{2T}\right)\right]}{4 \cosh[2]\left(\frac{2\bar{\epsilon} + \bar{U}}{2T}\right)}, \quad \text{(H11)}$$

which predicts a behavior similar to that for (ϵ, Λ) driving given that $|U| \gg T$ [see Fig. 4(d)].

The non-tightly-coupled contribution to the curvature $B_{H\alpha}^{C,NTC}(\{\epsilon, T_L\}) = -T^2 \partial_{T_L} a_{H\alpha}^{C,NTC} \partial_{\epsilon} N_z$ for (ϵ, T_L) driving is suppressed at finite bias voltage [Eq. (H10)] $|V_b| \gg T$. The pumped energy is therefore dominated by the tightly coupled contribution [Eq. (H4)] $B_{H\alpha}^{C,TC}(\{\epsilon, T_L\}) \approx [(1 - \bar{\Lambda})/2]\partial_{T_L} N_z$, which has the same sign as $\bar{V}_b$ [see Fig. 4(a)]. Conversely, at zero bias $|V_b|/T \approx 0$, the non-tightly-coupled term $B_{H\alpha}^{C,NTC}(\{\epsilon, T_L\})$ dominates and changes sign with $\bar{\epsilon} + \bar{U}/2$ but not with $\bar{V}_b$ [Eq. (H10)]. For (U, T_L) driving, the fact that $\partial_U a_{H\alpha}^{C,NTC}$ does not vanish at $V_b > T$ and is of the same order of magnitude as $B_{H\alpha}^{C,TC}(\{U, T_L\})$ makes it difficult to understand the origin of the features in Fig. 4(c). Focusing on $V_b = 0$ only, $\partial_U a_{H\alpha}^{C,NTC} \sim V_b/8$ [Eq. (H6)], $|T \partial_{T_L} N_z| \ll 1$, and $\partial_U N_z \approx \partial_{\epsilon} N_z/2$ imply $B_{H\alpha}^{C,NTC}(\{U, T_L\}) \approx B_{H\alpha}^{C,NTC}(\{\epsilon, T_L\})/2$. This in particular predicts the same sign change of the energy pumping curvature as a function of $\bar{\epsilon} + \bar{U}/2$ as for (ϵ, T_L) driving.

APPENDIX I: ANALYTICAL EXPRESSIONS AT FIRST ORDER IN THE TEMPERATURE DIFFERENCE

This Appendix calculates the transport quantities of Eqs. (52) and (57) from Sec. V, i.e., the heat contributions $Q_R^{(0,1)}$ and work terms $\mathcal{W}_\epsilon^{(1,2)}$ up to linear order in a small left-right temperature difference δT, such that $\bar{T}_L = T + \delta T$ and $|\delta T| \ll T$. We are considering $\bar{\Lambda} = 0$ and $\bar{V}_b = 0$.

The first step is therefore to expand all relevant relaxation rates and stationary averages up to first order in δT around the full-equilibrium values. Since we are looking at the linear response of the system, these expansion will make the equilibrium fluctuations δN_{eq}^2 and $(\delta N_{eq}^i)^2$ appear. We define

$$N_{eq} = N_z|_{eq}, \quad N_{eq}^i = N_z^i|_{eq} = N_{z\alpha}^i|_{eq},$$

$$\gamma_{c,eq} = \gamma_c|_{eq} = \frac{\Gamma}{\Gamma_\alpha} \gamma_{c\alpha}|_{eq},$$

$$\mathcal{E}^{eq} = \mathcal{E}^\alpha|_{eq} = \epsilon + \frac{U}{2}(2 - N_{eq}^i),$$

$$\bar{\mathcal{E}}^{eq} = \mathcal{E}^{eq}|_{H,V_b \to -H,-V_b} = -\epsilon - \frac{U}{2}(2 - N_{eq}),$$

$$\delta N_{eq}^2 = ((N - N_z)^2 |z)|_{eq} = ((N - N_{z\alpha})^2 |z_\alpha)|_{eq},$$

$$(\delta N_{eq}^i)^2 = ((N - N_z^i)^2 |z^i)|_{eq} = ((N - N_{z\alpha}^i)^2 |z_\alpha^i)|_{eq},$$

$$\lambda N_{eq}^3 = ((N - N_z)^3 |z)|_{eq} = ((N - N_{z\alpha})^3 |z_\alpha)|_{eq},$$

$$(\lambda N_{eq}^i)^3 = ((N - N_z^i)^3 |z^i)|_{eq} = ((N - N_{z\alpha}^i)^3 |z_\alpha^i)|_{eq}, \quad \text{(I1)}$$

where $|_{eq}$ corresponds to the limit $\delta T, V_b \to 0$, and $|z_\alpha)$ and $|z_\alpha^i)$ are the stationary state and its dual for the situation in which only the lead α couples to the dot. The skewnesses λN_{eq}^3 and $(\lambda N_{eq}^i)^3$ will appear in the derivatives of the equilibrium charge fluctuations. The expansion of the stationary averages up to linear order in δT around $\delta T, V_b \to 0$ is achieved with the help of the state linearization derived in Eqs. (A31)–(A33) of Ref. [81] for the spin-degenerate single-level quantum dot with energy-independent couplings

$$|z_R) = |z)|_{eq} = |z_{eq}),$$

$$[\partial_{\delta T} |z_L)]|_{eq} = \frac{1}{T^2}[H - (H|z_{eq})\mathbb{1}]|z_{eq}), \quad \text{(I2)}$$

and

$$[\partial_{\delta T} |z)]|_{eq} = \sum_\alpha \frac{\Gamma_\alpha}{\Gamma} [\partial_{\delta T} |z_\alpha)]|_{eq}$$

$$= \frac{1 + \Lambda}{2T^2}[H - (H|z_{eq})\mathbb{1}]|z_{eq})$$

$$\Rightarrow |z) \approx |z_{eq}) + \frac{1 + \Lambda}{2} \frac{\delta T}{T^2}[H - (H|z_{eq})\mathbb{1}]|z_{eq})$$

$$+ O(\delta T^2), \quad \text{(I3)}$$

having used $V_b = 0$ and that for a constant $T_R = T$, $\partial_{\delta T}$ only acts on terms with $\alpha = L$ of the lead sums in Eq. (I3).

Together with Eqs. (A47) and (A48) from Ref. [81], Eqs. (I2) and (I3) imply

$$N_{zR} = N_{eq}, \quad N_{zL} \approx N_{eq} + \delta N_{eq}^2 \frac{\mathcal{E}^{eq}\delta T}{T^2} + O(\delta T^2),$$

$$N_z \approx N_{eq} + \frac{1+\Lambda}{2} \delta N_{eq}^2 \frac{\mathcal{E}^{eq}\delta T}{T^2} + O(\delta T^2). \quad (I4)$$

Since energy inversion commutes with $\partial_{\delta T}$, we obtain the corresponding dual quantities from Eq. (I4) by simply applying the dual parameter transform:

$$N_{zR}^i = N_{eq}^i, \quad N_{zL}^i \approx N_{eq}^i + (\delta N_{eq}^i)^2 \frac{\bar{\mathcal{E}}^{eq}\delta T}{T^2} + O(\delta T^2),$$

$$N_z^i \approx N_{eq}^i + \frac{1+\Lambda}{2} (\delta N_{eq}^i)^2 \frac{\bar{\mathcal{E}}^{eq}\delta T}{T^2} + O(\delta T^2). \quad (I5)$$

To calculate the parity derivative $\partial_{\delta T} p_z = ((-\mathbb{1})^N | \partial_{\delta T} z)$, we first insert the Liouville-space unit operator expansion with respect to the eigenmodes of right-lead kernel W^R and then use Eq. (I4) as well as Eqs. (A55) and (A61) from Ref. [81],

$$\partial_{\delta T} p_z|_{eq} = ((-\mathbb{1})^N |c_R)|_{eq} \partial_{\delta T} N_z|_{eq}$$
$$+ 4[\partial_{\delta T}(z_R^i(-\mathbb{1})^N |z)]|_{eq}$$
$$= \frac{1+\Lambda}{T^2} \left[\mathcal{E}^{eq}(1 - N_{eq}^i) + \frac{U}{2}(\delta N_{eq}^i)^2 \right] \delta N_{eq}^2, \quad (I6)$$

where we have used

$$[\partial_{\delta T}(z_R^i(-\mathbb{1})^N |z)]|_{eq} = \frac{1+\Lambda}{2} \frac{U}{4T^2} \delta N_{eq}^2 (\delta N_{eq}^i)^2. \quad (I7)$$

This means that

$$p_{zR} = p_{eq},$$

$$p_z \approx p_{eq} + \frac{1+\Lambda}{T^2} \left[\mathcal{E}^{eq}(1 - N_{eq}^i) + \frac{U}{2}(\delta N_{eq}^i)^2 \right] \delta N_{eq}^2 \delta T$$
$$+ O(\delta T^2). \quad (I8)$$

Next we need to expand the charge rate ratio γ_{cR}/γ_c. We use Eqs. (G4), (I3), and (I5), $\gamma_c = \gamma_{cR} + \gamma_{cL}$, $\gamma_{cR} = (\Gamma_R/\Gamma)\gamma_{c,eq}$, and $\Gamma_{L/R} = \Gamma(1 \pm \Lambda)/2$ to derive

$$\frac{\gamma_{cR}}{\gamma_c} = \left[1 + \frac{1+\Lambda}{1-\Lambda} \frac{\gamma_p}{\gamma_{c,eq}} \frac{\gamma_{cL}}{\gamma_{pL}} \right]^{-1},$$

$$\frac{\gamma_{cL}}{\gamma_{pL}} \approx \frac{\gamma_{c,eq}}{\gamma_p} + \frac{\gamma_{c,eq}^2}{\gamma_p^2} \frac{\delta N_{eq}^2}{N_{eq}^i - 1} \frac{\mathcal{E}^{eq}\delta T}{T^2} + O(\delta T^2) + \text{inv}, \quad (I9)$$

which means

$$\frac{\gamma_{cR}}{\gamma_c} \approx \frac{1-\Lambda}{2} - \frac{(1-\Lambda^2)\gamma_{c,eq}\delta N_{eq}^2}{4(N_{eq}^i - 1)\gamma_p} \frac{\mathcal{E}^{eq}\delta T}{T^2} + O(\delta T^2) + \text{inv}. \quad (I10)$$

The terms inv are contributions $\sim (\delta N_{eq}^i)^2$ that further below will only appear in products $\sim \delta N_{eq}^2 (\delta N_{eq}^i)^2$ which are more strongly suppressed by the very nature of the dual fluctuations $(\delta N_{eq}^i)^2$ being sizable at different points in parameter space than the fluctuations δN_{eq}^2.

Having determined all relevant quantities up to linear order in δT, we still require the derivatives of these quantities with

respect to ϵ and Λ in order to compute the quantities entering Eqs. (52) and (57). Any quantity derived from the equilibrium state $|z_{eq}) = |z)|_{eq}$ is independent of the tunnel couplings, hence giving a vanishing Λ derivative. For the ϵ derivative, Eq. (A42) from Ref. [81] implies that

$$\partial_\epsilon |z_{eq}) = -\frac{N - N_{eq}\hat{\mathbb{1}}}{T} |z_{eq}), \quad \partial_\epsilon |z_{eq}^i) = \frac{N - N_{eq}^i\hat{\mathbb{1}}}{T} |z_{eq}^i) \quad (I11)$$

and thus

$$\partial_\epsilon N_{eq} = -\frac{1}{T}\delta N_{eq}^2, \quad \partial_\epsilon N_{eq}^i = +\frac{1}{T}(\delta N_{eq}^i)^2,$$

$$\partial_\epsilon \mathcal{E}^{eq} = 1 - \frac{U}{2T}(\delta N_{eq}^i)^2. \quad (I12)$$

For the equilibrium parity $p_{eq} = ((-\mathbb{1})^N |z_{eq})$, we insert the unit expansion of the equilibrium eigenmodes and use that $(z_{eq}^i(-\mathbb{1})^N |\partial_\epsilon |z_{eq}) = -(z_{eq}^i(-\mathbb{1})^N N |z_{eq})/T = 0$ according to the eigenmode orthogonality $(z_{eq}^i(-\mathbb{1})^N |z_{eq}) = 0$ and Eq. (A46) of Ref. [81]:

$$\partial_\epsilon p_{eq} = ((-\mathbb{1})^N |c_{eq})\partial_\epsilon N_{eq} = -\frac{2(1 - N_{eq}^i)}{T}\delta N_{eq}^2. \quad (I13)$$

Moreover, using the definition (I1) of the fluctuations δN_{eq}^2 and $(\delta N_{eq}^i)^2$, the derivative $\partial_\epsilon(N - x\mathbb{1})^n = -n(\partial_\epsilon x)(N - x\mathbb{1})^{n-1}$, and Eq. (I11), we obtain the ϵ derivative of the fluctuations in terms of the skewnesses λN_{eq}^3 and $(\lambda N_{eq}^i)^3$ at full equilibrium:

$$\partial_\epsilon \delta N_{eq}^2 = -\frac{\lambda N_{eq}^3}{T}, \quad \partial_\epsilon (\delta N_{eq}^i)^2 = +\frac{(\lambda N_{eq}^i)^3}{T}. \quad (I14)$$

The derivative of $\gamma_{c,eq}$ with respect to ϵ is given by

$$\partial_\epsilon \gamma_{c,eq} \approx \frac{-\delta N_{eq}^2 \gamma_{c,eq}^2}{T(N_{eq}^i - 1)\gamma_p} + \text{inv}, \quad (I15)$$

where inv indicates, as before, terms $\sim(\delta N_{eq}^i)^2$ which will later drop out. With this, we are finally in the position to compute the transport quantities in Eqs. (52) and (57) up to linear order in δT around full equilibrium $\delta T = V_b = 0$. The stationary charge and energy current between the dot and right lead $\alpha = $ R read

$$I_{NR}^{(0)} = (N|W^R|z) = -\gamma_{cR}(N_z - N_{zR})$$
$$\approx -\frac{1-\Lambda^2}{4}\gamma_{c,eq}\delta N_{eq}^2 \frac{\mathcal{E}^{eq}\delta T}{T^2} + O(\delta T^2)$$

$$I_{HR}^{(0)} = (H|W^R|z) = \mathcal{E}^{eq}I_{NR}^{(0)} - U\gamma_{pR}(z_R^i(-\mathbb{1})^N |z)$$
$$\approx \mathcal{E}^{eq}I_{NR}^{(0)} - \kappa\delta T + O(\delta T^2), \quad (I16)$$

having recalled Eq. (I7) and identified the Fourier heat

$$\kappa = \frac{1-\Lambda^2}{4}\gamma_p \delta N_{eq}^2 (\delta N_{eq}^i)^2 \frac{U^2}{4T^2} \quad (I17)$$

as defined in, e.g., Ref. [81]. The corresponding derivatives of the currents and κ with respect to ϵ and Λ around $\Lambda = 0$ up to linear order in δT are

$$\partial_\Lambda \kappa|_\Lambda = \partial_\epsilon \partial_\Lambda \kappa|_{\Lambda=0} = 0,$$

$$\partial_\Lambda I_{NR}^{(0)}|_{\Lambda=0} \sim \partial_\Lambda I_{HR}^{(0)}|_{\Lambda=0} \sim \partial_\epsilon \partial_\Lambda I_{NR}^{(0)}|_{\Lambda=0} \approx 0 + O(\delta T^2),$$

$$\partial_\epsilon \partial_\Lambda I_{HR}^{(0)}\big|_{\Lambda=0} \approx \partial_\epsilon \mathcal{E}^{eq}\partial_\Lambda I_{NR}^{(0)}\big|_{\Lambda=0} \approx 0 + O(\delta T^2),$$

$$\frac{\partial_\epsilon I_{NR}^{(0)}}{I_{NR}^{(0)}/T}\bigg|_{\Lambda=0} \approx \frac{T}{\mathcal{E}^{eq}} - \frac{\partial_\epsilon \gamma_{c,eq}}{\gamma_{c,eq}/T} - \frac{\lambda N_{eq}^3}{\delta N_{eq}^2} + O(\delta T^2),$$

$$\frac{\partial_\epsilon \kappa}{\kappa/T}\bigg|_{\Lambda=0} = \frac{(\lambda N_{eq}^i)^3}{(\delta N_{eq}^i)^2} - \frac{\lambda N_{eq}^3}{\delta N_{eq}^2} \tag{I18}$$

as well as

$$\frac{\partial_\epsilon^2 I_{NR}^{(0)}}{I_{NR}^{(0)}/T^2}\bigg|_{\Lambda=0} \approx \left[\frac{T}{\mathcal{E}^{eq}} - \frac{\partial_\epsilon \gamma_{c,eq}}{\gamma_{c,eq}/T} - \frac{\lambda N_{eq}^3}{\delta N_{eq}^2}\right]^2$$
$$+ T\partial_\epsilon\left[\frac{T}{\mathcal{E}^{eq}} - \frac{\partial_\epsilon \gamma_{c,eq}}{\gamma_{c,eq}/T} - \frac{\lambda N_{eq}^3}{\delta N_{eq}^2}\right] + O(\delta T^2), \tag{I19}$$

$$\frac{\partial_\epsilon^2 \kappa}{\kappa/T^2}\bigg|_{\Lambda=0} = \left[\frac{(\lambda N_{eq}^i)^3}{(\delta N_{eq}^i)^2} - \frac{\lambda N_{eq}^3}{\delta N_{eq}^2}\right]^2$$
$$+ T\partial_\epsilon\left[\frac{(\lambda N_{eq}^i)^3}{(\delta N_{eq}^i)^2} - \frac{\lambda N_{eq}^3}{\delta N_{eq}^2}\right], \tag{I20}$$

$$\frac{\partial_\Lambda^2 \kappa}{\kappa}\bigg|_{\Lambda=0} = -2, \quad \frac{\partial_\Lambda^2 I_{NR}^{(0)}}{I_{NR}^{(0)}}\bigg|_{\Lambda=0} \approx -2 + O(\delta T^2) \tag{I21}$$

for the charge current $I_{NR}^{(0)}$ and Fourier heat κ and

$$\partial_\epsilon I_{HR}^{(0)}\big|_{\Lambda=0} \approx I_{NR}^{(0)}\big|_{\Lambda=0} + \mathcal{E}^{eq}\partial_\epsilon I_{NR}^{(0)}\big|_{\Lambda=0} - (\partial_\epsilon \kappa)|_{\Lambda=0}\delta T$$
$$+ O(\delta T^2), \tag{I22}$$

$$\partial_\epsilon^2 I_{HR}^{(0)}\big|_{\Lambda=0} \approx \partial_\epsilon I_{NR}^{(0)}\big|_{\Lambda=0} + \mathcal{E}^{eq}\partial_\epsilon^2 I_{NR}^{(0)}\big|_{\Lambda=0}$$
$$- (\partial_\epsilon^2 \kappa)|_{\Lambda=0}\delta T + O(\delta T^2), \tag{I23}$$

$$\partial_\Lambda^2 I_{HR}^{(0)}\big|_{\Lambda=0} \approx -2 I_{HR}^{(0)}\big|_{\Lambda=0} + O(\delta T^2) \tag{I24}$$

for the steady-state energy current $I_{HR}^{(0)}$. Note that we have neglected terms $\sim \delta N_{eq}^2(\delta N_{eq}^i)^2$ and $\sim \delta N_{eq}^2(\lambda N_{eq}^i)^3$ that are, when not scaled by the large prefactor $(U/T)^2$ as in the Fourier heat κ, strongly suppressed compared to the other terms, since the quantities of the dual inverted system have finite support at very different levels ϵ compared to the actual dot system (see Ref. [81]). Inserting the driving protocol (46) into the integral (49) and Taylor expanding the integrand $I_{NR}^{(0)}(t)$ in the small driving amplitudes $\delta\epsilon$ and $\delta\Lambda$ around the working point $\bar{\epsilon}$ and $\bar{\Lambda} = 0$ using Eqs. (I16)–(I24), we find the $\ell = 0$ heat contribution

$$\mathcal{Q}_R^{(0)} \approx \frac{2\pi}{\Omega}\left[\left(\mathcal{E}^{eq}I_{NR}^{(0)} - \kappa\delta T\right)\left(1 - \frac{(\delta\Lambda)^2}{2}\right)\right.$$
$$\left.+ \frac{(\delta\epsilon)^2}{4}\left(\mathcal{E}^{eq}\partial_\epsilon^2 I_{NR}^{(0)} + \partial_\epsilon I_{NR}^{(0)} - (\partial_\epsilon^2 \kappa)\delta T\right)\right]_{\Lambda=0}$$
$$+ O(\delta T^2). \tag{I25}$$

The $\ell = 1$ heat component depends on the energy pumping curvature (30), i.e., on the (ϵ, Λ) derivatives of N_z, p_z, and the coefficients (31) in the geometric connection. The derivatives of N_z follow from Eqs. (I4) and (I12) as well as Eq. (I14). Again dropping any terms $\sim \delta N_{eq}^2(\delta N_{eq}^i)^2$ which are not scaled

by a large prefactor $\sim (U/T)^2$, we find

$$\partial_\Lambda N_z|_{\Lambda=0} \approx \frac{1}{2}\delta N_{eq}^2 \mathcal{E}^{eq}\frac{\delta T}{T^2} + O(\delta T^2),$$

$$\partial_\epsilon N_z|_{\Lambda=0} \approx -\frac{\delta N_{eq}^2}{T} + \left[\delta N_{eq}^2 - \frac{\mathcal{E}^{eq}\lambda N_{eq}^3}{T}\right]\frac{\delta T}{2T^2} + O(\delta T^2). \tag{I26}$$

Differentiating, the parity p_z is performed analogously using Eq. (I8) together with Eqs. (I13) and (I14):

$$\partial_\Lambda p_z|_{\Lambda=0} \approx \frac{\mathcal{E}^{eq}}{T}\left(1 - N_{eq}^i\right)\delta N_{eq}^2\frac{\delta T}{T} + O(\delta T^2),$$

$$\partial_\epsilon p_z|_{\Lambda=0} \approx \frac{2}{T}\left(N_{eq}^i - 1\right)\left[\delta N_{eq}^2\left(1 - \frac{\delta T}{2T}\right) + \frac{\mathcal{E}^{eq}}{T}\lambda N_{eq}^3\frac{\delta T}{2T}\right]$$
$$+ O(\delta T^2). \tag{I27}$$

For the charge-mode coefficients in the mode-decomposed geometric connection (31) and (31a), Eqs. (I5) and (I10) yield

$$\partial_\Lambda a_{HR}^C\big|_{\Lambda=0} \approx -\frac{\mathcal{E}^{eq}}{2} + O(\delta T^2),$$

$$\partial_\epsilon a_{HR}^C\big|_{\Lambda=0} \approx \frac{1}{2} - \frac{U}{4T}\left(\delta N_{eq}^i\right)^2 + O(\delta T). \tag{I28}$$

The derivatives of the parity-mode terms (31b) and (31c) are

$$\partial_\Lambda a_{HR}^{P,N}\big|_{\Lambda=0} \approx -\frac{U}{4}\left(N_{eq}^i - 1\right) + O(\delta T^2),$$

$$\partial_\epsilon a_{HR}^{P,N}\big|_{\Lambda=0} \approx \frac{U}{4T}\left(\delta N_{eq}^i\right)^2 + O(\delta T) \tag{I29}$$

and

$$\partial_\Lambda a_{HR}^{P,p}\big|_{\Lambda=0} = -\frac{U}{8}, \quad \partial_\epsilon a_{HR}^{P,p}\big|_{\Lambda=0} = 0. \tag{I30}$$

Combining Eqs. (I26)–(I30), we obtain

$$\frac{Q_R^{(1)}}{\delta S} = B_{HR}(\{\epsilon, \Lambda\})|_{\Lambda=0}$$
$$= T\left[\left(\partial_\epsilon a_{HR}^C + \partial_\epsilon a_{HR}^{P,N}\right)\partial_\Lambda N_z\right.$$
$$\left.- \left(\partial_\Lambda a_{HR}^C + \partial_\Lambda a_{HR}^{P,N}\right)\partial_\epsilon N_z\right]\big|_{\Lambda=0}$$
$$+ T\left[\partial_\epsilon a_{HR}^{P,p}\partial_\Lambda p_z - \partial_\Lambda a_{HR}^{P,p}\partial_\epsilon p_z\right]\big|_{\Lambda=0}$$
$$\approx -\frac{\delta N_{eq}^2 \mathcal{E}^{eq}}{2}\left(1 - \frac{\delta T}{T}\right) - \frac{\lambda N_{eq}^3 \mathcal{E}^{eq}}{4}\frac{\mathcal{E}^{eq}}{T}\frac{\delta T}{T} + O(\delta T^2), \tag{I31}$$

with the surface element $\delta S = \iint_S d\Lambda(d\epsilon/T) = -\pi\sin(\phi)(\delta\epsilon/T)\delta\Lambda$ normalized by T as in the main text. The final step is to compute the work, as defined in Eq. (57), with the help of Eq. (I26). We arrive at

$$\mathcal{W}_\epsilon^{(1)} = -\partial_\Lambda N_z T\delta S|_{\Lambda=0} \approx -2T\frac{I_{NR}^{(0)}}{\gamma_{c,eq}}\delta S + O(\delta T^2), \tag{I32}$$

$$
\mathcal{W}_\epsilon^{(2)} = -\pi\Omega\delta\epsilon^2 \frac{\partial_\epsilon N_z}{\gamma_c} - \pi\Omega\cos(\phi)\delta\epsilon\,\delta\Lambda \frac{\partial_\Lambda N_z}{\gamma_c}
$$

$$
\approx \pi\frac{\Omega}{\gamma_{c,eq}}\frac{\delta\epsilon^2}{T}\delta N_{eq}^2\left(1-\frac{\delta T}{2T}\right)
$$

$$
+ \pi\frac{\Omega}{\gamma_{c,eq}}\frac{\delta\epsilon^2 \mathcal{E}^{eq}\delta T}{2T^3}\left(\lambda N_{eq}^3 - \frac{\gamma_{c,eq}}{\gamma_p}\frac{\left[\delta N_{eq}^2\right]^2}{N_{eq}^i - 1}\right)
$$

$$
+ 2\pi\frac{\Omega}{\gamma_{c,eq}}\cos(\phi)\frac{I_{NR}^{(0)}}{\gamma_{c,eq}}\delta\epsilon\,\delta\Lambda + O(\delta T^2). \tag{I33}
$$

This proves all relations necessary to derive the efficiency given in Eq. (59).

APPENDIX J: VALIDITY OF THE ADIABATIC APPROXIMATION

In Sec. V we studied energy pumping in the context of cyclically driven refrigerators, using the master equation in all orders in frequency. This Appendix studies to what extent the work and heat from this full equation deviate from the adiabatic approximation, that is, truncating at the first order the expansion of $|\rho)$ in Ω/Γ, when using it to compute thermodynamic quantities. Figure 10 shows the heat and work as functions of the driving frequency computed with and without the adiabatic approximation. More precisely, we have plotted $\mathcal{Q}_R^{adia} = \mathcal{Q}_R^{(0)} + \mathcal{Q}_R^{(1)}$ [Eq. (49)] and $\mathcal{W}_\epsilon^{adia} = \mathcal{W}_\epsilon^{(1)} + \mathcal{W}_\epsilon^{(2)}$ [Eq. (51)] and the $\mathcal{Q}_R$ and $\mathcal{W}_\epsilon$ obtained by numerically solving the master equation $\partial_t|\rho) = W|\rho)$ like in the figures of Sec. V. The adiabatic approximation gives good results for $\delta R_i\Omega \ll \Gamma$ but, as explained in Sec. V C, requires a lower driving frequency when the interaction is attractive. For the value of Ω used in the figures of Sec. V (black dotted line),
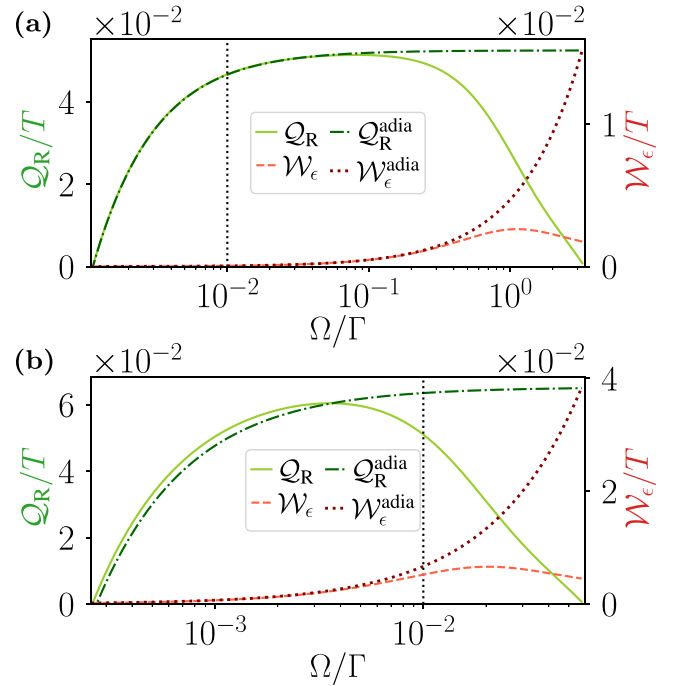

FIG. 10. Comparison of the heat $\mathcal{Q}_R$ (left axis, in green) and work (right axis, in red) computed with and without the adiabatic approximation (see the legend). The interaction is repulsive in (a) and attractive in (b). All the parameters, except for Ω, are the ones corresponding to the blue stars in Fig. 5 and the driving frequency used in the figures of Sec. V is indicated by the vertical black dotted line.

the repulsive dot is perfectly in the adiabatic-response regime while there is a significant deviation for the attractive dot. We nevertheless chose not to take a smaller Ω because the detrimental stationary contribution $\mathcal{Q}_R^{(0)}$ scales like Γ/Ω.

[1] A. L. Schawlow, Spectroscopy in a new light, Rev. Mod. Phys. **54**, 697 (1982).

[2] R. Haight, Electron dynamics at surfaces, Surf. Sci. Rep. **21**, 275 (1995).

[3] J. Splettstoesser, M. Governale, J. König, and R. Fazio, Adiabatic pumping through a quantum dot with Coulomb interactions: A perturbation expansion in the tunnel coupling, Phys. Rev. B **74**, 085305 (2006).

[4] X. Xu, B. Sun, P. R. Berman, D. G. Steel, A. S. Bracker, D. Gammon, and L. J. Sham, Coherent optical spectroscopy of a strongly driven quantum dot, Science **317**, 929 (2007).

[5] M. C. Hoffmann, J. Hebling, H. Y. Hwang, K.-L. Yeh, and K. A. Nelson, Impact ionization in InSb probed by terahertz pump—terahertz probe spectroscopy, Phys. Rev. B **79**, 161201(R) (2009).

[6] F. Reckermann, J. Splettstoesser, and M. R. Wegewijs, Interaction-Induced Adiabatic Nonlinear Transport, Phys. Rev. Lett. **104**, 226803 (2010).

[7] T. Rohwer, S. Hellmann, M. Wiesenmayer, C. Sohrt, A. Stange, B. Slomski, A. Carr, Y. Liu, L. M. Avila, M. Kalläne, S. Mathias, L. Kipp, K. Rossnagel, and M. Bauer, Collapse of

long-range charge order tracked by time-resolved photoemission at high momenta, Nature (London) **471**, 490 (2011).

[8] Y. H. Wang, H. Steinberg, P. Jarillo-Herrero, and N. Gedik, Observation of Floquet-Bloch states on the surface of a topological insulator, Science **342**, 453 (2013).

[9] J. I. Fuks, K. Luo, E. D. Sandoval, and N. T. Maitra, Time-Resolved Spectroscopy in Time-Dependent Density Functional Theory: An Exact Condition, Phys. Rev. Lett. **114**, 183002 (2015).

[10] J. Wiedenmann, E. Bocquillon, R. S. Deacon, S. Hartinger, O. Herrmann, T. M. Klapwijk, L. Maier, C. Ames, C. Brüne, C. Gould, A. Oiwa, K. Ishibashi, S. Tarucha, H. Buhmann, and L. W. Molenkamp, 4π-periodic Josephson supercurrent in HgTe-based topological Josephson junctions, Nat. Commun. **7**, 10303 (2016).

[11] R.-P. Riwar, B. Roche, X. Jehl, and J. Splettstoesser, Readout of relaxation rates by nonadiabatic pumping spectroscopy, Phys. Rev. B **93**, 235401 (2016).

[12] J. V. Koski, A. J. Landig, A. Pályi, P. Scarlino, C. Reichl, W. Wegscheider, G. Burkard, A. Wallraff, K. Ensslin, and T. Ihn, Floquet Spectroscopy of a Strongly Driven Quantum Dot

Charge Qubit with a Microwave Resonator, Phys. Rev. Lett. **121**, 043603 (2018).

[13] M. Hays, G. de Lange, K. Serniak, D. J. van Woerkom, D. Bouman, P. Krogstrup, J. Nygård, A. Geresdi, and M. H. Devoret, Direct Microwave Measurement of Andreev-Bound-State Dynamics in a Semiconductor-Nanowire Josephson Junction, Phys. Rev. Lett. **121**, 047001 (2018).

[14] T. T. Luu and H. J. Wörner, Measurement of the Berry curvature of solids using high-harmonic spectroscopy, Nat. Commun. **9**, 916 (2018).

[15] M. C. Dartiailh, J. J. Cuozzo, B. H. Elfeky, W. Mayer, J. Yuan, K. S. Wickramasinghe, E. Rossi, and J. Shabani, Missing Shapiro steps in topologically trivial Josephson junction on InAs quantum well, Nat. Commun. **12**, 78 (2021).

[16] S. Krøjer, R. Seoane Souto, and K. Flensberg, Demonstrating Majorana non-Abelian properties using fast adiabatic charge transfer, Phys. Rev. B **105**, 045425 (2022).

[17] F. Vigneau, F. Fedele, A. Chatterjee, D. Reilly, F. Kuemmeth, F. Gonzalez-Zalba, E. Laird, and N. Ares, Probing quantum devices with radio-frequency reflectometry, arXiv:2202.10516.

[18] H. le Sueur, C. Altimiras, U. Gennser, A. Cavanna, D. Mailly, and F. Pierre, Energy Relaxation in the Integer Quantum Hall Regime, Phys. Rev. Lett. **105**, 056803 (2010).

[19] C. Altimiras, H. le Sueur, U. Gennser, A. Cavanna, D. Mailly, and F. Pierre, Non-equilibrium edge-channel spectroscopy in the integer quantum Hall regime, Nat. Phys. **6**, 34 (2010).

[20] C. Altimiras, H. le Sueur, U. Gennser, A. Cavanna, D. Mailly, and F. Pierre, Tuning Energy Relaxation along Quantum Hall Channels, Phys. Rev. Lett. **105**, 226804 (2010).

[21] D. Halbertal, J. Cuppens, M. B. Shalom, L. Embon, N. Shadmi, Y. Anahory, H. R. Naren, J. Sarkar, A. Uri, Y. Ronen, Y. Myasoedov, L. S. Levitov, E. Joselevich, A. K. Geim, and E. Zeldov, Nanoscale thermal imaging of dissipation in quantum systems, Nature (London) **539**, 407 (2016).

[22] G. Rosselló, F. Battista, M. Moskalets, and J. Splettstoesser, Interference and multiparticle effects in a Mach-Zehnder interferometer with single-particle sources, Phys. Rev. B **91**, 115438 (2015).

[23] A. Marguerite, J. Birkbeck, A. Aharon-Steinberg, D. Halbertal, K. Bagani, I. Marcus, Y. Myasoedov, A. K. Geim, D. J. Perello, and E. Zeldov, Imaging work and dissipation in the quantum Hall state in graphene, Nature (London) **575**, 628 (2019).

[24] T. Krähenmann, S. G. Fischer, M. Röösli, T. Ihn, C. Reichl, W. Wegscheider, K. Ensslin, Y. Gefen, and Y. Meir, Auger-spectroscopy in quantum Hall edge channels and the missing energy problem, Nat. Commun. **10**, 3915 (2019).

[25] J. D. Fletcher, N. Johnson, E. Locane, P. See, J. P. Griffiths, I. Farrer, D. A. Ritchie, P. W. Brouwer, V. Kashcheyevs, and M. Kataoka, Continuous-variable tomography of solitary electrons, Nat. Commun. **10**, 5298 (2019).

[26] A. G. Bauer and B. Sothmann, Phase-dependent transport in thermally driven superconducting single-electron transistors, Phys. Rev. B **104**, 195418 (2021).

[27] F. Haupt, M. Leijnse, H. L. Calvo, L. Classen, J. Splettstoesser, and M. R. Wegewijs, Heat, molecular vibrations, and adiabatic driving in non-equilibrium transport through interacting quantum dots, Phys. Status Solidi B **250**, 2315 (2013).

[28] M. H. Kolodrubetz, F. Nathan, S. Gazit, T. Morimoto, and J. E. Moore, Topological Floquet-Thouless Energy Pump, Phys. Rev. Lett. **120**, 150601 (2018).

[29] M. Hasegawa and T. Kato, Geometrical optimization of pumping power under adiabatic parameter driving, J. Phys. Soc. Jpn. **89**, 064706 (2020).

[30] T. Simons, D. Meidan, and A. Romito, Pumped heat and charge statistics from Majorana braiding, Phys. Rev. B **102**, 245420 (2020).

[31] H. L. Calvo, L. Classen, J. Splettstoesser, and M. R. Wegewijs, Interaction-induced charge and spin pumping through a quantum dot at finite bias, Phys. Rev. B **86**, 245308 (2012).

[32] T. Pluecker, M. R. Wegewijs, and J. Splettstoesser, Gauge freedom in observables and Landsberg's nonadiabatic geometric phase: Pumping spectroscopy of interacting open quantum systems, Phys. Rev. B **95**, 155431 (2017).

[33] T. Pluecker, M. R. Wegewijs, and J. Splettstoesser, Meter calibration and the geometric pumping process in open quantum systems, arXiv:1711.10431.

[34] R. Alicki, The quantum open system as a model of the heat engine, J. Phys. A: Math. Gen. **12**, L103 (1979).

[35] T. Feldmann and R. Kosloff, Quantum four-stroke heat engine: Thermodynamic observables in a model with intrinsic friction, Phys. Rev. E **68**, 016101 (2003).

[36] A. E. Allahverdyan, R. S. Johal, and G. Mahler, Work extremum principle: Structure and function of quantum heat engines, Phys. Rev. E **77**, 041118 (2008).

[37] R. Kosloff and A. Levy, Quantum heat engines and refrigerators: Continuous devices, Annu. Rev. Phys. Chem. **65**, 365 (2014).

[38] R. Kosloff and Y. Rezek, The quantum harmonic Otto cycle, Entropy **19**, 136 (2017).

[39] N. M. Myers, O. Abah, and S. Deffner, Quantum thermodynamic devices: From theoretical proposals to experimental reality, AVS Quantum Sci. **4**, 027101 (2022).

[40] Y. Hino and H. Hayakawa, Geometrical formulation of adiabatic pumping as a heat engine, Phys. Rev. Res. **3**, 013187 (2021).

[41] S. Juergens, F. Haupt, M. Moskalets, and J. Splettstoesser, Thermoelectric performance of a driven double quantum dot, Phys. Rev. B **87**, 245423 (2013).

[42] A.-M. Daré and P. Lombardo, Time-dependent thermoelectric transport for nanoscale thermal machines, Phys. Rev. B **93**, 035303 (2016).

[43] R. Bustos-Marún, G. Refael, and F. von Oppen, Adiabatic Quantum Motors, Phys. Rev. Lett. **111**, 060802 (2013).

[44] H. L. Calvo, F. D. Ribetto, and R. A. Bustos-Marún, Real-time diagrammatic approach to current-induced forces: Application to quantum-dot based nanomotors, Phys. Rev. B **96**, 165309 (2017).

[45] A. Bruch, S. V. Kusminskiy, G. Refael, and F. von Oppen, Interacting adiabatic quantum motor, Phys. Rev. B **97**, 195411 (2018).

[46] M. F. Ludovico, J. S. Lim, M. Moskalets, L. Arrachea, and D. Sánchez, Dynamical energy transfer in ac-driven quantum systems, Phys. Rev. B **89**, 161306(R) (2014).

[47] R. A. Bustos-Marún and H. L. Calvo, Thermodynamics and steady state of quantum motors and pumps far from equilibrium, Entropy **21**, 824 (2019).

[48] B. Bhandari, P. T. Alonso, F. Taddei, F. von Oppen, R. Fazio, and L. Arrachea, Geometric properties of adiabatic quantum thermal machines, Phys. Rev. B **102**, 155407 (2020).

[49] F. D. Ribetto, R. A. Bustos-Marún, and H. L. Calvo, Role of coherence in quantum-dot-based nanomachines within the Coulomb blockade regime, Phys. Rev. B **103**, 155435 (2021).

[50] B. Bhandari, R. Fazio, F. Taddei, and L. Arrachea, From nonequilibrium Green's functions to quantum master equations for the density matrix and out-of-time-order correlators: Steady-state and adiabatic dynamics, Phys. Rev. B **104**, 035425 (2021).

[51] I. L. Aleiner and A. V. Andreev, Adiabatic Charge Pumping in Almost Open Dots, Phys. Rev. Lett. **81**, 1286 (1998).

[52] T. Aono, Adiabatic Pumping in the Mixed-Valence and Kondo Regimes, Phys. Rev. Lett. **93**, 116601 (2004).

[53] J. Splettstoesser, M. Governale, J. König, and R. Fazio, Adiabatic Pumping through Interacting Quantum Dots, Phys. Rev. Lett. **95**, 246803 (2005).

[54] A. Schiller and A. Silva, Adiabatic pumping through a quantum dot in the Kondo regime: Exact results at the Toulouse limit, Phys. Rev. B **77**, 045330 (2008).

[55] M. Moskalets and M. Büttiker, Dynamic scattering channels of a double barrier structure, Phys. Rev. B **78**, 035301 (2008).

[56] R.-P. Riwar and J. Splettstoesser, Charge and spin pumping through a double quantum dot, Phys. Rev. B **82**, 205308 (2010).

[57] F. Battista and P. Samuelsson, Proposal for nonlocal electron-hole turnstile in the quantum Hall regime, Phys. Rev. B **83**, 125324 (2011).

[58] M. Taguchi, S. Nakajima, T. Kubo, and Y. Tokura, Quantum adiabatic pumping by modulating tunnel phase in quantum dots, J. Phys. Soc. Jpn. **85**, 084704 (2016).

[59] M. Hasegawa and T. Kato, Temperature-driven and electrochemical-potential-driven adiabatic pumping via a quantum dot, J. Phys. Soc. Jpn. **86**, 024710 (2017).

[60] M. Hasegawa and T. Kato, Effect of interaction on reservoir-parameter-driven adiabatic charge pumping via a single-level quantum dot system, J. Phys. Soc. Jpn. **87**, 044709 (2018).

[61] H. Pothier, P. Lafarge, C. Urbina, D. Esteve, and M. H. Devoret, Single-electron pump based on charging effects, Europhys. Lett. **17**, 249 (1992).

[62] P. J. Leek, M. R. Buitelaar, V. I. Talyanskii, C. G. Smith, D. Anderson, G. A. C. Jones, J. Wei, and D. H. Cobden, Charge Pumping in Carbon Nanotubes, Phys. Rev. Lett. **95**, 256802 (2005).

[63] B. Roche, R.-P. Riwar, B. Voisin, E. Dupont-Ferrier, R. Wacquez, M. Vinet, M. Sanquer, J. Splettstoesser, and X. Jehl, A two-atom electron pump, Nat. Commun. **4**, 1581 (2013).

[64] J. P. Pekola, O.-P. Saira, V. F. Maisi, A. Kemppinen, M. Möttönen, Y. A. Pashkin, and D. V. Averin, Single-electron current sources: Toward a refined definition of the ampere, Rev. Mod. Phys. **85**, 1421 (2013).

[65] L. Arrachea, M. Moskalets, and L. Martin-Moreno, Heat production and energy balance in nanoscale engines driven by time-dependent fields, Phys. Rev. B **75**, 245420 (2007).

[66] J. Ren, P. Hänggi, and B. Li, Berry-Phase-Induced Heat Pumping and Its Impact on the Fluctuation Theorem, Phys. Rev. Lett. **104**, 170601 (2010).

[67] M. F. Ludovico, F. Battista, F. von Oppen, and L. Arrachea, Adiabatic response and quantum thermoelectrics for ac-driven quantum systems, Phys. Rev. B **93**, 075136 (2016).

[68] R.-P. Riwar and J. Splettstoesser, Transport fluctuation relations in interacting quantum pumps, New J. Phys. **23**, 013010 (2021).

[69] A. A. M. Staring, L. W. Molenkamp, B. W. Alphenaar, H. van Houten, O. J. A. Buyk, M. A. A. Mabesoone, C. W. J. Beenakker, and C. T. Foxon, Coulomb-blockade oscillations in the thermopower of a quantum dot, Europhys. Lett. **22**, 57 (1993).

[70] A. S. Dzurak, C. G. Smith, M. Pepper, D. A. Ritchie, J. E. F. Frost, G. A. C. Jones, and D. G. Hasko, Observation of Coulomb blockade oscillations in the thermopower of a quantum dot, Solid State Commun. **87**, 1145 (1993).

[71] B. A. Placke, T. Pluecker, J. Splettstoesser, and M. R. Wegewijs, Attractive and driven interactions in quantum dots: Mechanisms for geometric pumping, Phys. Rev. B **98**, 085307 (2018).

[72] G. Cheng, M. Tomczyk, S. Lu, J. P. Veazey, M. Huang, P. Irvin, S. Ryu, H. Lee, C.-B. Eom, C. S. Hellberg, and J. Levy, Electron pairing without superconductivity, Nature (London) **521**, 196 (2015).

[73] A. Hamo, A. Benyamini, I. Shapir, I. Khivrich, J. Waissman, K. Kaasbjerg, Y. Oreg, F. von Oppen, and S. Ilani, Electron attraction mediated by Coulomb repulsion, Nature (London) **535**, 395 (2016).

[74] G. Cheng, M. Tomczyk, A. B. Tacla, H. Lee, S. Lu, J. P. Veazey, M. Huang, P. Irvin, S. Ryu, C.-B. Eom, A. Daley, D. Pekker, and J. Levy, Tunable Electron-Electron Interactions in LaAlO$_3$/SrTiO$_3$ Nanostructures, Phys. Rev. X **6**, 041042 (2016).

[75] G. E. D. K. Prawiroatmodjo, M. Leijnse, F. Trier, Y. Chen, D. V. Christensen, M. von Soosten, N. Pryds, and T. S. Jespersen, Transport and excitations in a negative-U quantum dot at the LaAlO$_3$/SrTiO$_3$ interface, Nat. Commun. **8**, 395 (2017).

[76] J. Schulenborg, R. B. Saptsov, F. Haupt, J. Splettstoesser, and M. R. Wegewijs, Fermion-parity duality and energy relaxation in interacting open systems, Phys. Rev. B **93**, 081411(R) (2016).

[77] J. Vanherck, J. Schulenborg, R. B. Saptsov, J. Splettstoesser, and M. R. Wegewijs, Relaxation of quantum dots in a magnetic field at finite bias – Charge, spin, and heat currents, Phys. Status Solidi B **254**, 1600614 (2017).

[78] J. Schulenborg, M. R. Wegewijs, and J. Splettstoesser, Thermovoltage in quantum dots with attractive interaction, Appl. Phys. Lett. **116**, 243103 (2020).

[79] J. Schulenborg, J. Splettstoesser, and M. R. Wegewijs, Duality for open fermion systems: Energy-dependent weak coupling and quantum master equations, Phys. Rev. B **98**, 235405 (2018).

[80] L. C. Ortmanns, M. R. Wegewijs, and J. Splettstoesser, Time-dependent solutions of master equations by fermionic-duality invariance: Application to a superconducting proximized quantum dot (unpublished)

[81] J. Schulenborg, A. Di Marco, J. Vanherck, M. R. Wegewijs, and J. Splettstoesser, Thermoelectrics of interacting nanosystems—exploiting superselection instead of time-reversal symmetry, Entropy **19**, 668 (2017).

[82] V. Bruch, K. Nestmann, J. Schulenborg, and M. Wegewijs, Fermionic duality: General symmetry of open systems with strong dissipation and memory, SciPost Phys. **11**, 053 (2021).

[83] J. Splettstoesser, M. Governale, J. König, and M. Büttiker, Charge and spin dynamics in interacting quantum dots, Phys. Rev. B **81**, 165318 (2010).

[84] J. Koch, M. E. Raikh, and F. von Oppen, Pair Tunneling through Single Molecules, Phys. Rev. Lett. **96**, 056803 (2006).

[85] J. Koch, E. Sela, Y. Oreg, and F. von Oppen, Nonequilibrium charge-Kondo transport through negative-*U* molecules, Phys. Rev. B **75**, 195402 (2007).

[86] T. A. Costi and V. Zlatić, Thermoelectric transport through strongly correlated quantum dots, Phys. Rev. B **81**, 235127 (2010).

[87] S. Andergassen, T. A. Costi, and V. Zlatić, Mechanism for large thermoelectric power in molecular quantum dots described by the negative-*U* Anderson model, Phys. Rev. B **84**, 241107(R) (2011).

[88] A. Taraphder and P. Coleman, Heavy-Fermion Behavior in a Negative-*U* Anderson Model, Phys. Rev. Lett. **66**, 2814 (1991).

[89] B. L. Altshuler and L. I. Glazman, Pumping electrons, Science **283**, 1864 (1999).

[90] M. Möttönen, J. J. Vartiainen, and J. P. Pekola, Experimental Determination of the Berry Phase in a Superconducting Charge Pump, Phys. Rev. Lett. **100**, 177201 (2008).

[91] T. Yuge, T. Sagawa, A. Sugita, and H. Hayakawa, Geometrical pumping in quantum transport: Quantum master equation approach, Phys. Rev. B **86**, 235308 (2012).

[92] J. Thingna, P. Hänggi, R. Fazio, and M. Campisi, Geometric quantum pumping in the presence of dissipation, Phys. Rev. B **90**, 094517 (2014).

[93] H. Thierschmann, R. Sánchez, B. Sothmann, F. Arnold, C. Heyn, W. Hansen, H. Buhmann, and L. W. Molenkamp, Three-terminal energy harvester with coupled quantum dots, Nat. Nanotechnol. **10**, 854 (2015).

[94] M. Josefsson, A. Svilans, A. M. Burke, E. A. Hoffmann, S. Fahlvik, C. Thelander, M. Leijnse, and H. Linke, A quantum-dot heat engine operating close to the thermodynamic efficiency limits, Nat. Nanotechnol. **13**, 920 (2018).

[95] J. M. Luttinger, Theory of thermal transport coefficients, Phys. Rev. **135**, A1505 (1964).

[96] F. G. Eich, A. Principi, M. Di Ventra, and G. Vignale, Luttinger-field approach to thermoelectric transport in nanoscale conductors, Phys. Rev. B **90**, 115116 (2014).

[97] G. Tatara, Thermal Vector Potential Theory of Transport Induced by a Temperature Gradient, Phys. Rev. Lett. **114**, 196601 (2015).

[98] F. Cavaliere, M. Governale, and J. König, Nonadiabatic Pumping through Interacting Quantum Dots, Phys. Rev. Lett. **103**, 136801 (2009).

[99] R. B. Saptsov and M. R. Wegewijs, Time-dependent quantum transport: Causal superfermions, exact fermion-parity protected decay modes, and Pauli exclusion principle for mixed quantum states, Phys. Rev. B **90**, 045407 (2014).

[100] J. Schulenborg, Dynamics of open fermionic nano-systems – a fundamental symmetry and its application to electron transport in interacting quantum dots, Ph.D. thesis, Chalmers University of Technology, 2018.

[101] L.-A. Wu and D. Segal, Energy flux operator, current conservation and the formal Fourier's law, J. Phys. A: Math. Theor. **42**, 025302 (2009).

[102] P. Haughian, M. Esposito, and T. L. Schmidt, Quantum thermodynamics of the resonant-level model with driven system-bath coupling, Phys. Rev. B **97**, 085435 (2018).

[103] C. Z. Ning and H. Haken, Geometrical Phase and Amplitude Accumulations in Dissipative Systems with Cyclic Attractors, Phys. Rev. Lett. **68**, 2109 (1992).

[104] A. S. Landsberg, Spatial symmetries and geometrical phases in classical dissipative systems, Mod. Phys. Lett. B **07**, 71 (1993).

[105] N. A. Sinitsyn, The stochastic pump effect and geometric phases in dissipative and stochastic systems, J. Phys. A: Math. Theor. **42**, 193001 (2009).

[106] V. I. Arnold, *Mathematical Methods of Classical Mechanics* (Springer, New York, 1978), Chap. 7.

[107] J. Splettstoesser, M. Governale, and J. König, Adiabatic charge and spin pumping through quantum dots with ferromagnetic leads, Phys. Rev. B **77**, 195320 (2008).

[108] H. J. D. Miller, M. H. Mohammady, M. Perarnau-Llobet, and G. Guarnieri, Thermodynamic Uncertainty Relation in Slowly Driven Quantum Heat Engines, Phys. Rev. Lett. **126**, 210603 (2021).

[109] M. Esposito, M. A. Ochoa, and M. Galperin, Quantum Thermodynamics: A Nonequilibrium Green's Function Approach, Phys. Rev. Lett. **114**, 080602 (2015).

[110] J. Eglinton and K. Brandner, Geometric bounds on the power of adiabatic thermal machines, Phys. Rev. E **105**, L052102 (2022).

[111] A. S. Dzurak, C. G. Smith, C. H. W. Barnes, M. Pepper, L. Martín-Moreno, C. T. Liang, D. A. Ritchie, and G. A. C. Jones, Thermoelectric signature of the excitation spectrum of a quantum dot, Phys. Rev. B **55**, R10197 (1997).

[112] T. Prosen, $\mathbb{PT}$-Symmetric Quantum Liouvillean Dynamics, Phys. Rev. Lett. **109**, 090404 (2012).